DISSERTATION

FAST OFF-LATTICE MONTE CARLO SIMULATIONS OF PHASE TRANSITIONS IN BLOCK COPOLYMERS AND LIQUID CRYSTALS

Submitted by

Jing Zong

Department of Chemical and Biological Engineering

In partial fulfillment of the requirements

For the Degree of Doctor of Philosophy

Colorado State University

Fort Collins, Colorado

Summer 2015

Doctoral Committee:

Advisor: David (Qiang) Wang

Travis S. Bailey
Grzegorz Szamel
A. Ted Watson

ABSTRACT

FAST OFF-LATTICE MONTE CARLO SIMULATIONS OF PHASE TRANSITIONS IN BLOCK COPOLYMERS AND LIQUID CRYSTALS

The basic idea of the so-called fast off-lattice Monte Carlo (FOMC) simulations is to perform particle-based Monte Carlo (MC) simulations in continuum with the excluded-volume interactions modeled by soft repulsive potentials that allow particle complete overlapping, where using soft potentials naturally arises from the application of coarse-grained models. This method is particularly suitable for the study of equilibrium properties of soft matter. One apparent advantage of FOMC is that using soft potentials can greatly improve the sampling efficiency in the simulations. Another advantage is that FOMC simulations can be performed in any statistical ensemble, and all the advanced off-lattice MC techniques proposed to date can be readily applied to further improve the sampling efficiency. Moreover, it provides a powerful methodology to directly compare theoretical results with simulation results without any parameter fitting. Last but not least, using FOMC is the only way to study experimentally accessible fluctuation/correlation effects in many-chain systems.

This work makes use of FOMC simulations to study phase transitions in block copolymers and liquid crystals. To compare with the simulations results, various theoretical methods are also applied in the research. Chapter 2 is devoted to study the classic yet unsolved problem of fluctuation/correlation effects on the order-disorder transition (ODT) of symmetric diblock copolymer (DBC). In Chapter 3, we highlight the importance of quantitative and parameter-fitting-free comparisons among different models/methods. In Chapter 4, we investigate the effect of system compressibility on the ODT of DBC melts. In Chapter 5, we extend FOMC simulations to study the isotropic-nematic transition of liquid crystals. Finally, in Chapter 6, we briefly summarize all the studies in this dissertation and give some directions to future work.

ACKNOWLEDGEMENTS

First of all, I would like to express my greatest gratitude to my family, my parents Yuan-He Zong and Xiao-Ru He and my wife Hong-Guo Li, not only for their love, but also for their understanding on my choice. Without their support, I cannot finish my Ph.D. program.

I would like to extend my deep appreciation to my advisor, Professor David (Qiang) Wang, for introducing me to the research area on molecular simulation and theoretical calculation. I have learned a lot from his ways of solving problems and the rigorous attitude towards science.

I would also like to thank Professor Travis Bailey, Professor Grzegorz Szamel, and Professor Ted Watson for their serving on my committee.

I owe a lot of thanks to many members in Wang's group for their kind help, especially to Dr. Yu-Hua Yin, Dr. Dong Meng, Dr. Xing-Hua Zhang, Dr. De-Lian Yang, Dr. Peng-Fei Zhang, Dr. Vijay Gupta, and Mr. Paramvir Sandhu.

Finally, I would like to thank all the faculty and staff members of Department of Chemical and Biological Engineering at Colorado State University.

This work is funded by Department of Energy under Award No. DE-FG02-07ER46448, which is gratefully acknowledged.

TABLE OF CONTENTS

LIST OF TABLES

LIST OF FIGURES

CHAPTER 1

INTRODUCTION

1.1 Fast Off-lattice Monte Carlo Simulation

Fast off-lattice Monte Carlo (FOMC) simulations have recently attracted great research interest in the study of soft matter.[1–3] The basic idea of the so-called FOMC simulations is to perform particle-based Monte Carlo (MC) simulations in continuum with the excluded-volume interactions modeled by soft repulsive potentials that allow particle complete overlapping. Using soft potentials naturally arises from the application of coarse-grained (CG) models. Because full atomistic simulations of soft matter are not affordable due to their formidable computational requirements, CG models are inevitably applied in most molecular simulations. In a CG model, one CG unit usually represents the center-of-mass of tens to hundreds of atoms of the original system, and complete overlapping between these CG units is thus possible. In this sense, the interaction between CG units should be described as a soft effective pair potential[4,5] instead of hard repulsion (e.g. harsh Lennard-Jones repulsion) originally derived from the interaction between two atoms.

FOMC simulation is particularly suitable for the study of equilibrium properties of soft matter. One apparent advantage of FOMC is that using soft potentials can greatly improve the sampling efficiency in simulations. Wang and Yin[1] showed in their recent work that the statistical inefficiency, which measures the average number of MC steps needed to generate one statistically uncorrelated sample in MC simulations, dramatically increases with the increasing interaction strength of the pair potential. This indicates that FOMC simulations can give much better sampling of the configuration space than conventional molecular simulations with hard repulsions, of which the interaction strength is actually infinitely large.

Another advantage is that FOMC simulations can be performed in any statistical ensemble, and all the advanced off-lattice MC techniques proposed to date can be readily applied to further improve the sampling efficiency. For example, in this work, we perform FOMC simulations in canonical (nVT) and isothermal-isobaric (nPT) ensembles, and we also show that FOMC simulations can be perfectly combined with replica exchange and multiple histogram reweighting technique to determine phase transition point. Moreover, soft model (Hamiltonian) used in FOMC simulations can also be applied in theoretical calculations; this offers a powerful method to directly compare theoretical results with simulation results without any parameter fitting, and with this methodology we can unambiguously quantify the approximations used in the theory. Last but not least, using FOMC is the only way to study experimentally accessible fluctuation/correlation effects in many-chain systems, which are controlled by the invariant degree of polymerization $\bar{\mathcal{N}}$. In conventional molecular simulations of concentrated polymer solutions or melts with hard repulsions, $\bar{\mathcal{N}}$ is on the same order of magnitude as the number of monomers in a chain N, i.e., $\bar{\mathcal{N}} \sim N \lesssim 10^2$, which is much smaller than the typical experimental range of $\bar{\mathcal{N}} = 500 \sim 20,000$. In contrast, with soft potentials, $\bar{\mathcal{N}}$ and N are decoupled, and one can therefore study systems of much larger $\bar{\mathcal{N}}$-values, while N becomes a chain discretization parameter that does not correspond to the actual chain length used in experiments. This is crucial to study fluctuation/correlation effects of polymeric systems in experimentally accessible range.

This work makes use of FOMC simulations to study phase transitions in block copolymers and liquid crystals. To compare with the simulations results, various theoretical methods are also applied in the research.

Chapter 2 is devoted to study the classic yet unsolved problem of fluctuation/correlation effects on the order-disorder transition (ODT) of symmetric diblock copolymer (DBC). Exactly the same model system (Hamiltonian) is used in both FOMC simulations and mean-field theory; the ODT shift is therefore due to the fluctuations/correlations neglected by the latter. We have varied all the parameters in our model system (the invariant degree

of polymerization $\bar{\mathcal{N}}$, the number of segments N on each chain, the finite interaction range σ, and the compressibility N/κ of DBC melts) to examine their effects on the ODT shift. While $\chi^*/\chi^*_{\rm MF} - 1 \propto \bar{\mathcal{N}}^{-k}$ is found in all the cases, k decreases around $\bar{\mathcal{N}}_{\rm cp}$ (the $\bar{\mathcal{N}}$-value corresponding to the FCC close packing of polymer segments as hard spheres), indicating the short-range correlation effects.

In Chapter 3, we highlight the importance of quantitative and parameter-fitting-free comparisons among different models/methods. We compare the self-consistent field (SCF) calculation results of the "standard" DBC model[6] with those of the DPD model (i.e., DBC model used in dissipative particle dynamics (DPD) simulations[7]) to reveal the effects of the model difference. For the DPD model, we compare SCF calculation results with FOMC simulation results to unambiguously quantify their theoretical approximation. Furthermore, we compare FOMC simulation results with DPD simulation results[7] to identify the kinetically trapped structures in the latter.

In Chapter 4, we investigate the effect of system compressibility N/κ on the ODT of DBC melts. We use both the SCF calculations and FOMC simulations to determine the ODT of compressible DBC melts by equating the Gibbs free energy per chain of the two co-existing phases, and compare with our previous results obtained by equating the Helmholtz free energy per chain in Chapters 2 and 3. We find that the co-existing range is quite small and decreases as the system becomes less compressible, which justifies the previous results in Chapters 2 and 3 where it was assumed that the co-existing phases have the same density. We also find that, when $N/\kappa = 0$, the SCF theory predicts the ODT to be a second-order phase transition even for asymmetric DBC melts.

In Chapter 5, we extend FOMC simulations to study the isotropic-nematic transition (INT) of liquid crystals (modeled as spherocylinders). We propose a novel anisotropic soft potential that takes into account the degree of overlap between two spherocylinders, thus superior to other soft-core spherocylinder models depending only on the minimum distance between two line segments representing spherocylinders. We determine the INT with FOMC

simulations and virial expansion (VE), and find that VE predictions are in qualitative agreement with FOMC simulation results, and become more accurate with increasing aspect ratio of spherocylinders.

Finally, in Chapter 6, we briefly summarize all the studies in this dissertation, and then give some extensions that can be possibly made based on the current work.

1.2 List of Publications

In this section, all of the publications (including the unpublished work) in my Ph.D. study are listed as follows:

1. J. Zong, V. Gupta, and Q. Wang , "A Novel Soft-Core Model for Rod-Coil Block Copolymers", in preparation.
   (Here I did the fast off-lattice Monte Carlo simulations and self-consistent field calculations.)

2. J. Zong and Q. Wang, "On the Order-Disorder Transition of Compressible Diblock Copolymer Melts", to be submitted.

3. D. Yang, J. Zong, and Q. Wang, "Fluctuation/Correlation Effects in Symmetric Diblock Copolymers: Direct Comparisons between Fast Off-Lattice Monte Carlo Simulations and Integral Equation Theories", to be submitted.
   (Here I did the fast off-lattice Monte Carlo simulations.)

4. J. Zong and Q. Wang, "Fluctuation/Correlation Effects in Symmetric Diblock Copolymers: On the Order-Disorder Transition", J. Chem. Phys. **139**, 124907 (2013).

5. P. Sandhu, J. Zong, D. Yang, and Q. Wang, "On the Comparisons Between Dissipative Particle Dynamics Simulations and Self-Consistent Field Calculations of Diblock Copolymer Microphase Separation", J. Chem. Phys. **138**, 194904 (2013).
   (Here I did the fast off-lattice Monte Carlo simulations.)

6. J. Zong, X. Zhang, and Q. Wang, "Fast Off-Lattice Monte Carlo Simulations of Soft-Core Spherocylinders: Isotropic-Nematic Transition and Comparisons with Virial Expansion", J. Chem. Phys. **137**, 134904 (2012).
   (Here I did the fast off-lattice Monte Carlo simulations.)

REFERENCES

[1] Q. Wang and Y. Yin, J. Chem. Phys. **130**, 104903 (2009).

[2] F. A. Detcheverry, D. Q. Pike, P. F. Nealey, M. Muller, and J. J. de Pablo, Phys. Rev. Lett. **102**, 197801 (2009).

[3] D. Q. Pike, F. A. Detcheverry, M. Muller, and J. J. de Pablo, J. Chem. Phys. **131**, 084903 (2009).

[4] A. J. Clark, J. McCarty, I. Y. Lyubimov, and M. G. Guenza, Phys. Rev. Lett. **102**, 197801 (2009).

[5] D.Yang and Q. Wang, J. Chem. Phys. **142**, 054905 (2015).

[6] M. W. Matsen and F. S. Bates, Macromolecules **29**, 1091 (1996).

[7] R. D. Groot and T. J. Madden, J. Chem. Phys. **108**, 8713 (1998).

CHAPTER 2

FLUCTUATION/CORRELATION EFFECTS ON THE ORDER-DISORDER TRANSITION OF SYMMETRIC DIBLOCK COPOLYMERS

2.1 Introduction

The self-assembly of block copolymers has attracted great interest not only due to their applications (e.g., in nanotechnology) but also the underlying physics.[1] Owing to the well developed polymer self-consistent field (SCF) calculations,[2] good or even quantitative understanding has been achieved for the self-assembly of flexible linear diblock copolymer (DBC) melts in bulk.[3] Due to its mean-field approximation, however, SCF theory gives qualitatively incorrect predictions in the region near the order-disorder transition (ODT) where the system fluctuations it neglects become important. In particular, it fails to capture the fluctuation-induced first-order phase transition for ODT of symmetric DBC[4] and the direct transition between the gyroid and disordered phases.[5]

With the polymer SCF theory well developed in terms of both theoretical formalisms and numerical methods,[2] it is natural and timely to develop advanced theories that can quantitatively account for the fluctuation/correlation effects neglected by this mean-field theory. For this purpose, we perform this study unambiguously quantifying the effects of fluctuations and correlations, using the simplest block copolymer system – symmetric DBC melts – as an example. Here, we focus on the classic yet unsolved problem of ODT shift of symmetric DBC from the mean-field prediction, and directly compare (i.e., without any parameter-fitting) our Monte Carlo (MC) simulations and mean-field predictions based on exactly the same model system (Hamiltonian), such that the differences between them

are due to the fluctuations/correlations neglected by the latter. Our results here are the prerequisite for developing and testing new fluctuation theories for inhomogeneous polymeric systems, which are clearly needed as the existing theories on this classic problem are not satisfactory.

About 28 years ago, Fredrickson and Helfand (FH) presented so far the most influential fluctuation theory for DBC,[6] which can qualitatively explain the fluctuation-induced first-order phase transition for ODT of symmetric DBC, as well as the direct transition between the gyroid and disordered phases.[7] This theory is based on the Hartree analysis of Brazovskii[8] and the Ohta-Kawasaki effective Hamiltonian[9] for the "standard" model of incompressible DBC melts of continuous Gaussian chains with Dirac δ-function interactions. In particular, the ODT shift of symmetric DBC from the mean-field value is predicted to be $\chi^*/\chi^*_{\rm MF} - 1 = 3.91\bar{\mathcal{N}}^{-1/3}$, where the Flory-Huggins χ parameter characterizes the repulsion between A and B segments, and the invariant degree of polymerization $\bar{\mathcal{N}} \equiv (nR^3_{e,0}/V)^2$ is for n monodisperse copolymer chains in volume V with $R_{e,0}$ denoting the root-mean-square end-to-end distance of an ideal chain.[6] $\bar{\mathcal{N}}$ essentially measures the number of chains with which a single chain interacts within its volume and therefore controls the fluctuations in polymeric systems. For systems at the highest packing density (i.e., polymer melts) in both experiments and conventional molecular simulations with hard excluded-volume interactions (e.g., the Lennard-Jones potential or the self- and mutual-avoiding walk on a lattice), one can estimate $V \sim nNb^3$ and $R_{e,0} \sim \sqrt{N}b$ with b denoting the size of a monomer or segment, which means $\bar{\mathcal{N}}$ is on the same order of magnitude as the chain length N.

To be more quantitative, for monodisperse DBC melts where each copolymer chain consists of $N_{\rm A}$ monomers of type A followed by $N_{\rm B}$ monomers of type B, with $R^2_{e,0} = N_{\rm A}a^2_{\rm A} + N_{\rm B}a^2_{\rm B}$ and $nN = \bar{\rho}_0 V$, we have $\bar{\mathcal{N}} = N\bar{\rho}^2_0\bar{a}^6$; here $N = N_{\rm A} + N_{\rm B}$, $\bar{\rho}_0 \equiv \phi_{\rm A}\rho_{0,{\rm A}} + (1-\phi_{\rm A})\rho_{0,{\rm B}}$, $\bar{a} \equiv \sqrt{fa^2_{\rm A} + (1-f)a^2_{\rm B}}$, $f \equiv N_{\rm A}/N$, $a_{\rm A}$ ($a_{\rm B}$) denotes the statistical segment length of the A (B) block, $\rho_{0,{\rm A}}$ ($\rho_{0,{\rm B}}$) the A (B) monomer number density, and $\phi_{\rm A}$ the overall volume fraction of the A block. Fig. 2.1 shows $\bar{\mathcal{N}}$ vs. the bulk lamellar period L_0 for nearly symmetric DBC

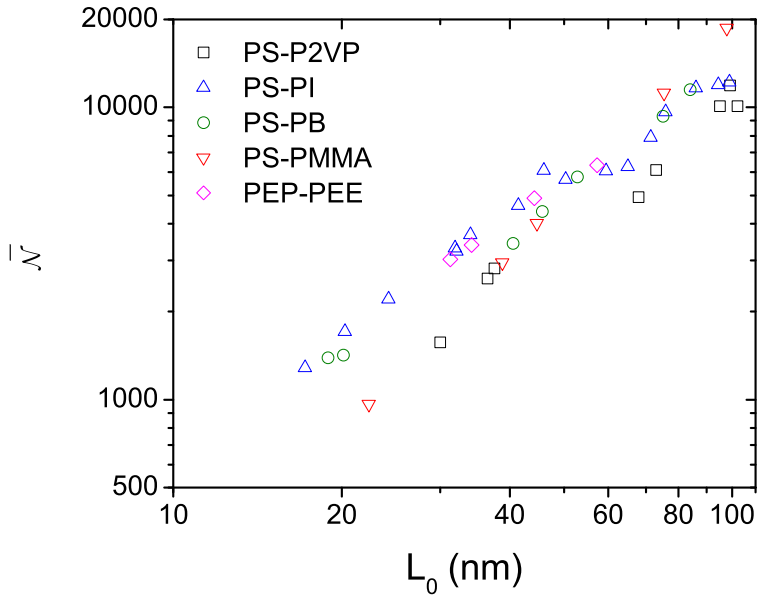

Figure 2.1: Logarithmic plot of the invariant degree of polymerization $\bar{\mathcal{N}}$ as a function of the bulk lamellar period L_0 for nearly symmetric DBC melts commonly used in experiments. See main text and Table 2.1 for details.

melts commonly used in experiments,[10–15] and Table 2.1 lists the values of a and ρ_0 for each block. The range of $L_0 = 10 \sim 100$nm, which is of interest in most applications of DBC, roughly corresponds to $\bar{\mathcal{N}} = 500 \sim 20,000$ (note that $\bar{\mathcal{N}}$ is quite sensitive to a, and that L_0 depends on the temperature used in experiments[10–15]).

However, the Brazovskii approximation used in FH[6] and related[7,23] Hartree theories, which takes into account only critical fluctuations in a specific way, was questioned about a decade ago.[24] The lack of unambiguous determination of χ for an experimental system unfortunately precludes quantitative test of these theoretical predictions by experiments. Similarly, the standard model used in these theories cannot be directly employed in molecular simulations due to its continuous Gaussian chains (i.e., $N \to \infty$) and Dirac δ-function interactions. We are therefore not concerned with testing such theories in this work and do not expect their predictions to be found in our simulations.

On the other hand, most conventional molecular simulations of concentrated polymer solutions or melts have $\bar{\mathcal{N}} \lesssim 10^2$ (e.g., the leftmost data point in Fig. 2.2 is at $\bar{\mathcal{N}} \approx 139$), too

Table 2.1: Statistical segment length a and monomer number density ρ_0 for various blocks. Values in the same row as the block name are used in Fig. 2.1. For PS-PB, we calculate $L_0 = 2\pi/q^*$, where the small-angle scattering peak position q^* is taken as the average of the shear aligned results from Table II of Ref. [13]. For PEP-PEE, we obtain its N and q^* from Fig. 4 of Ref. [15].

Block	a (nm)	ρ_0 (mol/cm^3)
polystyrene (PS)	0.67 [16]	0.0101 [17]
		0.0093 [18]
poly(2-vinylpyridine) (P2VP)	0.71 [19]	0.0109 [10]
polyisoprene (PI)	0.69 [20]	0.0136 [11]
	0.59 [21]	0.0133 [12]
polybutadiene (PB)	0.63 [17]	0.0165 [18]
	0.69 [18]	
poly-(methylmethacrylate) (PMMA)	0.65 [18]	0.0119 [17]
	0.64 ± 0.06 [17]	0.0113 [18]
poly(ethylene-propylene) (PEP)	0.72 [22]	0.0121 [22]
poly(ethylethylene) (PEE)	0.50 [22]	0.0155 [22]

small to be accessible in DBC experiments. Using soft potentials, which allow particle overlapping and naturally arise from coarse-graining real monomers into segments,[25] is therefore the best way to study DBC melts with $\bar{\mathcal{N}} = 500 \sim 20,000$ (i.e., with experimentally accessible fluctuations), where $nN = \bar{\rho}_0 V$ no longer holds (thus $\bar{\mathcal{N}}$ and N are decoupled) and N in such models becomes a chain discretization parameter that does not correspond to the actual chain length used in experiments. This point is crucial for understanding coarse-grained models with soft potentials, the use of which is the basic idea of the recently proposed fast Monte Carlo simulations.[26,27]

To demonstrate the need of our study quantifying the ODT shift of symmetric DBC, Fig. 2.2 summarizes recent simulation results addressing this classic problem; among the many simulation studies[28–33] reported in the literature, these represent the most accurate data obtained using each method and are briefly explained in the following: Beardsley and Matsen performed conventional MC simulations on a face-centered cubic (FCC) lattice in a canonical ensemble with replica-exchange to study symmetric DBC of $N = 30$ segments modeled by the self- and mutual-avoiding walk with the nearest-neighbor repulsion between

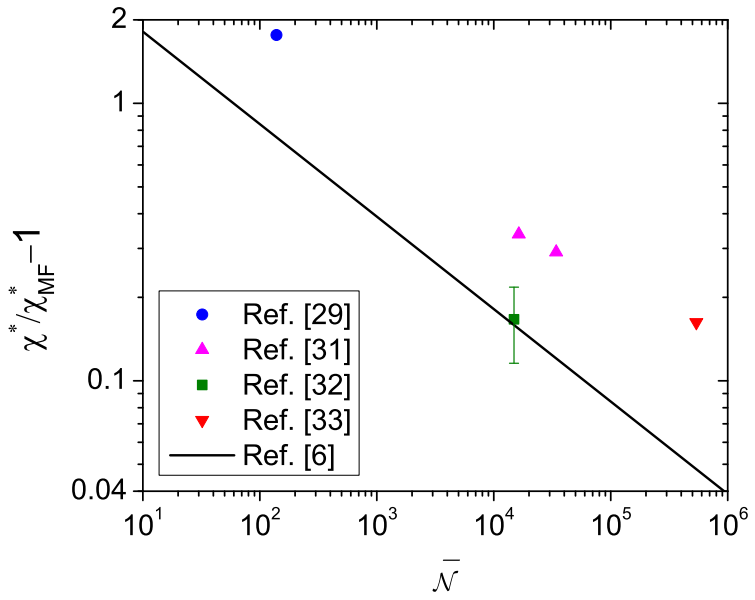

Figure 2.2: Logarithmic plot of some simulation results (points) and FH prediction (line) of the ODT shift of symmetric DBC reported in the literature as a function of $\bar{\mathcal{N}}$. See main text for details.

A and B segments ϵ_{AB} (in units of k_BT, where k_B is the Boltzmann constant and T the thermodynamic temperature); about 20% lattice sites were unoccupied, treated as an athermal solvent.[29] From the peak of constant-volume heat capacity, they determined ODT to be $\chi^*N \equiv z\epsilon^*_{\mathrm{AB}}N = 40.5$, where $z = 12$ is the lattice coordination number.[29] The mean-field ODT was determined to be $\chi^*_{\mathrm{MF}}N = 14.654$ using lattice SCF calculations based on the same model system as used in their simulations.[30]

Using fast off-lattice Monte Carlo (FOMC) simulations in an isothermal-isobaric ensemble, de Pablo and co-workers studied compressible symmetric DBC melts modeled by discrete Gaussian chains (DGC) of $N = 64$ with a position-independent but anisotropic pair potential of cubic symmetry.[31] They determined χ^*N by calculating the chemical potentials of the disordered and lamellar phases.[31] Note that their χ^*N was renormalized to take into account the short-range correlations (due to the finite interaction range used in their simulations) approximately; their $\chi^*_{\mathrm{MF}}N$ was therefore determined using the random-phase approximation for DGC with Dirac δ-function interactions.[31,34]

Müller and Daoulas performed single-chain-in-mean-field (SCMF) simulations to study compressible symmetric DBC melts modeled by DGC of $N = 32$, and determined $\chi^* N = 13.65 \pm 0.1$ by comparing the free energies of the disordered and lamellar phases.[32] Their SCMF simulation is similar to canonical-ensemble FOMC simulation with a spatial discretization scheme (i.e., with a position-dependent and anisotropic pair potential),[26] except that the second-order term in the energy difference due to MC trial moves is neglected by the quasi-instantaneous field approximation[35] (i.e., the detailed balance condition is not satisfied). They also estimated $\chi^*_{\rm MF} N = 11.7 \pm 0.5$ by fitting the lamellar composition profiles (averaged over directions parallel to the lamellar interfaces) of a system with $\bar{\mathcal{N}} \approx 2.5 \times 10^9$ at various $\chi > \chi^*_{\rm MF}$ to a sinusoidal function and then extrapolating the so-obtained amplitude of the profiles to 0.[32]

Finally, with the standard model, Fredrickson and co-workers performed field-theoretic simulations in a canonical ensemble and determined $\chi^* N = 12.2$ (for slightly asymmetric DBC with $f = 0.49$) by comparing the free energies of the disordered and lamellar phases.[33] For this model, $\chi^*_{\rm MF} N = 10.495$ at $f = 1/2$ is the well-known Leibler's result[36] and is used in Fig. 2.2. This study represents the most stringent test of the FH prediction to date and reveals large inaccuracy of the latter. Overall, with the different models and methods used and the scarce simulation data in Fig. 2.2, it is clear that the ODT shift of symmetric DBC due to fluctuations is a problem far from being well understood.

Here we report the first systematic study using FOMC simulations with experimentally accessible fluctuations to unambiguously quantify the ODT shift of symmetric DBC from the mean-field prediction. Different from Ref. [31], exactly the same model system (Hamiltonian) with an isotropic pair potential is used in both our simulations and mean-field theory; the ODT shift is therefore due to the fluctuations/correlations neglected by the latter. In addition, our simulations are performed in a canonical ensemble, thus avoiding the fluctuations of $\bar{\mathcal{N}}$ during a simulation run. We further use the multiple histogram reweighting technique[37] with a novel order parameter to accurately locate ODT. Last but not least, we

vary all the parameters in our model system to examine their effects on the ODT shift. We emphasize again that our purpose here is not to test FH[6] or other[23] fluctuation theories based on the standard model, which, albeit its simplicity (i.e., with only $\bar{\mathcal{N}}$ affecting the ODT shift), cannot be directly used and tested in molecular simulations. In models that can be used in such simulations, other parameters (i.e., finite values of N, compressibility and interaction range, as well as the form of pair-potential) are inevitable and expected to affect the ODT shift.[26,38] Due to the lack of advanced fluctuation theories that take into account the effects of these model parameters, however, it is difficult to extract relevant experimental implications directly from such simulations as reported here. To highlight the importance of quantitative and parameter-fitting-free comparisons among different models/methods, we will revisit the comparisons made by Groot and Madden[39] between their dissipative particle dynamics (DPD) simulations and the SCF calculations of the standard model for DBC melts[40] in Chapter 3.

2.2 Model and Methods

2.2.1 Model System

We consider compressible symmetric DBC melts of n chains each of N segments in volume V at the thermodynamic temperature T. The Hamiltonian of our model system is given by $\mathcal{H} = \mathcal{H}^C + \mathcal{H}^E_\kappa + \mathcal{H}^E_\chi$, where

$$\mathcal{H}^C = \frac{3k_BT}{2a^2}\sum_{k=1}^{n}\sum_{s=1}^{N-1}\left(\mathbf{R}_{k,s+1}-\mathbf{R}_{k,s}\right)^2$$

is due to the chain connectivity modeled by DGC, with k_B being the Boltzmann constant, a the effective bond length, and $\mathbf{R}_{k,s}$ the spatial position of the s^{th} segment on the k^{th} chain;

$$\mathcal{H}^E_\kappa = \frac{1}{2\kappa\rho_0}\int \mathrm{d}\mathbf{r}\mathrm{d}\mathbf{r}'\left[\hat{\rho}_{\mathrm{A}}(\mathbf{r})+\hat{\rho}_{\mathrm{B}}(\mathbf{r})\right]u_0(|\mathbf{r}-\mathbf{r}'|)\left[\hat{\rho}_{\mathrm{A}}(\mathbf{r}')+\hat{\rho}_{\mathrm{B}}(\mathbf{r}')\right]-\frac{nN}{2\kappa\rho_0}u_0(0) \qquad (2.1)$$

is due to the system compressibility, with κ denoting the generalized Helfand compressibility[41] for the copolymer melts, $\rho_0 \equiv nN/V$, $\hat{\rho}_{\mathrm{A}}(\mathbf{r}) \equiv \sum_{k=1}^{n}\sum_{s=1}^{N_{\mathrm{A}}}\delta(\mathbf{r}-\mathbf{R}_{k,s})$ and

$\hat{\rho}_{\rm B}(\mathbf{r}) \equiv \sum_{k=1}^{n} \sum_{s=N_{\rm A}+1}^{N} \delta(\mathbf{r} - \mathbf{R}_{k,s})$ being the microscopic number density of A and B segments at spatial position $\mathbf{r}$, respectively, $N_{\rm A} = N/2$ for symmetric DBC, and the last term deducting the self-interaction; and

$$\mathcal{H}_{\chi}^{E} = \frac{\chi}{\rho_0} \int \mathrm{d}\mathbf{r}\mathrm{d}\mathbf{r}' \hat{\rho}_{\rm A}(\mathbf{r}) u_0(|\mathbf{r} - \mathbf{r}'|) \hat{\rho}_{\rm B}(\mathbf{r}') \tag{2.2}$$

is due to the repulsion between A and B segments, with χ denoting the generalized Flory-Huggins parameter. The non-bonded pair potential

$$u_0(r) = \begin{cases} (15k_BT/2\pi\sigma^3)(1 - r/\sigma)^2 & \text{if } r < \sigma \\ 0 & \text{otherwise} \end{cases},$$

is normalized (i.e., $\int \mathrm{d}\mathbf{r} u_0(|\mathbf{r}|) = k_BT$) and isotropic (i.e., depends only on the distance r between two segments) with σ denoting the finite interaction range. Note that $u_0(r)$ is essentially the same as the potential for the conservative force used in DPD simulations;[42] its Fourier transform is positive definite, thus avoiding the formation of clustered crystals at large ρ_0.[43]

Taking $R_{e,0} = \sqrt{N-1}a$ as the length scale, we have five parameters in this model: $\bar{\mathcal{N}}$, χN, N/κ, N, and $\sigma/R_{e,0}$ (or equivalently σ/a); the first three are physical parameters that can be mapped to an experimental system, and the last two characterize chain discretization and finite interaction range, respectively.

2.2.2 Simulation Methodologies

Our FOMC simulations are performed in a canonical ensemble using a variable-length, rectangular parallelepipedal simulation box with periodic boundary conditions applied in all directions. As evident from Eqs. (2.1) and (2.2), the strength of non-bonded interactions between two segments depends on the average segment number density ρ_0; this feature of using soft potentials is different from using hard excluded-volume interactions. We therefore use a canonical ensemble, instead of an isothermal-isobaric ensemble,[31] to avoid the fluctuations of ρ_0 (thus $\bar{\mathcal{N}}$). We note that FOMC simulations can also be performed in a

variable-density ensemble (e.g., an isothermal-isobaric or a grand-canonical ensemble). Here we take FOMC simulations of homopolymer melts in an isothermal-isobaric (nPT) ensemble as an example; generalization to DBC melts and other variable-density ensembles (e.g., the grand-canonical ensemble) is straightforward. First of all, the segment interaction strength $\epsilon_\kappa \equiv (N/\kappa)/N\rho_0$ in Eq. (2.1) must be kept constant during a simulation run, which can be specified at the beginning of an nPT simulation by the input value of compressibility $(N/\kappa)_0$ and the initial volume V_0, i.e., $\epsilon_\kappa = (N/\kappa)_0/(N^2 n/V_0)$. During the simulation, ρ_0 fluctuates and cannot be used in the calculation of $\mathcal{H}_\kappa^E$; instead, the specified value of ϵ_κ should be used. Once the simulation is done, the actual value of compressibility can then be found as $N/\kappa = (N/\kappa)_0 V_0/\langle V\rangle$; in other words, the simulation is actually performed at N/κ and $\bar{\mathcal{N}} = \left(nR_{e,0}^3/\langle V\rangle\right)^2$, which are not known a priori, instead of $(N/\kappa)_0$ and $\bar{\mathcal{N}}_0 = \left(nR_{e,0}^3/V_0\right)^2$.

Our trial moves include hopping,[26] reptation,[26] pivot, and box-length change, for which the Metropolis acceptance criterion is used. In our pivot trial move, the shorter portion of a chosen chain is rotated around a segment (referred to as the pivot center) instead of a bond.[44] The pivot center is randomly chosen from all segments except chain ends. The shorter portion of the chain on which the pivot center resides is then randomly rotated around the spatial position of the pivot center, $\mathbf{R}_c$; the new position of a rotated segment is given by $\mathbf{R}_{\text{new}} = \mathbf{T}(\mathbf{R}_{\text{old}} - \mathbf{R}_c) + \mathbf{R}_c$, where $\mathbf{R}_{\text{old}}$ is the spatial position of the rotated segment before the trial move, and the rotation matrix

$$\mathbf{T} = \begin{bmatrix} q_0^2+q_1^2-q_2^2-q_3^2 & 2(q_1q_2+q_0q_3) & 2(q_1q_3-q_0q_2) \\ 2(q_1q_2-q_0q_3) & q_0^2-q_1^2+q_2^2-q_3^2 & 2(q_2q_3+q_0q_1) \\ 2(q_1q_3+q_0q_2) & 2(q_2q_3-q_0q_1) & q_0^2-q_1^2-q_2^2+q_3^2 \end{bmatrix}$$

with the four random numbers satisfying $q_0^2+q_1^2+q_2^2+q_3^2 = 1$ and generated using the method of Vesely.[45] We note that the very efficient pivot trial move cannot be used in many-chain simulations with hard excluded-volume interactions due to its extremely small acceptance rates.[46] With soft potential, however, we can achieve acceptance rates of about 50% at $N/\kappa = 0$ and $8 \sim 20\%$ at $N/\kappa = 50$ in our FOMC simulations near ODT. (See Sec. 2.2.3.)

In our box-length change trial move, without loss of generality, we generate the new box length along the x direction as $L_{x,\text{new}} = L_{x,\text{old}} \exp(\xi)$, where $L_{x,\text{old}}$ is the box length before the trial move and ξ a random number uniformly distributed within $(-\xi_{\max}, \xi_{\max})$, and set the box lengths along the other two directions to be the same (i.e., $L_y = L_z$), which are varied accordingly to keep V constant. The spatial positions of all segments are then re-scaled in each direction. We note that, in simulations of periodic structures such as lamellae, our box-length change trial move avoids the limitation of periodic boundary conditions on the orientation (thus the period) of the structure.[47] In Sec. 2.3.2.4, we compare our variable-box simulations with the commonly used fixed-box simulations to highlight such effects on ODT.

To further improve our sampling efficiency, we use the replica-exchange (RE)[48] of configurations at different χ-values, which greatly reduces the sample correlation length. The acceptance criterion for swapping two configurations i and j at χ_i and χ_j, respectively, is $P_{\text{acc}} = \min\{1, \exp[(\chi_i N - \chi_j N)(E_{\chi,i} - E_{\chi,j})]\}$ with $E_\chi \equiv \mathcal{H}^E_\chi / \chi N$.

In this work, the initial configuration of each run is randomly generated. Unless specified otherwise, the fractions of hopping, pivot and box-length change trial moves are 0.9, 0.05 and 0.00003, respectively, with the rest for reptation. About 50% acceptance rates are achieved for hopping and box-length change trial moves by adjusting their maximum displacement at the beginning of equilibration. Before RE is performed, we run several simulations to estimate the χN-range of ODT. For given $\bar{\mathcal{N}}$, N/κ, N and σ/a, we then use $R = 10 \sim 40$ replicas within the estimated χN-range with RE attempted every 10 Monte Carlo steps (MCS), where one MCS is defined as on average one trial move for every segment in the system; this gives an acceptance rate of RE about $60 \sim 85\%$. We use $3 \sim 8 \times 10^5$ MCS for equilibration and collect samples every 10 MCS for the subsequent $1 \sim 4 \times 10^6$ MCS.

2.2.3 On the Pivot Acceptance Rate

Pivot algorithm has been proven to be very efficient for sampling chain conformations.[49] It has been successfully applied to single-chain systems in both lattice and off-lattice simulations, but its application to many-chain systems with hard excluded-volume interactions is rather limited due to its extremely low acceptance rates.[46] To the best of our knowledge, no application of pivot to many-chain systems with soft potentials has been reported yet.

Here we first examine the pivot acceptance rate f_P in homopolymer melts (i.e., $\chi = 0$), where we use a cubic box of $V/R_{e,0}^3 = 20$ and fix $N = 10$ and $\sigma/a = 0.3$. In these simulations, hopping, reptation and pivot trial moves occur with a fraction of 0.9, 0.05 and 0.05, respectively. Fig. 2.3(a) shows f_P as a function of N/κ at $\bar{\mathcal{N}} = 10^4$. An exponential decay, i.e., $f_P \propto \exp(-kN/\kappa)$, is found with different k-values at small and large N/κ; this is similar to Fig. 2 of Ref. [46] showing f_P as a function of polymer volume fraction in their conventional lattice Monte Carlo simulations with the self- and mutual-avoiding walk. The exponential behavior is clearly in accordance with the Metropolis acceptance criterion, and the change of k was attributed by Olaj et al. to the fact that f_P is an average acceptance rate over the trial moves with different numbers of rotated segments N_P.[46] In our case, we can write $f_P \propto \sum_{N_P=1}^{4} \exp[-(N/\kappa)N_P C]/4$ with C assumed constant. At small N/κ, the Taylor expansion gives $f_P \propto \exp[-2.5(N/\kappa)C]$; while at large N/κ, only $N_P = 1$ (i.e., end-rotation) contributes significantly to f_P, leading to $f_P \propto \exp[-(N/\kappa)C]$. This is supported by our fitted k-values given in Fig. 2.3(a).

Fig. 2.3(b) shows f_P as a function of $\bar{\mathcal{N}}$ at $N/\kappa = 20$ and 50. The smallest $\bar{\mathcal{N}}$ ($= 2.5\times10^{-3}$) here corresponds to a single chain in the box, where $f_P \approx 0.96$ is hardly influenced by N/κ. As $\bar{\mathcal{N}}$ increases, f_P exhibits a minimum before $\bar{\mathcal{N}}_{\rm cp} = 2\times10^4$ in both cases. This is due to two competing effects: the increased segmental density (or reduced void fraction) and the decreased segment repulsion strength $1/\kappa\rho_0 = (N/\kappa)R_{e,0}^3/N^2\sqrt{\mathcal{N}}$ (see Eq. (2.1)). While the latter also makes f_P to further increase with increasing $\bar{\mathcal{N}} > \bar{\mathcal{N}}_{\rm cp}$, another reason for this nice behavior is the increased homogeneity of the segmental distribution, which leads to

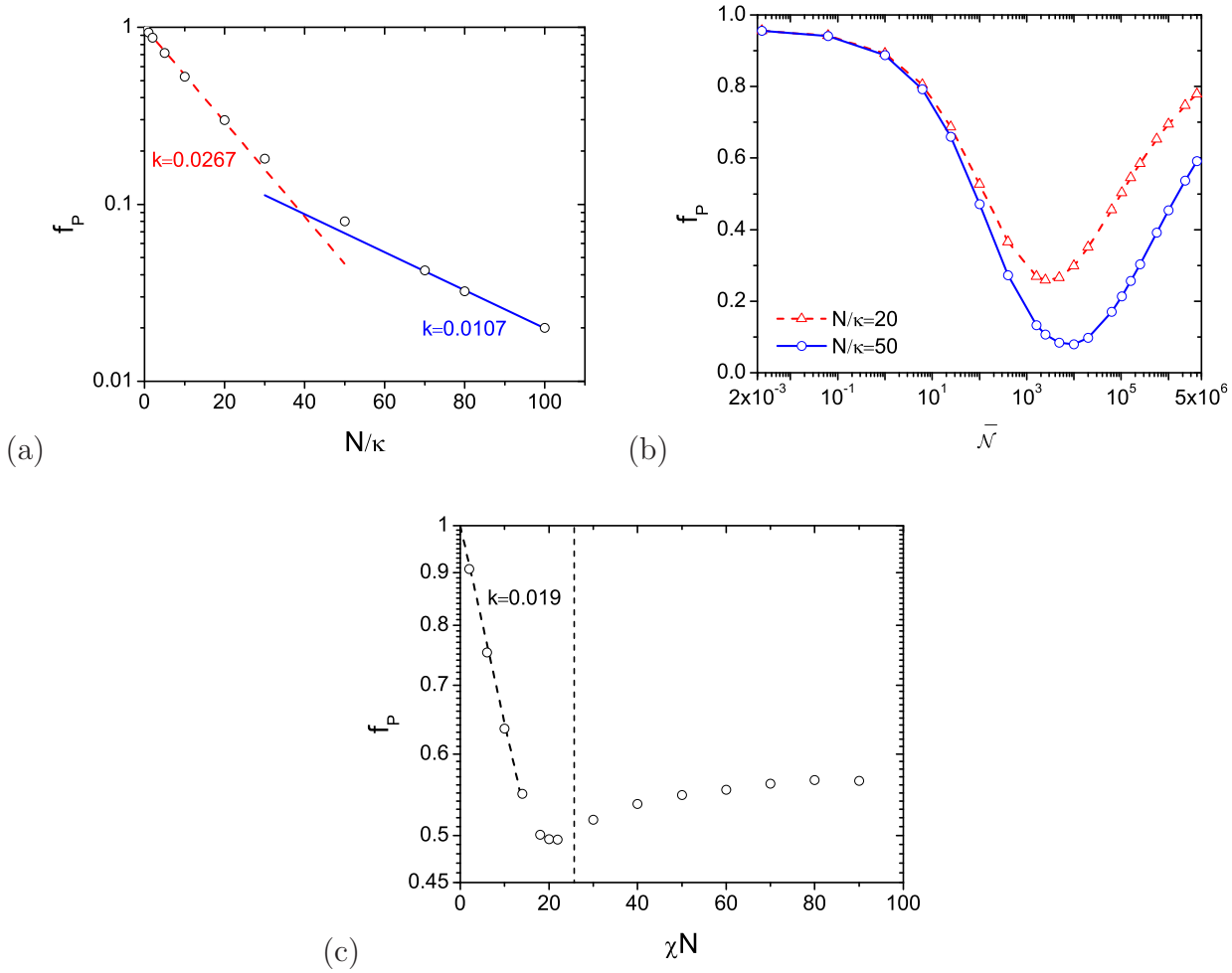

Figure 2.3: Semi-logarithmic plots of pivot acceptance rate f_P as a function of (a) N/κ in our fixed-box simulations of homopolymer melts with $\chi N = 0$ and $\bar{\mathcal{N}} = 10^4$, (b) $\bar{\mathcal{N}}$ in our fixed-box simulations of homopolymer melts with $\chi N = 0$, and (c) χN in our variable-box simulations of symmetric DBC melts with $N/\kappa = 0$ and $\bar{\mathcal{N}} = 10^4$. The negative slope k is given next to each fitted line, and the vertical line in part (c) marks $\chi^* N = 25.67$. $N = 10$ and $\sigma/a = 0.3$.

decreased energy difference caused by the pivot trial move. Clearly, in the limit of $\bar{\mathcal{N}} \to \infty$, the system is homogeneous without any fluctuations, and f_P should be 1. Overall, very good acceptance rates are achieved over a broad range (more than nine orders of magnitude) of $\bar{\mathcal{N}}$ in homopolymer melts.

Next, we examine the influence of χ on f_P in symmetric DBC melts, where we use variable-box simulations with $V/R_{e,0}^3 = 19.26$ and fix $N = 10$, $\sigma/a = 0.3$, $N/\kappa = 0$ and

$\bar{\mathcal{N}} = 10^4$. Fig. 2.3(c) shows f_P as a function of χN, where the vertical line marks the ODT $\chi^* N$. We see that f_P exponentially decreases with increasing χ well below χ^*, where the system is in the homogeneous (disordered) phase; this exponential decay is again in accordance with the Metropolis acceptance criterion. f_P then exhibits a minimum around χ^* and slightly increases with increasing $\chi > \chi^*$. This is because in our pivot algorithm we rotate the shorter portion of the selected chain; once lamellae form, the rotated A (B) segments are more likely to be within the A (B) domain, with less chance to overlap with B (A) segments than in the disordered phase. Increasing $\chi > \chi^*$ results in more segregated A and B domains with larger lamellar spacing, thus the slight increase of f_P. Very good acceptance rates can therefore also be achieved in ordered block copolymers.

2.2.4 Multiple Histogram Reweighting with a Novel Order Parameter

To accurately locate ODT in our FOMC simulations, we use a new scalar order parameter characterizing the degree of positional order in lamellae. In simulations of periodic structures such as lamellae, the periodic boundary conditions limit the allowed orientations of the structure and thus its period. In particular, for lamellae with a normal direction $\mathbf{n}$ in a rectangular parallelepipedal simulation box with length L_j in the $\mathbf{j}(= \mathbf{x}, \mathbf{y}, \mathbf{z})$ direction (and periodic boundary conditions applied in all directions), $L_j \mathbf{j} \cdot \mathbf{n} = n_j L(\mathbf{n})$ must be satisfied, where n_j is the number of periods contained in the box along the $\mathbf{j}$ direction (which is a non-negative integer) and L the lamellar period corresponding to $\mathbf{n}$; this gives $L = 1 \Big/ \sqrt{\sum_{\mathbf{j}} (n_j / L_j)^2}$.[47] For a fixed-length box as commonly used in canonical-ensemble simulations, both the lamellar orientation and its period are therefore discretized (i.e., L can hardly be the natural lamellar period L_0). This problem is the most severe for cubic boxes;[47] on the other hand, however, we can take advantage of this and use cubic boxes to control L in the simulations, as shown in Sec. 2.3.2.4.

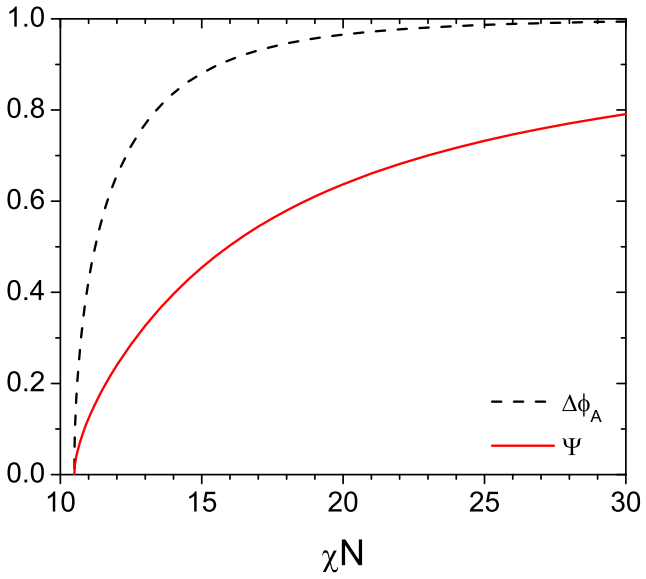

Figure 2.4: The order parameter Ψ and the oscillation amplitude $\Delta\phi_{\rm A}$ obtained from SCF calculations of the standard model of symmetric DBC. Both Ψ and $\Delta\phi_{\rm A}$ are 0 in the disordered phase (i.e., for $\chi N < 10.495$).

For a given direction $\mathbf{n}$, we calculate the volume fraction of A segments $\phi_{\rm A}(t) \equiv \hat{\rho}_{\rm A}(t)/[\hat{\rho}_{\rm A}(t) + \hat{\rho}_{\rm B}(t)]$ as a function of position t along $\mathbf{n}$ in a collected configuration (averaged over directions perpendicular to $\mathbf{n}$), where the spatial positions of all segments in the system is mapped into the interval $0 \le t < L(\mathbf{n})$ according to the periodic boundary conditions, and then $\psi(\mathbf{n}) \equiv \left|\int {\rm d}t \exp[4\pi i t/L(\mathbf{n})] f(t)\right| / \int {\rm d}t f(t)$ with $f(t) \equiv 1 - |2\phi_{\rm A}(t) - 1|$ and $i \equiv \sqrt{-1}$. Finally, we define the order parameter $\Psi \in [0, 1]$ for a collected configuration as the largest ψ over all possible lamellar orientations in the box with L larger than some lower-limit estimate of L_0, and the L corresponding to $\psi = \Psi$ as the lamellar period of this configuration. As an example, Fig. 2.4 compares Ψ with the oscillation amplitude $\Delta\phi_{\rm A}$ of the A-segment volume fraction in the direction perpendicular to the lamellar interfaces, both obtained from SCF calculations of the standard model of symmetric DBC, as a function of χN. While they exhibit similar behavior, $\Delta\phi_{\rm A}$ is very susceptible to the system fluctuations, but Ψ, as a quantity averaged over the spatial positions of all segments, is not and can therefore be used as an order parameter in simulations.

With the new order parameter Ψ, we use the multiple histogram reweighting technique[37] to analyze our simulation data, which is nicely combined with RE. For totally R simulation runs performed at the same $\bar{\mathcal{N}}$, N/κ, N and σ/a but different χ_i ($i = 1, \ldots, R$), we collect the histogram $H_i(E_\chi, \Psi)$ at each χ_i. The probability for the system having E_χ and Ψ at χ is then given by

$$p_b(E_\chi, \Psi|\chi) = \frac{\sum_{i=1}^{R} g_i^{-1} H_i(E_\chi, \Psi) \exp(\chi N E_\chi)}{\sum_{j=1}^{R} g_j^{-1} M_j H_j(E_\chi, \Psi) \exp(\chi_j N E_\chi - C_j)},$$

where g_j is the statistical inefficiency of the collected E_χ in the j^{th} run, M_j is the total number of collected samples after equilibration in the j^{th} run, and $\exp(C_j) = \sum_{E_\chi} \sum_{\Psi} p_b(E_\chi, \Psi|\chi_j)$; note that $\exp(C_j)$ is proportional to the canonical-ensemble partition function at χ_j.[50] This allows us to accurately locate ODT in simulations, as described in Sec. 2.3.2.1.

2.2.5 Advantages

Here we briefly summarize the advantages of our methods compared with previous simulation studies on the ODT of symmetric DBC. First of all, hard excluded-volume interactions are used in most of such studies[28–30] reported in the literature. This not only limits $\bar{\mathcal{N}} \lesssim 10^2$, but also significantly slows down the chain relaxation towards equilibrium configurations and efficient sampling of configuration space. As shown in Ref. [26], using soft potentials can lead to several orders of magnitude faster/better sampling. It also allows the use of very efficient trial moves such as the pivot algorithm, which further improves our sampling. Clearly, efficient sampling is crucial for the study of phase transitions such as ODT.

Second, our variable-box simulations avoid the limitation of periodic boundary conditions on the lamellar period (which in turn affects ODT as shown in Sec. 2.3.2.4), thus allowing accurate determination of both L_0 and ODT. While such limitation could be alleviated by using large (fixed) box sizes, the difficulty of efficiently sampling configuration space increases exponentially with the system volume.

Third, our use of replica exchange ensures sufficient sampling of configuration space; as an example, Fig. 2.5 clearly shows that an (arbitrarily chosen) replica during our simulation

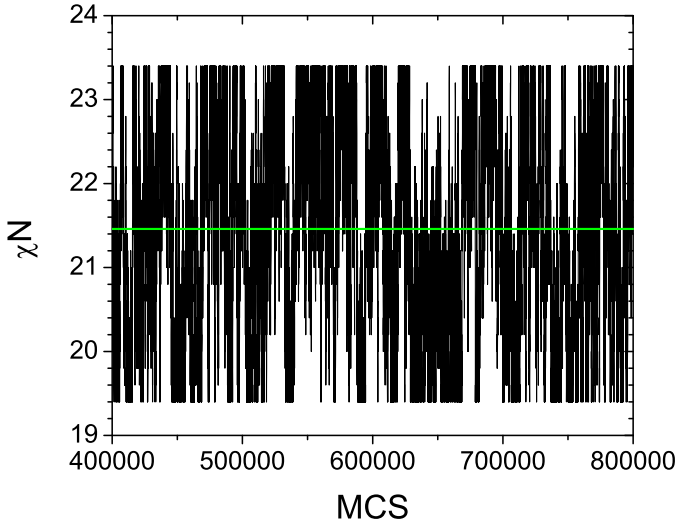

Figure 2.5: The χN value of an arbitrarily chosen replica as a function of Monte Carlo step (MCS) for the case of $N = 20$, $\bar{\mathcal{N}} = 10^4$, $\sigma/a = 0.3$, and $N/\kappa = 0$ after equilibration, where totally 21 replicas and 2,435,000 MCS are used, and the green horizontal line marks the ODT determined at $\chi^* N = 21.46 \pm 0.07$.

frequently crosses the ODT. In contrast, the occurrence of hysteresis and only one phase during a simulation run is a clear indication of insufficient sampling.

Last but not least, our use of multiple histogram reweighting with a novel order parameter ensures unambiguous classification of the two phases and the most accurate determination of ODT (within our sampling error). While the only simulations of ODT using replica exchange were reported by Beardsley and Matsen using a lattice model with hard excluded-volume interactions,[29] the lack of multiple histogram reweighting limits the accuracy of their ODT. On the other hand, using an order parameter is essential to simulations of phase transitions such as ODT. Although using different order parameters may give slightly different results due to the system fluctuations and finite size, it is just arbitrary and unreliable, particularly when close to the phase transition point, to classify the configurations from simulations into different phases without an order parameter.

Our methods having all of these advantages therefore give the most accurate simulation data of ODT and L_0 reported to date, which can be used to quantitatively test advanced fluctuation theories. This is the purpose of our work.

2.3 Results and Discussion

2.3.1 Mean-Field ODT

For the same model system as used in our FOMC simulations, we determine the mean-field ODT $\chi^*_{\rm MF}$ and the corresponding lamellar period $L^*_{0,\rm MF}$ using the random-phase approximation (RPA).[26] Table 2.2 lists $\chi^*_{\rm MF}N$ and $L^*_{0,\rm MF}/R_{e,0}$ for various N and σ/a. We see that, within our choice of parameter values (which is explained in Sec. 2.3.3), $\chi^*_{\rm MF}N$ can vary by more than 10%, comparable to the smallest ODT shift due to fluctuations. It is therefore important to use $\chi^*_{\rm MF}N$ of the same model system as in the simulations, so that the ODT shift due to fluctuations can be unambiguously quantified.

Table 2.2: Mean-field ODT $\chi^*_{\rm MF}N$ and corresponding lamellar period $L^*_{0,\rm MF}$

		$\sigma/a = 0.3$	$\sigma/a = 0.1\sqrt{19}$	$\sigma/a = 2/\sqrt{3}$
$N = 10$	$\chi^*_{\rm MF}N$	10.047		11.427
	$L^*_{0,\rm MF}/R_{e,0}$	1.356		1.495
$N = 20$	$\chi^*_{\rm MF}N$	10.405	10.462	11.102
	$L^*_{0,\rm MF}/R_{e,0}$	1.347	1.353	1.414

We also note that the mean-field results are independent of N/κ and $\bar{\mathcal{N}}$, and can be understood based on the Refs. [26,38]. Finally, the well-known Leibler's results[36] of $\chi^*_{\rm MF}N \approx 10.495$ and $L^*_{0,\rm MF}/R_{e,0} \approx 1.318$ are recovered in the limit of $N \to \infty$ ($a \to 0$) and $\sigma \to 0$, i.e., for continuous Gaussian chains with Dirac δ-function interactions.

2.3.2 ODT from FOMC Simulations

2.3.2.1 Determining ODT with order parameter

Using multiple histogram reweighting, we can interpolate with minimal error the simulation data at any χ within the range of our simulations. Fig. 2.6 shows the histograms of Ψ at various χ, $p_b(\Psi|\chi) \equiv \sum_{E_\chi} p_b(E_\chi, \Psi|\chi)$, which are normalized such that $\int_0^1 {\rm d}\Psi p_b(\Psi|\chi) = 1$ and exhibit a double peak near ODT; the peak at smaller Ψ corresponds to the disordered

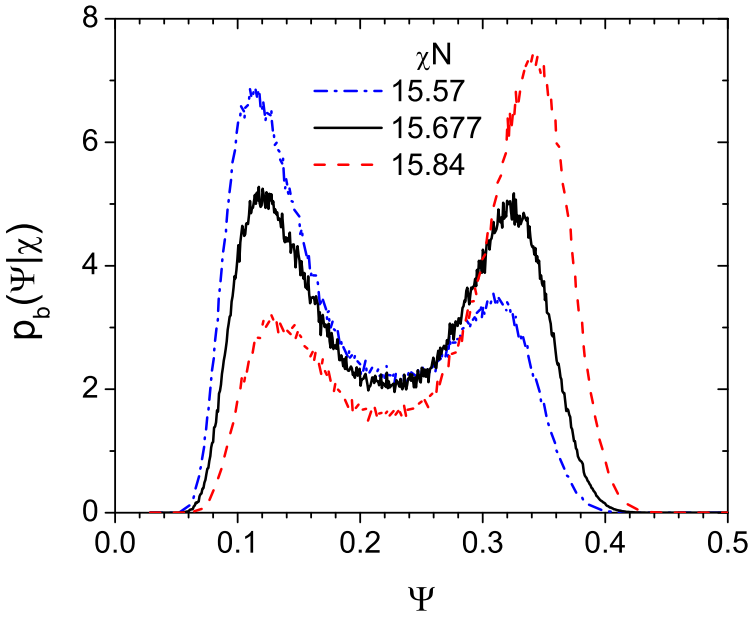

Figure 2.6: Reweighted histogram $p_b(\Psi|\chi)$ near ODT (where $\chi N = 15.677$) obtained from FOMC simulations at $N = 10$, $\sigma/a = 2/\sqrt{3}$, $N/\kappa = 50$, and $\bar{\mathcal{N}} = 2002$.

state, and that at larger Ψ corresponds to the ordered (lamellar) state. ODT χ^* is then determined according to the equal-weight criterion[51]

$$\int_0^{\Psi^*} \mathrm{d}\Psi p_b(\Psi|\chi^*) = \int_{\Psi^*}^1 \mathrm{d}\Psi p_b(\Psi|\chi^*),$$

where $\Psi^* \equiv \langle\Psi\rangle(\chi^*)$.

Once χ^* is determined, all samples with $\Psi < \Psi^*$ are considered as the disordered (D) phase, and the rest are considered as the lamellar (L) phase. Averaging Ψ over these two phases, respectively, gives $\langle\Psi\rangle_{\mathrm{D}}^* \equiv \int_0^{\Psi^*} \mathrm{d}\Psi p_b(\Psi|\chi^*)\Psi$ and $\langle\Psi\rangle_{\mathrm{L}}^* \equiv \int_{\Psi^*}^1 \mathrm{d}\Psi p_b(\Psi|\chi^*)\Psi$ at ODT. Furthermore, at given $\chi \geq \chi^*$, averaging the lamellar period over the lamellar phase gives the ensemble-averaged lamellar period $L_0(\chi)$; in particular, we denote the lamellar period at ODT as $L_0^* \equiv L_0(\chi^*)$. To estimate the statistical error of χ^*, we calculate it using the first- and second-half of our samples collected after equilibration, respectively, and take three times their largest deviation from χ^* determined using all the samples as the error bar; the statistical errors of other quantities here are similarly estimated.

Note that the difference in the Helmholtz free energy per chain f_c between the two phases at given χ can be calculated as $\beta\Delta f_c \equiv \beta(f_{c,\mathrm{D}} - f_{c,\mathrm{L}}) = \left[-\ln\int_0^{\Psi^*} \mathrm{d}\Psi p_b(\Psi|\chi) + \ln\int_{\Psi^*}^1 \mathrm{d}\Psi p_b(\Psi|\chi)\right] \Big/ n$; the above equal-weight criterion is therefore equivalent to setting $f_{c,\mathrm{D}}(\chi^*) = f_{c,\mathrm{L}}(\chi^*)$.[52]

2.3.2.2 Effects of $\bar{\mathcal{N}}$

In the thermodynamic limit, where both n and V go to infinity at given $\bar{\mathcal{N}}$, $p_b(\Psi)$ should be δ-function like, and we have $\langle\Psi\rangle_{\mathrm{D}}^* = 0$, $\langle\Psi\rangle_{\mathrm{L}}^* = 0$ in the limit of $\bar{\mathcal{N}} \to \infty$ due to the second-order ODT predicted by the mean-field theory (see Fig. 2.4), and $\langle\Psi\rangle_{\mathrm{L}}^* > 0$ at finite $\bar{\mathcal{N}}$ due to the fluctuation-induced first-order ODT.[6] In simulations (which are for finite-size systems at finite $\bar{\mathcal{N}}$), $p_b(\Psi)$ is rounded and $\langle\Psi\rangle_{\mathrm{L}}^* > \langle\Psi\rangle_{\mathrm{D}}^* > 0$ due to the system fluctuations. Fig. 2.7 shows $p_b(\Psi|\chi^*)$ obtained from our FOMC simulations at various $\bar{\mathcal{N}}$, where we see that, with increasing $\bar{\mathcal{N}}$ (thus decreasing system fluctuations), the double peak shifts towards smaller Ψ and becomes narrower (thus higher due to the normalization of $p_b(\Psi)$). To be more quantitative, we plot $\langle\Psi\rangle_{\mathrm{D}}^*$, $\langle\Psi\rangle_{\mathrm{L}}^*$, and $\langle\Psi\rangle_{\mathrm{L}}^* - \langle\Psi\rangle_{\mathrm{D}}^*$ vs. $\bar{\mathcal{N}}$ in Fig. 2.8, which shows that all of them monotonically decrease with increasing $\bar{\mathcal{N}}$ (at the same V) and approximately $\langle\Psi\rangle_{\mathrm{L}}^* \propto \bar{\mathcal{N}}^{-0.18}$. Our simulation results are therefore qualitatively consistent with the statement that fluctuations change the second-order ODT to a first-order one.

2.3.2.3 Finite-size effects

The shape of $p_b(\Psi)$, however, are quantitatively affected by the volume V in simulations. In the following we take the case of $N = 10$, $\sigma/a = 0.3$, $N/\kappa = 0$ and $\bar{\mathcal{N}} = 10^4$ as an example. While systematic study of the finite-size effects requires much more extensive simulations and is thus out of the scope of this paper, we have performed variable-box simulations at two different volumes for this case: those at $V/R_{e,0}^3 = 19.26$ give $\chi^* N = 25.67 \pm 0.23$ and $L_0^*/R_{e,0} = 1.463 \pm 0.001$ (which are used in the following), and those at $V/R_{e,0}^3 = 8.85$ give the corresponding values of 25.72 ± 0.23 and 1.458 ± 0.001. We therefore see that the finite-size effect on the ODT determined from our simulations ($< 0.2\%$) is negligible compared to

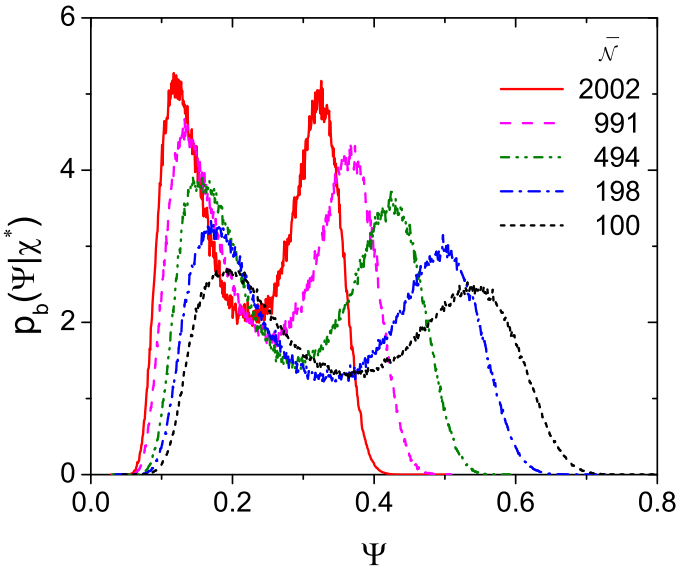

Figure 2.7: $p_b(\Psi|\chi^*)$ obtained from FOMC simulations at $N = 10$, $\sigma/a = 2/\sqrt{3}$, and $N/\kappa = 50$, where the ODT $\chi^* N$ at each $\bar{\mathcal{N}}$ is given in Table 2.4.

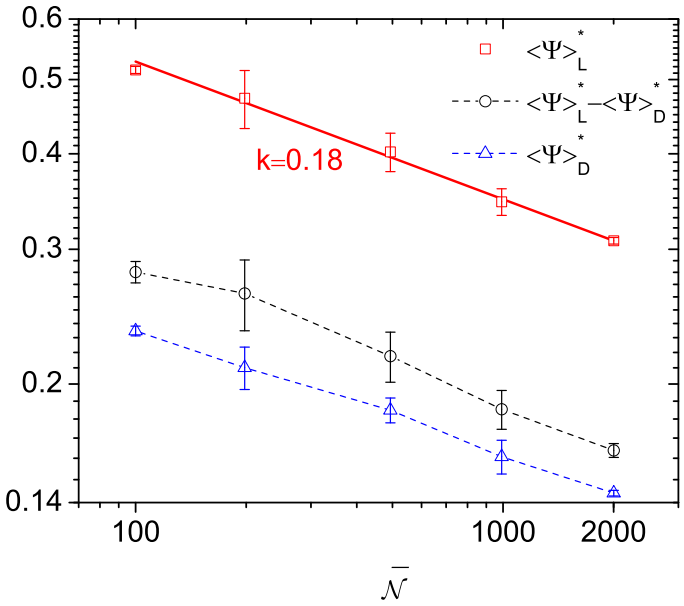

Figure 2.8: Logarithmic plot of the ensemble-averaged order parameter of the disordered and lamellar phases at ODT, $\langle\Psi\rangle^*_{\rm D}$ and $\langle\Psi\rangle^*_{\rm L}$, respectively, and their difference vs. $\bar{\mathcal{N}}$ for the cases shown in Fig. 2.7. The negative slope k is given next to the straight line.

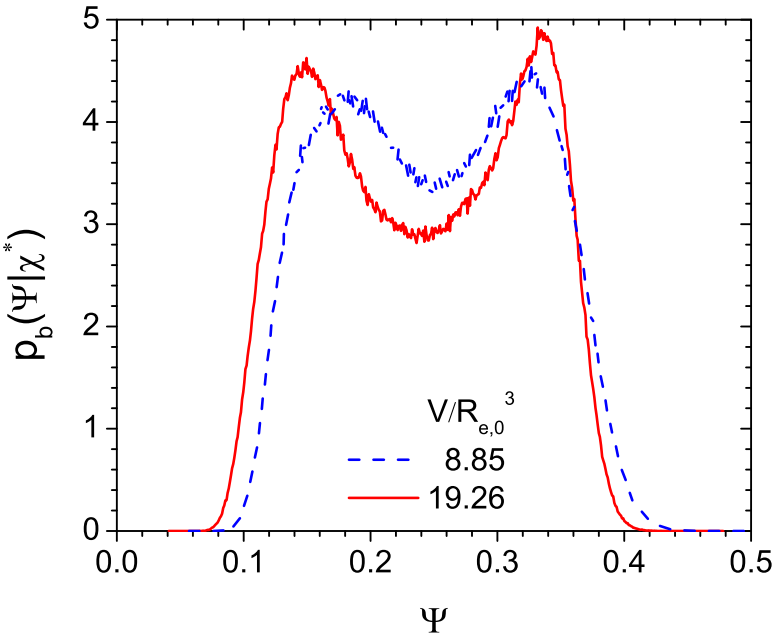

Figure 2.9: $p_b(\Psi|\chi^*)$ at different volume V obtained from FOMC simulations at $N = 10$, $\sigma/a = 0.3$, $N/\kappa = 0$, and $\bar{\mathcal{N}} = 10^4$, where the ODT $\chi^* N$ at each V is given in the main text.

its statistical error ($< 1\%$ in this case and $< 3\%$ in all the cases), although its effect on L_0^* is not.

Fig. 2.9 compares $p_b(\Psi|\chi^*)$ at these two volumes; we see that the two peaks are better separated at larger V, which then affects the values of $\langle\Psi\rangle_{\rm D}^*$ and $\langle\Psi\rangle_{\rm L}^*$. In particular, we have $\langle\Psi\rangle_{\rm D}^* = 0.167 \pm 0.004$ and $\langle\Psi\rangle_{\rm L}^* = 0.312 \pm 0.010$ at $V/R_{e,0}^3 = 19.26$, and $\langle\Psi\rangle_{\rm D}^* = 0.184 \pm 0.003$ and $\langle\Psi\rangle_{\rm L}^* = 0.318 \pm 0.005$ at $V/R_{e,0}^3 = 8.85$.

2.3.2.4 Effects of fixed-length boxes

Fixed-length boxes, particularly cubic boxes, are commonly used in canonical-ensemble simulations. For a cubic box of length L_b, let L_1 and L_2 be the lamellar period allowed in this box that is, respectively, the closest and the second-closest to the above L_0^*. We judiciously choose L_b such that $|L_2/L_0^* - 1| > 0.1$ and $|L_2/L_0^* - 1| - |L_1/L_0^* - 1| > 0.03$, then determine the ODT $\chi_f^* N$ and the corresponding lamellar period $L_{0,f}^*$ in fixed-box simulations using our method explained in Sec. 2.3.2.1; the results are listed in Table 2.3. It is confirmed that all

the collected configurations have only one lamellar period, namely $L_1 = L_b/\sqrt{2}$. In this way, we can precisely control the mismatch between $L^*_{0,f} = L_1$ and L^*_0 in fixed-box simulations.

To see the effects of such mismatch on ODT, we plot χ^*_f/χ^* vs. $L^*_{0,f}/L^*_0$ in Fig. 2.10. First of all, we see that $\chi^*_f < \chi^*$ even if $L^*_{0,f} = L^*_0$. This is because a fixed-length box limits the system fluctuations, thus inducing periodic structures and decreasing ODT. Second, we see that χ^*_f increases with increasing mismatch (i.e., $|L^*_{0,f}/L^*_0 - 1|$) in most cases. This is because the stretching/compression caused by a mismatched lamellar period makes the lamellae unstable, thus increasing ODT. These two opposite effects were pointed out by Beardsley and Matsen.[29] Third, our data from the fixed-box simulations are clearly not symmetric about $L^*_{0,f}/L^*_0 = 1$; cubic fitting of χ^*_f vs. $L^*_{0,f}$ (the curve in Fig. 2.10) indicates that the minimum of χ^*_f is around $L^*_{0,f}/L^*_0 = 1.03$ instead of 1. This asymmetry between the stretching and compression of lamellae is due to the fact that undulation, which occurs only when lamellae are stretched, reduces the frustration caused by a mismatched lamellar period and makes the lamellae stable, as pointed out by Guo and Kremer.[53] Last but not least, we note that the deviation in ODT caused by using a fixed-length box can be as large as 6%, clearly out of its statistical error. This highlights the importance of using variable-length boxes in our simulations.

Table 2.3: Box size L_b and ODT $\chi^*_f N$ in our fixed-box simulations. All the collected configurations have only one lamellar period, namely $L^*_{0,f} = L_1 = L_b/\sqrt{2}$.

$L_b/R_{e,0}$	$\chi^*_f N$
$\sqrt[3]{7.59}$	25.40 ± 0.05
$\sqrt[3]{8.08}$	24.99 ± 0.09
$\sqrt[3]{8.85}$	24.26 ± 0.02
$\sqrt[3]{9.70}$	24.12 ± 0.02
$\sqrt[3]{10.24}$	24.16 ± 0.02
$\sqrt[3]{10.84}$	24.57 ± 0.03
$\sqrt[3]{11.15}$	24.86 ± 0.17

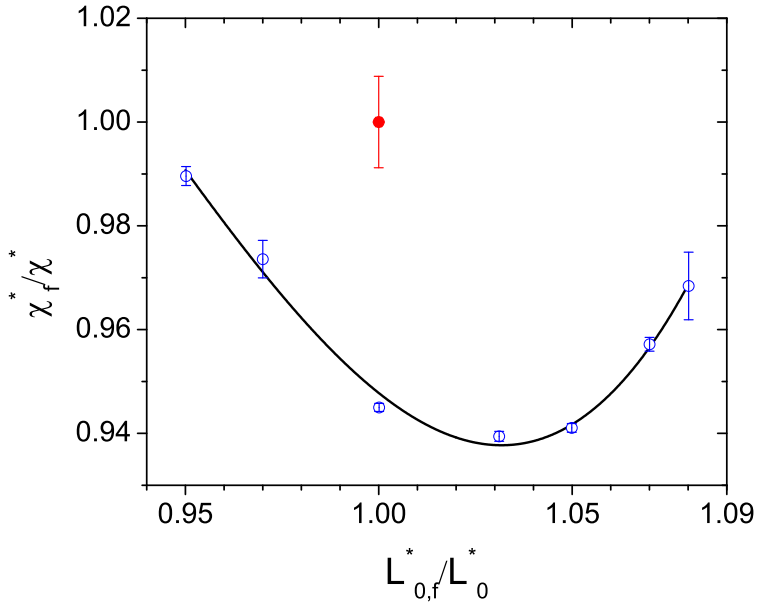

Figure 2.10: Effects of mismatched lamellar period on ODT. The open circles are from fixed-box simulations, and the filled one is from variable-box simulations. The solid curve shows the cubic fitting: $\chi^*_f/\chi^* = 41.17(L^*_{0,f}/L^*_0)^3 - 116.14(L^*_{0,f}/L^*_0)^2 + 108.18(L^*_{0,f}/L^*_0) - 32.26$. $N = 10$, $\sigma/a = 0.3$, $N/\kappa = 0$, and $\bar{\mathcal{N}} = 10^4$. See main text for details.

2.3.3 ODT Shift

Table 2.4 lists our parameters in variable-box simulations and the corresponding $\chi^* N$. Collecting all the data, Fig. 2.11 shows our results of ODT shift vs. $\bar{\mathcal{N}}$ at various N, σ/a and N/κ. We find $\chi^*/\chi^*_{\rm MF} - 1 \propto \bar{\mathcal{N}}^{-k}$ in all the cases. While this is consistent with the functional form of the FH prediction, our ODT shift is larger than their prediction for all the cases studied, in agreement with Refs. [29, 33]. In the cases of $\sigma/a = 0.3$ and $0.1\sqrt{19} \approx 0.44$, we also find that the negative exponent k decreases around $\bar{\mathcal{N}}_{\rm cp} = 2(N-1)^3/N^2(\sigma/a)^6$, which corresponds to the FCC close packing of polymer segments as hard spheres (where the volume fraction occupied by these spheres is given by $(4/3)\pi(\sigma/2)^3 nN/V = \pi/3\sqrt{2}$). This is therefore due to the local packing of segments (i.e., the short-range correlations).

Table 2.4: Our parameters in variable-box simulations and results of ODT.

N (n)	σ/a	N/κ	$\bar{\mathcal{N}}$	$\chi^* N$	$L_0^*/R_{e,0}$
10 (1300)	0.3	0	7000	34.07 ± 0.20	1.4727 ± 0.0033
10 (1926)	0.3	0	10000	25.67 ± 0.23	1.4631 ± 0.0011
10 (1926)	0.3	0	20000	18.18 ± 0.09	1.4291 ± 0.0012
10 (1926)	0.3	0	50000	14.74 ± 0.06	1.4193 ± 0.0022
10 (1926)	0.3	0	99978	12.99 ± 0.06	1.4013 ± 0.0052
10 (1926)	0.3	50	10000	81.66 ± 0.54	1.4882 ± 0.0010
10 (1926)	0.3	50	14000	55.33 ± 0.16	1.4648 ± 0.0067
10 (1926)	0.3	50	20000	39.40 ± 0.08	1.4530 ± 0.0080
10 (1926)	0.3	50	50000	23.07 ± 0.04	1.4415 ± 0.0002
10 (1926)	0.3	50	99978	17.90 ± 0.02	1.4154 ± 0.0078
10 (270)	$2/\sqrt{3}$	0	100	48.81 ± 0.61	1.8832 ± 0.0018
10 (380)	$2/\sqrt{3}$	0	198	32.00 ± 0.57	1.8159 ± 0.0069
10 (600)	$2/\sqrt{3}$	0	494	21.61 ± 0.63	1.7338 ± 0.0051
10 (850)	$2/\sqrt{3}$	0	991	17.71 ± 0.03	1.6791 ± 0.0004
10 (2454)	$2/\sqrt{3}$	0	2000	15.28 ± 0.12	1.6298 ± 0.0049
10 (270)	$2/\sqrt{3}$	50	100	31.37 ± 0.13	1.9816 ± 0.0008
10 (380)	$2/\sqrt{3}$	50	198	24.58 ± 0.62	1.8830 ± 0.0050
10 (600)	$2/\sqrt{3}$	50	494	19.70 ± 0.06	1.7939 ± 0.0100
10 (850)	$2/\sqrt{3}$	50	991	17.25 ± 0.06	1.7338 ± 0.0029
10 (1208)	$2/\sqrt{3}$	50	2002	15.68 ± 0.03	1.6892 ± 0.0100
20 (600)	$0.1\sqrt{19}$	0	1000	57.81 ± 0.76	1.5739 ± 0.0039
20 (1000)	$0.1\sqrt{19}$	0	2000	28.27 ± 0.92	1.5313 ± 0.0077
20 (1926)	$0.1\sqrt{19}$	0	5000	17.21 ± 0.37	1.4561 ± 0.0164
20 (1926)	$0.1\sqrt{19}$	0	10000	15.72 ± 0.10	1.4585 ± 0.0027
20 (1926)	$0.1\sqrt{19}$	0	30000	14.40 ± 0.03	1.4200 ± 0.0032
20 (1926)	$0.1\sqrt{19}$	0	50000	12.89 ± 0.10	1.4146 ± 0.0011
20 (1926)	$0.1\sqrt{19}$	0	1000	12.086 ± 0.004	1.3934 ± 0.0018
20 (800)	0.3	0	10000	21.46 ± 0.07	1.4358 ± 0.0030
20 (1150)	0.3	0	20664	16.84 ± 0.10	1.4230 ± 0.0015
20 (1750)	0.3	0	47852	14.30 ± 0.02	1.4086 ± 0.0005
20 (2116)	0.3	0	69960	13.58 ± 0.05	1.4012 ± 0.0010
20 (2530)	0.3	0	100014	13.09 ± 0.14	1.3967 ± 0.0015
20 (470)	$2/\sqrt{3}$	0	303	33.63 ± 0.35	1.7260 ± 0.0032
20 (604)	$2/\sqrt{3}$	0	500	25.31 ± 0.19	1.6751 ± 0.0006
20 (854)	$2/\sqrt{3}$	0	1000	19.95 ± 0.14	1.6244 ± 0.0029
20 (270)	$2/\sqrt{3}$	50	100	40.89 ± 0.19	1.9504 ± 0.0104
20 (604)	$2/\sqrt{3}$	50	500	22.75 ± 0.02	1.7490 ± 0.0045
20 (854)	$2/\sqrt{3}$	50	1000	18.82 ± 0.18	1.6809 ± 0.0046

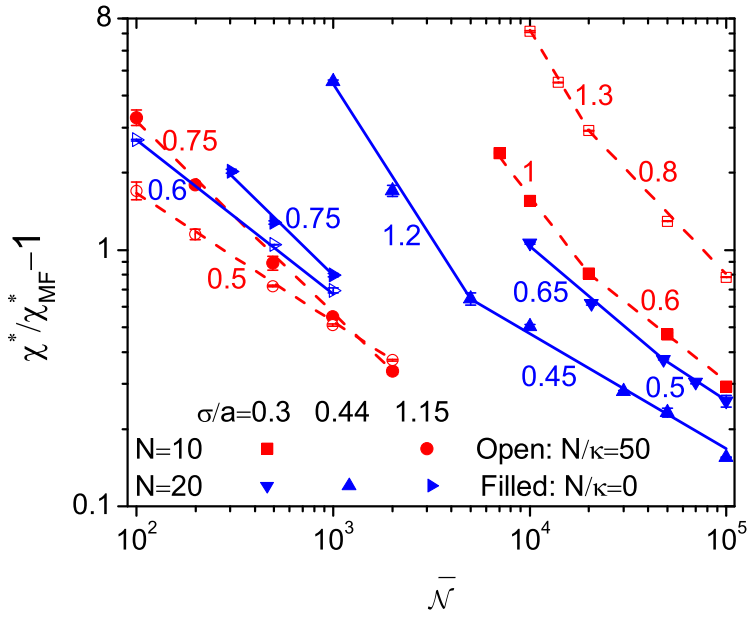

Figure 2.11: Logarithmic plot of our results of the ODT shift of symmetric DBC as a function of $\bar{\mathcal{N}}$. The negative slope k is given next to each line. See main text for details.

Some discussion on our choice of parameter values is in order here. $N = 10$ and $\sigma/a = 2/\sqrt{3} \approx 1.15$ were used in the DPD simulations by Groot and Madden,[39,40] which are followed here. $N = 20$ is used (at $\sigma/a = 2/\sqrt{3}$ and 0.3) to examine the effects of chain discretization; larger N-values make the simulations more expensive to do. $\sigma/a = 0.3$ is chosen such that $\bar{\mathcal{N}}_{\rm cp} = 2 \times 10^4$ for $N = 10$, which is roughly the upper limit of $\bar{\mathcal{N}}$ in experiments as shown in Fig. 2.1, and the case of $\sigma/a = 0.1\sqrt{19} \approx 0.44$ and $N = 20$ is chosen because it has the same value of $\sigma/R_{e,0} = 0.1$ as the case of $\sigma/a = 0.3$ and $N = 10$. Clearly, $\bar{\mathcal{N}} > \bar{\mathcal{N}}_{\rm cp}$ cannot occur in experiments and is due to the use of soft potentials. On the one hand, setting $\bar{\mathcal{N}}_{\rm cp} = 2 \times 10^4$ in such models with $N < 100$ leads to $\sigma/a < 0.46$, which can be readily studied in simulations. On the other hand, simulation results for $\bar{\mathcal{N}} > \bar{\mathcal{N}}_{\rm cp}$ are interesting and equally useful for quantitative test of advanced fluctuation theories, which can then make experimentally relevant predictions. (Note that $\bar{\mathcal{N}} > \bar{\mathcal{N}}_{\rm cp}$ was also used in the DPD simulations by Groot and Madden.[39,40]) Similarly, while our N/κ-values in Fig. 2.11 do not correspond to typical values in experiments (i.e., our model system is much more

compressible), they greatly facilitate our sampling of configuration space. For the same reason, we do not perform simulations at $\chi N > 100$.

Denoting the k-value for $\bar{\mathcal{N}} < \bar{\mathcal{N}}_{\rm cp}$ by k_1 and that for $\bar{\mathcal{N}} > \bar{\mathcal{N}}_{\rm cp}$ by k_2, we first examine how $k_1 - k_2$ varies with N, σ, and N/κ. Fig. 2.11 shows that $k_1 - k_2$ decreases with increasing N (i.e., in the case of $\sigma/a = 0.3$), which leads to decreasing σ (thus weaker correlations) at constant $R_{e,0}$. One may therefore expect a single power-law decay of $\chi^*/\chi^*_{\rm MF} - 1$ with increasing $\bar{\mathcal{N}}$ in the limit of $N \to \infty$ (i.e., $\sigma \to 0$), which has no such correlations and is the case studied by Fredrickson and Helfand.[6] On the other hand, increasing σ/a at constant N leads to stronger correlations and thus increasing $k_1 - k_2$ (i.e., in the case of $N = 20$). We also note that varying N at constant σ/a exhibits both the correlation and chain discretization effects. To examine the latter alone, one may compare the case of $N = 10$ and $\sigma/a = 0.3$ with that of $N = 20$ and $\sigma/a = 0.1\sqrt{19}$ (both of which have $\sigma = 0.1R_{e,0}$). We expect that the chain discretization effects diminish quickly with increasing N, as supported by Fig. 6(a) of Ref. [26] showing $\chi^*_{\rm MF}N$ vs. N; more simulation data at larger N-values, however, are needed to check this. Finally, as N/κ increases from 0 to 50, $k_1 - k_2$ weakly increases (i.e., in the case of $N = 10$ and $\sigma/a = 0.3$) due to the increased segment repulsion (thus correlations).

The effects of N, σ, and N/κ on k_1 and k_2 themselves are more complicated and difficult to explain. We first note that, in the case of $\sigma/a = 2/\sqrt{3}$, $\bar{\mathcal{N}}_{\rm cp} < 15$ for both $N = 10$ and 20, and we do not perform simulations at $\bar{\mathcal{N}} < 100$ here (i.e., we only have k_2 in this case). This large σ/a-value also makes simulations at $\bar{\mathcal{N}} > 2000$ expensive to do. Nevertheless, from Fig. 2.11 we see that, while k_1 clearly decreases with increasing N, decreasing σ/a or decreasing N/κ, k_2 varies differently in different cases (i.e., the cases at $\sigma/a = 2/\sqrt{3}$ give different results from those at $\sigma/a = 0.3$ and $0.1\sqrt{19}$). The reason is not known at this point.

Finally, the qualitative trends of ODT shift (not the k-values) for $\bar{\mathcal{N}} \gtrsim 10^3$ shown in Fig. 2.11 can be explained based on the following argument in the context of the Reference Interaction Site Model (RISM) theory[54] for the disordered phase: As shown in detail in this paper,[55] RISM theory with the ideal DGC single-chain structure factor and RPA closure for soft

potentials[56] only accounts for the Gaussian-level fluctuations and gives $r_\psi^{\rm RPA} = 1-\chi/\chi^*_{\rm MF}$ for $\chi \le \chi^*_{\rm MF}$, where $r_\psi \equiv S_\psi(q^*, \chi N = 0)/S_\psi(q^*, \chi N)$ with $S_\psi(q, \chi N)$ being the structure factor due to the composition fluctuations and q^* the length of the wavevector at which $S_\psi(q, \chi N)$ reaches its maximum.[55] Non-Gaussian fluctuations are approximately accounted for by the Percus-Yevick (PY) closure[57] (also adapted for soft potentials), which can be reduced to RPA closure after the Taylor expansion $1 - \exp[\beta u_{s,s'}(r)] \approx -\beta u_{s,s'}(r)$, where $u_{s,s'}(r)$ denotes our non-bonded pair potential between segments s and s'. It is easy to show that the maximum value of $\beta u_{s,s'}(r)$, achieved at $r = 0$, linearly varies with $(N/\kappa)\bar{\mathcal{N}}^{-1/2}N^{-2}(\sigma/R_{e,0})^{-3}$ (or equivalently $(N/\kappa)\bar{\mathcal{N}}^{-1/2}N^{-1/2}(\sigma/a)^{-3}$). While at finite $\chi > 0$ r_ψ predicted by RISM theory with the ideal DGC single-chain structure factor and PY closure is always larger than $r_\psi^{\rm RPA}$ and never vanishes as shown in Ref. [55], the qualitative trends of ODT shift from $\chi^*_{\rm MF}$ can be inferred from the closeness of r_ψ to $r_\psi^{\rm RPA}$, which is controlled by the value of $\beta u_{s,s'}(r = 0)$. That is, $\chi^*/\chi^*_{\rm MF} - 1$ should decrease as N/κ decreases or other parameters ($\bar{\mathcal{N}}$, N, $\sigma/R_{e,0}$ or σ/a) increase. This is consistent with all of our simulation data at $\sigma/a = 0.3$ and $0.1\sqrt{19}$ (which are for $\bar{\mathcal{N}} \ge 10^3$), as well as the two data points at $\sigma/a = 2/\sqrt{3}$ and $\bar{\mathcal{N}} \approx 2 \times 10^3$, but not the rest at $\sigma/a = 2/\sqrt{3}$ and $\bar{\mathcal{N}} \le 10^3$.

2.4 Conclusions

To summarize, Fig. 2.1 shows that the invariant degree of polymerization $\bar{\mathcal{N}}$ controlling the system fluctuations is in the range of $500 \sim 20,000$ for nearly symmetric DBC melts commonly used in experiments.[10–15] Guided by this, we have performed FOMC simulations (the basic idea of which is to use soft potentials that allow particle overlapping)[26] with experimentally accessible fluctuations, and reported the first systematic study unambiguously quantifying the shift of ODT χ^* of symmetric DBC melts from the mean-field prediction $\chi^*_{\rm MF}$. Our simulations are performed in a canonical ensemble in order to avoid the fluctuations of $\bar{\mathcal{N}}$ (thus the segment interaction strength) during a simulation run; meanwhile, we

explain how to do FOMC simulations in a variable-density ensemble (e.g., an isothermal-isobaric or a grand-canonical ensemble). We use the very efficient pivot trial move, which can achieve very good acceptance rates in many-chain systems with soft potentials as shown in Sec. 2.2.3, and box-length change trial move, which eliminates the restriction of periodic boundary conditions on the lamellar period.[47] We further use the replica-exchange[48] of configurations at different χ-values to greatly reduce the sample correlation length, and the multiple histogram reweighting technique[37] with a novel order parameter characterizing the degree of positional order in lamellae to accurately locate ODT. These ensure that our simulations give the most accurate data of χ^* and bulk lamellar period reported to date.

Exactly the same model system (Hamiltonian) is used in both our simulations and mean-field theory; the ODT shift is therefore due to the fluctuations/correlations neglected by the latter. We have varied all the parameters in our model system ($\bar{\mathcal{N}}$, the number of segments N on each chain, the finite interaction range σ, and the compressibility N/κ of DBC melts) to examine their effects on the ODT shift. Our results are listed in Tables 2.2 and 2.4 and shown in Fig. 2.11. While $\chi^*/\chi^*_{\rm MF} - 1 \propto \bar{\mathcal{N}}^{-k}$ is found in all the cases, k decreases around $\bar{\mathcal{N}}_{\rm cp}$ (the $\bar{\mathcal{N}}$-value corresponding to the FCC close packing of polymer segments as hard spheres), indicating the short-range correlation effects. Such effects, as well as the k-value for $\bar{\mathcal{N}} < \bar{\mathcal{N}}_{\rm cp}$, decrease with increasing N, decreasing σ, or decreasing N/κ. In addition, the qualitative trends of ODT shift found in our simulations at $\bar{\mathcal{N}} \gtrsim 10^3$ (i.e., $\chi^*/\chi^*_{\rm MF} - 1$ decreases as N/κ decreases or other parameters ($\bar{\mathcal{N}}$, N and σ) increase) can be explained based on the segment repulsion strength in the context of the Reference Interaction Site Model (RISM) theory.[54] The opposite trends of N/κ, N and σ on the ODT shift, however, are found at smaller $\bar{\mathcal{N}}$ (where $\sigma/a = 2\sqrt{3}$ with a being the effective bond length used in our model). We hope our simulation results will stimulate the development of advanced theories that can quantitatively describe the fluctuation/correlation effects identified here.

Finally, by precisely controlling the mismatched lamellar period in simulations with fixed-length, cubic boxes, we have examined its effects on ODT. Our results shown in Fig. 2.10

clearly indicate that (1) a fixed-length box limits the system fluctuations, thus inducing periodic structures and decreasing ODT;[29] (2) the stretching/compression caused by a mismatched lamellar period makes the lamellae unstable, thus increasing ODT;[29] and (3) undulation, which occurs only when lamellae are stretched, reduces the frustration caused by a mismatched lamellar period and makes the lamellae stable.[53]

REFERENCES

[1] See, for example, F. S. Bates and G. H. Fredrickson, Annu. Rev. Phys. Chem. **41**, 525 (1990); *ibid.*, Phys. Today **52**, 32 (1999).

[2] G. H. Fredrickson, The Equilibrium Theory of Inhomogeneous Polymers, Oxford University Press, 2006.

[3] M. W. Matsen and M. Schick, Phys. Rev. Lett. **72**, 2660 (1994); C. A. Tyler and D. C. Morse, *ibid.* **94**, 208302 (2005).

[4] F. S. Bates, J. H. Rosedale, G. H. Fredrickson, and C. J. Glinka, Phys. Rev. Lett. **61**, 2229 (1988).

[5] F. S. Bates, M. F. Schulz, A. K. Khandpur, S. Forster, J. H. Rosedale, K. Almdal, and K. Mortensen, Faraday Discuss. **98**, 7 (1994).

[6] G. H. Fredrickson and E. Helfand, J. Chem. Phys. **87**, 697 (1987).

[7] V. E. Podneks and I. W. Hamley, JETP Lett. **64**, 617 (1996); I. W. Hamley and V. E. Podneks, Macromolecules **30**, 3701 (1997).

[8] S. A. Brazovskii, Sov. Phys. JETP **41**, 85 (1975).

[9] T. Ohta and K. Kawasaki, Macromolecules **19**, 2621 (1986).

[10] Y. Matsushita, K. Mori, R. Saguchi, Y. Nakao, I. Noda, and M. Nagasawa, Macromolecules **23**, 4313 (1990).

[11] T. Hashimoto, M. Shibayama, and H. Kawai, Macromolecules **13**, 1237 (1980).

[12] G. Hadziioannou and A. Skoulios, Macromolecules **15**, 258 (1982).

[13] C. M. Papadakis, K. Almdal, K. Mortensen, and D. Posselt, J. Phys. II France **7**, 1829 (1997).

[14] P. F. Green, T. M. Christensen, T. P. Russell, and R. Jerome, Macromolecules **22**, 2189 (1989).

[15] K. Almdal, J. H. Rosedale, F. S. Bates, G. D. Wignall, and G. H. Fredrickson, Phys. Rev. Lett. **65**, 1112 (1990).

[16] D. G. H. Ballard, G. D. Wignall, and J. Schelten, Eur. Polym. J. **9**, 965 (1973).

[17] J. Brandrup, E. H. Immergut, E. A. Grulke, A. Abe, and D. Bloch, Polymer Handbook, John Wiley & Sons Inc, 1999.

[18] L. J. Fetters, D. J. Lohse, D. Richter, T. A. Witten, and A. Zirkel, Macromolecules **27**, 4639 (1994).

[19] Y. Matsushita, K. Shimizu, Y. Nakao, H. Choshi, I. Noda, and M. Nagasawa, Polymer J. **18**, 361 (1986).

[20] H. L. Wagner and P. J. Flory, J. Am. Chem. Soc. **74**, 195 (1952).

[21] T. Hashimoto, N. Nakamura, M. Shibayama, A. Izumi, and H. Kawai, J. Macromol. Sci. Phys. **B17**, 389 (1980).

[22] M. Sikka, N. Singh, A. Karim, F. S. Bates, S. K. Satija, and C. F. Majkrzak, Phys. Rev. Lett. **70**, 307 (1993).

[23] See, for example, J.-L. Barrat and G. H. Fredrickson, J. Chem. Phys. **95**, 1281 (1991); A. M. Mayes and M. Olvera de la Cruz, J. Chem. Phys. **95**, 4670 (1991); A. V. Dobrynin and I. Ya. Erukhimovich, J. Phys. II **1**, 1387 (1991).

[24] A. Kudlay and S. Stepanow, J. Chem. Phys. **118**, 4272 (2003).

[25] H. S. Ashbaugh, H. A. Patel, S. K. Kumar, and S. Garde, J. Chem. Phys. **122**, 104908 (2005).

[26] Q. Wang and Y. Yin, J. Chem. Phys. **130**, 104903 (2009).

[27] Q. Wang, Soft Matter **5**, 4564 (2009); *ibid.* **6**, 6206 (2010).

[28] H. Fried and K. Binder, J. Chem. Phys. **94**, 8349 (1991); A. Weyersberg and T. A. Vilgis, Phys. Rev. E **48**, 377 (1993); R. G. Larson, Mol. Simul. **13**, 321 (1994); *ibid.*, Macromolecules **27**, 4198 (1994); Y. Yang, J. Lu, D. Yan, and J. Ding, Macromol. Theory Simul. **3**, 731 (1994); T. Dotera and A. Hatano, J. Chem. Phys. **105**, 8413 (1996); G. S. Grest, M. Lacasse, K. Kremer, and A. M. Gupta, J. Chem. Phys. **105**, 10583 (1996); A. Hoffmann, J. Sommer, and A. Blumen, J. Chem. Phys. **106**, 6709 (1997); *ibid.* **107**, 7559 (1997); T. Pakula, K. Karatasos, S. H. Anastasiadis, and G. Fytas, Macromolecules **30**, 8463 (1997); M. Murat, G. S. Grest, and K. Kremer, Macromolecules **32**, 595 (1999); A. J. Schultz, C. K. Hall, and J. Genzer, J. Chem. Phys. **117**, 10329 (2002); J. Yang, M. A. Winnik, and T. Pakula, Macromol. Theory Simul. **14**, 9 (2005); M. W. Matsen, G. H. Griffiths, R. A. Wickham, and O. N. Vassiliev, J. Chem. Phys. **124**, 024904 (2006).

[29] T. M. Beardsley and M. W. Matsen, Eur. Phys. J. E **32**, 255 (2010).

[30] O. N. Vassiliev and M. W. Matsen, J. Chem. Phys. **118**, 7700 (2003).

[31] F. A. Detcheverry, D. Q. Pike, P. F. Nealey, M. Muller, and J. J. de Pablo, Phys. Rev. Lett. **102**, 197801 (2009); D. Q. Pike, F. A. Detcheverry, M. Muller, and J. J. de Pablo, J. Chem. Phys. **131**, 084903 (2009).

[32] M. Muller and K. C. Daoulas, J. Chem. Phys. **128**, 024903 (2008).

[33] E. M. Lennon, K. Katsov, and G. H. Fredrickson, Phys. Rev. Lett. **101**, 138302 (2008).

[34] Their result of $\chi^*_{\rm MF}N = 10.3$ is incorrect and should be 10.481 instead, which is used in Fig. 2.2. Due to the lack of data, their $\bar{\mathcal{N}}$-values are directly used in Fig. 2.2.

[35] K. C. Daoulas and M. Muller, J. Chem. Phys. **125**, 184904 (2006).

[36] L. Leibler, Macromolecules **13**, 1602 (1980).

[37] A. M. Ferrenberg and R. H. Swendsen, Phys. Rev. Lett. **63**, 1195 (1989).

[38] Q. Wang, J. Chem. Phys. **129**, 054904 (2008).

[39] R. D. Groot and T. J. Madden, J. Chem. Phys. **108**, 8713 (1998).

[40] P. Sandhu, J. Zong, D. Yang, and Q. Wang, J. Chem. Phys. **138**, 194904 (2013).

[41] E. Helfand and Y. Tagami, J. Polym. Sci., Part B: Polym. Lett. **9**, 741 (1971).

[42] P. J. Hoogerbrugge and J. M. V. A. Koelman, Europhys. Lett. **19**, 155 (1992).

[43] C. N. Likos, A. Lang, M. Watzlawek, and H. Lowen, Phys. Rev. E **63**, 031206 (2001).

[44] S. D. Stellman and P. J. Gans, Macromolecules **5**, 516 (1972).

[45] F. J. Vesely, J. Comput. Phys. **1982**, **47**, 291 (1982).

[46] O. F. Olaj, B. Neubauer, and G. Zifferer, Macromol. Theory Simul. **7**, 381 (1998).

[47] Q. Wang, Q, Yan, P. F. Nealey, and J. J. de Pablo, J. Chem. Phys. **112**, 450 (2000).

[48] R. H. Swendsen and J. Wang, Phys. Rev. Lett. **57**, 2607 (1986).

[49] N. Madras and A. D. Sokal, J. Stat. Phys. **50**, 109 (1988).

[50] J. D. Chodera, W. C. Swope, J. W. Pitera, C. Seok, and K. A. Dill, J. Chem. Theory Comput. **3**, 26 (2007).

[51] M. Muller and N. B. Wilding, Phys. Rev. E **51**, 2079 (1995).

[52] J. Zong, X. Zhang, and Q. Wang, J. Chem. Phys. **137**, 134904 (2012).

[53] H. Guo and K. Kremer, J. Chem. Phys. **118**, 7714 (2003).

[54] D. Chandler and H. C. Andersen, J. Chem. Phys. **57**, 1930 (1972).

[55] D. Yang, J. Zong, and Q. Wang, Macromolecules, to be submitted.

[56] A. Lang, C. N. Likos, M. Watzlawek, and H. Lowen, J. Phys.: Condens. Matter **12**, 5087 (2000); A. A. Louis, P. G. Bolhuis, and J. P. Hansen, Phys. Rev. E. **62**, 7961 (2000).

[57] J. K. Percus and G. J. Yevick, Phys. Rev. **110**, 1 (1958).

CHAPTER 3

DISENTANGLE MODEL DIFFERENCES AND FLUCTUATION EFFECTS OF DIBLOCK COPOLYMERS

3.1 Introduction

Dissipative particle dynamics (DPD) is a coarse-grained dynamic simulation technique, which has been widely used since proposed by Hoogerbrugge and Koelman about 20 years ago.[1] In this method, the total force acting on particle i consists of three parts: $\mathbf{F}_i = \sum_{j \neq i} \left(\mathbf{F}_{ij}^C + \mathbf{F}_{ij}^D + \mathbf{F}_{ij}^R \right)$, where $\beta\sigma\mathbf{F}_{ij}^C = a_{ij}(1 - r_{ij}/\sigma)\hat{\mathbf{r}}_{ij}$ for $r_{ij} < \sigma$ and 0 otherwise is the conservative force applied by particle j on i, with $\beta \equiv 1/k_B T$, k_B being the Boltzmann constant, T the thermodynamic temperature, σ the cut-off radius, $a_{ij} \geq 0$ a dimensionless number controlling the interaction strength, $r_{ij} \equiv |\mathbf{r}_{ij}|$, $\mathbf{r}_{ij} \equiv \mathbf{r}_i - \mathbf{r}_j$, $\mathbf{r}_i$ denoting the spatial position of particle i, and $\hat{\mathbf{r}}_{ij} \equiv \mathbf{r}_{ij}/r_{ij}$; $\beta\sigma\mathbf{F}_{ij}^D = -\gamma\omega^D(r_{ij}) \left[\hat{\mathbf{r}}_{ij} \cdot \sqrt{\beta m}(\mathbf{v}_i - \mathbf{v}_j) \right] \hat{\mathbf{r}}_{ij}$ is the dissipative (or drag) force, with $\gamma \geq 0$ being a dimensionless number controlling its strength, $\omega^D(r_{ij}) \geq 0$ a dimensionless weight function, m the particle mass (assumed to be the same for all particles), and $\mathbf{v}_i$ the velocity of particle i; and $\beta\sigma\mathbf{F}_{ij}^R = \alpha\omega^R(r_{ij})\xi_{ij}\hat{\mathbf{r}}_{ij}$ is the random force, with $\alpha \geq 0$ being a dimensionless number controlling its strength, $\omega^R(r_{ij}) \geq 0$ a dimensionless weight function, and ξ_{ij} a random number with zero mean and unit variance. One attractive feature of DPD simulation is that it conserves the momentum and thus gives the correct long-term hydrodynamic behavior of the system.[1]

In this work, however, we focus on the thermodynamic behavior. Espanol and Warren showed that, if $\alpha\omega^R(r_{ij}) = \sqrt{2\gamma\omega^D(r_{ij})}$, the Hamiltonian (or potential) for the conservative force $\beta\mathcal{H}^C$ then completely determines the system thermodynamics,[2] which means that such

DPD simulations can in principle (1) sample the full spectrum of fluctuations/correlations of the system, and (2) give the same thermodynamic properties as Monte Carlo simulations using $\beta\mathcal{H}^C$; the latter idea was indeed explored by Smit and co-workers.[3,4] We note that, as another attractive feature of DPD simulation, its $\beta\mathcal{H}^C$ is soft (i.e., allows complete particle overlapping). Using soft potentials is the basic idea of the so-called fast Monte Carlo (FMC) simulations,[5,6] which have recently attracted great interest especially in the study of polymeric systems.[7–12]

In particular, Groot and Madden first performed DPD simulations to study the microphase separation of linear diblock copolymer (DBC) A-B melts, and compared their results with those from the self-consistent field (SCF) calculations of Matsen and Bates;[13] after taking into account the fluctuation effects based on the theory of Fredrickson and Helfand (FH),[14] they found "quantitative match for the locations of the phase transitions".[15,16] Similar work was done by Chen et al.,[17] whose DPD results are consistent with and complementary to those of Groot and Madden.[15,16] There are, however, several important differences between the DPD and SCF studies: First, the DPD simulations use a compressible system of discrete Gaussian chains each of $N = 10$ segments interacting with a finite-range (DPD) potential, while the SCF calculations use the "standard" model, i.e., an incompressible system of continuous Gaussian chains interacting with the Dirac δ-function potential. The system compressibility, chain discretization, and interaction range can all change the phase boundaries quantitatively.

Second, SCF theory is a mean-field theory neglecting the system fluctuations/correlations. While such effects were taken into account by Groot and Madden based on FH theory, this theory is based on the Hartree analysis by Brazovskii[18] and the Ohta-Kawasaki effective Hamiltonian[19] for the "standard" model. The Hartree analysis is rigorously accurate only for the invariant degree of polymerization $\bar{\mathcal{N}} \equiv (nR_{e,0}^3/V)^2 \gtrsim 10^{10}$,[14] where n denotes the number of chains in volume V and $R_{e,0}$ the root-mean-square end-to-end distance of an ideal chain. As shown in Sec. 3.2.1, however, $\bar{\mathcal{N}} \approx 28$ and 77 in the DPD

simulations, which do not justify the use of FH theory. Furthermore, the fitting of a_{ij} to the Flory-Huggins χ parameter characterizing the A-B repulsion in the "standard" model used by Groot and Madden[15,16] is not rigorous, as explained in detail in Sec. 3.3.1.1.

Third, DPD is a dynamic simulation technique while SCF is an equilibrium approach, which means that the structures in DPD simulations could be kinetically trapped. Indeed, no well-ordered, spatially periodic structure was found in several cases of the DPD simulations,[15–17] as discussed in detail in Sec. 3.3.3.

Fourth, a fixed-size box of $(20\sigma)^3$ with the periodic boundary conditions applied in all directions was used in the DPD simulations, which limits the allowed periods of the ordered structures,[20] while the SCF calculations minimize the system free energy by finding the bulk period of each ordered structure. Last but not least, Groot and Madden used binary blends of DBC with different compositions (volume fractions of the A-block in the copolymer) f to sample intermediate f-values that are not integer multiples of 0.1,[15,16] while the SCF calculations are for pure DBC systems. Comparisons between the DPD simulations and the SCF calculations of the "standard" model mix all these differences together; the meaning of "quantitative match" between the two is therefore not clear.

In this work, we perform both SCF calculations and fast off-lattice monte carlo[5] (FOMC) simulations in a canonical ensemble based on exactly the same model DBC system as used in the DPD simulations (i.e., $\beta\mathcal{H}^C$ including the bonding potential).[15,17] In particular, in addition to the cubic box of $(20\sigma)^3$, our FOMC simulations are also performed in variable-length boxes to find the bulk period of lamellar and cylindrical structures. Comparing our SCF results with those for the "standard" model therefore unambiguously reveals the effects of model differences (i.e., the system compressibility, chain discretization, and interaction range), and comparing our SCF and FOMC results reveals, without any parameter-fitting, the effects of system fluctuations/correlations neglected in the SCF theory. Furthermore, comparing our fixed-box FOMC results with the DPD results unambiguously identifies the kinetically trapped structures in the latter, and comparing our SCF (or FOMC) results

in fixed- and variable-length boxes can unambiguously reveal the effects of fixed vs. bulk periods. For simplicity, we only consider systems of pure DBC in this work.

3.2 Model and Methods

3.2.1 Model system used in DPD simulations of DBC

The model system used in Ref. [15] consists of n DBC chains, each having $N_{\rm A}$ segments of type A followed by $N_{\rm B}$ segments of B. The volume fraction of the A block in the copolymer is denoted by $f \equiv N_{\rm A}/N$ with $N \equiv N_{\rm A}+N_{\rm B} = 10$ used in Ref. [15]. The discrete Gaussian chain (DGC) model is used for the chain connectivity; that is, adjacent segments on a chain are connected by Gaussian springs with the bonding potential $\beta u^b_{k,s} = (3/2a^2)\left(\mathbf{R}_{k,s+1} - \mathbf{R}_{k,s}\right)^2$, where $\beta \equiv 1/k_BT$ with k_B being the Boltzmann constant and T the thermodynamic temperature, a denotes the effective bond length, and $\mathbf{R}_{k,s}$ the spatial position of the $s^{\rm th}$ segment on the $k^{\rm th}$ chain. Comparing the above with the spring force

$$\beta\sigma\mathbf{F}^S_{ij} = -4\mathbf{r}_{ij}/\sigma \tag{3.1}$$

between two connected segments i and j used in Ref. [15], where σ denotes the cut-off radius (set to 1 in Ref. [15]), $\mathbf{F}^S_{ij}$ is the force acting by segment j on i, and $\mathbf{r}_{ij} \equiv \mathbf{r}_i - \mathbf{r}_j$ with $\mathbf{r}_i$ being the spatial position of segment i, we find that $\sigma/a = 2/\sqrt{3}$ (i.e., $R_{e,0} \equiv \sqrt{N-1}a = 3\sqrt{3}\sigma/2$) is used in Ref. [15].

As for the non-bonded interactions, all segments (regardless of their type) interact with the pair potential $u^\kappa(r) = u_0(r)/\kappa\rho_0$, where r denotes the distance between two segments, $\beta u_0(r) = (15/2\pi\sigma^3)(1-r/\sigma)^2$ for $r < \sigma$ and 0 otherwise (note that the coefficient here is chosen such that the DPD potential $\beta u_0(r)$ is normalized in 3D, i.e., $\int {\rm d}\mathbf{r}\beta u_0(r) = 1$; in the limit of $\sigma \to 0$, $\beta u_0(r)$ then becomes the Dirac δ-function potential $\delta(r)$), the average segmental number density $\rho_0 \equiv nN/V$ with V being the system volume, and the generalized Helfand compressibility[21,22] $\kappa \geq 0$ controls the interaction strength ($\kappa = 0$ corresponds to the hard-sphere chains). In addition, an A segment interacts with a B segment via the pair potential $u^\chi(r) = u_0(r)\chi/\rho_0$ with the generalized Flory-Huggins parameter $\chi \geq 0$ controlling

the A-B repulsion strength. Comparing these with the conservative force given by Eq. (2) of Ref. [15] (also in the Introduction of Chapter 3), we find that the maximum repulsion parameters used in Ref. [15] are given by $a_{\rm AA} = a_{\rm BB} = 15/\pi\rho_0\sigma^3\kappa$ and $a_{\rm AB} = (15/\pi\rho_0\sigma^3)(1/\kappa+\chi)$. Their value of $a_{\rm AA} = a_{\rm BB} = 75/\rho_0\sigma^3$ therefore corresponds to $N/\kappa = 50\pi$. In addition, the two segmental number densities, $\rho_0\sigma^3 = 3$ and 5, used in Ref. [15] correspond to the invariant degree of polymerization $\bar{\mathcal{N}} \equiv (nR_{e,0}^3/V)^2 \approx 28$ and 77, respectively; and their value of $a_{\rm AB} = 40$ used at $\rho_0\sigma^3 = 3$ corresponds to $\chi N = 30\pi$, and $a_{\rm AB} = 21$ used at $\rho_0\sigma^3 = 5$ corresponds to $\chi N = 20\pi$.

The canonical-ensemble configuration integral of the system is

$$\mathcal{Z} = \prod_{k=1}^{n}\prod_{s=1}^{N}\sum_{\mathbf{R}_{k,s}} \cdot \exp\left\{-\sum_{k=1}^{n}\sum_{s=1}^{N-1}\beta u_{k,s}^{b} - \beta\mathcal{H}^{nb}[\hat{\rho}_{\rm A},\hat{\rho}_{\rm B}]\right\} \tag{3.2}$$

with the Hamiltonian due to the non-bonded interactions given by

$$\begin{aligned}\mathcal{H}^{nb} = &\frac{1}{2\kappa\rho_0}\int {\rm d}\mathbf{r}{\rm d}\mathbf{r}'\,[\hat{\rho}_{\rm A}(\mathbf{r})+\hat{\rho}_{\rm B}(\mathbf{r})]\,u_0(|\mathbf{r}-\mathbf{r}'|)\,[\hat{\rho}_{\rm A}(\mathbf{r}')+\hat{\rho}_{\rm B}(\mathbf{r}')] - \frac{nN}{2\kappa\rho_0}u_0(0)\\ &+\frac{\chi}{\rho_0}\int {\rm d}\mathbf{r}{\rm d}\mathbf{r}'\hat{\rho}_{\rm A}(\mathbf{r})u_0(|\mathbf{r}-\mathbf{r}'|)\hat{\rho}_{\rm B}(\mathbf{r}'),\end{aligned} \tag{3.3}$$

where the microscopic number densities of A and B segments at spatial position $\mathbf{r}$ are defined as $\hat{\rho}_{\rm A}(\mathbf{r}) \equiv \sum_{k=1}^{n}\sum_{s=1}^{N_{\rm A}}\delta(\mathbf{r}-\mathbf{R}_{k,s})$ and $\hat{\rho}_{\rm B}(\mathbf{r}) \equiv \sum_{k=1}^{n}\sum_{s=N_{\rm A}+1}^{N}\delta(\mathbf{r}-\mathbf{R}_{k,s})$, respectively. It is easy to show that Eq. (3.3) is simply the summation of $u^{\kappa}(r)$ and $u^{\chi}(r)$ over all segment pairs in the system. We note that Eq. (3.3) is equivalent to Eq. (A4) in Ref. [5].

3.2.2 Fast off-lattice Monte Carlo (FOMC) simulations

We perform FOMC simulations of the above model system in a canonical ensemble with trial moves of hopping,[5] reptation,[5] pivot,[23] and box-length change (when a rectangular parallelepipedal simulation box with variable lengths is used).

In simulations of periodic structures, the periodic boundary conditions limit the allowed orientations of the structure and thus its period. For example, for lamellae with a normal direction $\mathbf{n}$ in a simulation box with length L_j in the $\mathbf{j}(=\mathbf{x},\mathbf{y},\mathbf{z})$ direction, $L_j\mathbf{j}\cdot\mathbf{n} = n_jL(\mathbf{n})$ must be satisfied, where n_j is the number of periods contained in the box along the $\mathbf{j}$ direction

(which could be 0) and L the lamellar period; this gives $L(\mathbf{n}) = 1\Big/\sqrt{\sum_{\mathbf{j}} (n_j/L_j)^2}$.[20] For a fixed-length box as commonly used in canonical-ensemble simulations, both the lamellar orientation and its period are therefore discretized (i.e., L can hardly be the bulk period L_0).[20] To eliminate this problem for lamellar structures, we use box-length change trial moves to generate, without loss of generality, the new box length along the x direction as $L_{x,\text{new}} = L_{x,\text{old}} \exp(\xi)$, where $L_{x,\text{old}}$ is the box length before the trial move and ξ a random number uniformly distributed within $(-\xi_{\max}, \xi_{\max})$, and set the box lengths along the other two directions to be the same (i.e., $L_y = L_z$), which are varied accordingly to keep V constant. The spatial positions of all segments are then re-scaled in each direction.[23] For 2D hexagonally packed cylindrical structures, where the restriction of a fixed-length box is more severe,[24] we use similar trial moves except keeping $L_y = \sqrt{3} L_z$. We have not performed FOMC simulations of 3D periodic structures, where canonical-ensemble simulations cannot be used to find L_0 without accurate free-energy calculations.[25]

Finally, to determine the order-disorder transition (ODT) of symmetric DBC, we use replica-exchange[26] at different χN (with acceptance rates of 40$\sim$90%) to further improve our sampling, a new order parameter characterizing the degree of positional order in lamellae, and multiple histogram reweighting[27] to accurately locate ODT according to the equal-weight criterion.[28] To estimate the statistical error of ODT, we calculate ODT using the first- and second-half of our samples collected after equilibration, respectively, and take three times their largest deviation from ODT determined using all the samples as the error bar.[23] More details are given in Chapter 2.

3.2.3 Self-consistent field (SCF) calculations

To transform the particle-based model in Sec. 3.2.1 to a field-based one, we insert in Eq. (3.2) the following identity

$$1 = \prod_{j=\text{A,B}} \int \mathscr{D}\phi_j \mathscr{D}\omega_j \exp\left\{ \int \mathrm{d}\mathbf{r} \omega_j(\mathbf{r}) \left[\rho_0 \phi_j(\mathbf{r}) - \hat{\rho}_j(\mathbf{r}) \right] \right\},$$

where $\phi_{\rm A}(\mathbf{r})$ and $\phi_{\rm B}(\mathbf{r})$ are the normalized segmental density (volume fraction) fields constrained to $\hat{\rho}_{\rm A}(\mathbf{r})/\rho_0$ and $\hat{\rho}_{\rm B}(\mathbf{r})/\rho_0$, respectively, and $\omega_{\rm A}(\mathbf{r})$ and $\omega_{\rm B}(\mathbf{r})$ are the conjugate fields interacting with A and B segments, respectively, which impose the constraints. We further re-scale variables according to $\mathbf{r}/R_{e,0} \to \mathbf{r}$ (thus $V/R_{e,0}^d \to V$, where d is the number of dimensions in which calculations are performed), $u_0(r)R_{e,0}^d \to u_0(r)$, and $N\omega_j(\mathbf{r}) \to \omega_j(\mathbf{r})$ (j=A,B), and finally obtain

$$\mathcal{Z} = \int \mathscr{D}\phi_{\rm A}\mathscr{D}\omega_{\rm A}\mathscr{D}\phi_{\rm B}\mathscr{D}\omega_{\rm B}\exp\{-n\beta f_c[\phi_{\rm A},\phi_{\rm B},\omega_{\rm A},\omega_{\rm B}]\}$$

with

$$\begin{aligned}\beta f_c =& \frac{\chi N}{V}\int {\rm d}\mathbf{r}{\rm d}\mathbf{r}'\phi_{\rm A}(\mathbf{r})\beta u_0(|\mathbf{r}-\mathbf{r}'|)\phi_{\rm B}(\mathbf{r}') \\ &+\frac{N}{2\kappa V}\int {\rm d}\mathbf{r}{\rm d}\mathbf{r}'\left[\phi_{\rm A}(\mathbf{r})+\phi_{\rm B}(\mathbf{r})\right]\beta u_0(|\mathbf{r}-\mathbf{r}'|)\left[\phi_{\rm A}(\mathbf{r}')+\phi_{\rm B}(\mathbf{r}')\right] \\ &-\frac{1}{V}\int {\rm d}\mathbf{r}\left[\omega_{\rm A}(\mathbf{r})\phi_{\rm A}(\mathbf{r})+\omega_{\rm B}(\mathbf{r})\phi_{\rm B}(\mathbf{r})\right]-\ln Q[\omega_{\rm A},\omega_{\rm B}], \end{aligned} \tag{3.4}$$

where an unimportant constant factor is omitted in $\mathcal{Z}$, and the single-chain partition function is defined as $Q \equiv \prod_{s=1}^{N}\sum_{\mathbf{R}_s}\cdot\exp\left[-\sum_{s=1}^{N-1}\beta u_s^b-\sum_{s=1}^{N_{\rm A}}\omega_{\rm A}(\mathbf{R}_s)/N-\sum_{s=N_{\rm A}+1}^{N}\omega_{\rm B}(\mathbf{R}_s)/N\right]\Big/G$ with $G \equiv \prod_{s=1}^{N}\sum_{\mathbf{R}_s}\cdot\exp\left(-\sum_{s=1}^{N-1}\beta u_s^b\right) = V\left[4\pi\sqrt{\pi/6}/3(N-1)^{3/2}\right]^{N-1}$. This field theory is the starting point for analysis using the random-phase approximation (RPA),[29] which closely follows the Appendices 3 and 4 of Ref. [5] and gives the mean-field ODT of symmetric DBC, and derivation of the SCF equations given below.

The SCF equations are obtained from Eq. (3.4) under the mean-field approximation, which neglects the system fluctuations/correlations and is exact in the limit of $\bar{\mathcal{N}} \to \infty$ (at finite $R_{e,0}$). That is, by setting $\delta\beta f_c/\delta\phi_j(\mathbf{r}) = \delta\beta f_c/\delta\omega_j(\mathbf{r}) = 0$ we obtain

$$\hat{\omega}_{\rm A}(\mathbf{k}) = \beta\hat{u}_0(k)\left[\frac{N}{\kappa}\hat{\phi}_{\rm A}(\mathbf{k})+\left(\frac{N}{\kappa}+\chi N\right)\hat{\phi}_{\rm B}(\mathbf{k})\right] \tag{3.5}$$

$$\hat{\omega}_{\rm B}(\mathbf{k}) = \beta\hat{u}_0(k)\left[\frac{N}{\kappa}\hat{\phi}_{\rm B}(\mathbf{k})+\left(\frac{N}{\kappa}+\chi N\right)\hat{\phi}_{\rm A}(\mathbf{k})\right] \tag{3.6}$$

$$\phi_{\rm A}(\mathbf{r}) = \frac{\exp[\omega_{\rm A}(\mathbf{r})/N]}{N\hat{q}_N(\mathbf{k}=\mathbf{0})/V} \sum_{s=1}^{N_{\rm A}} q_s(\mathbf{r}) q^*_{N-s+1}(\mathbf{r}) \tag{3.7}$$

$$\phi_{\rm B}(\mathbf{r}) = \frac{\exp[\omega_{\rm B}(\mathbf{r})/N]}{N\hat{q}_N(\mathbf{k}=\mathbf{0})/V} \sum_{s=N_{\rm A}+1}^{N} q_s(\mathbf{r}) q^*_{N-s+1}(\mathbf{r}), \tag{3.8}$$

where we denote the Fourier transform of $\omega_j(\mathbf{r})$, for example, by $\hat{\omega}_j(\mathbf{k}) \equiv \int {\rm d}\mathbf{r} e^{-i\mathbf{k}\cdot\mathbf{r}} \omega_j(\mathbf{r})$ with $\mathbf{k}$ being the wave-vector, and $k \equiv |\mathbf{k}|$. The chain propagator $q_s(\mathbf{r})$ corresponds to the probability of finding a partial copolymer chain of s segments that starts from the A-end (where $s = 1$) anywhere in the system and ends at $\mathbf{r}$, and satisfies the Chapman-Kolmogorov equation (CKE)[22]

$$q_{s+1}(\mathbf{r}) = \begin{cases} \exp[-\omega_{\rm A}(\mathbf{r})/N] \int {\rm d}\mathbf{r}' \Phi(|\mathbf{r}-\mathbf{r}'|) q_s(\mathbf{r}') & \text{for } s = 1, \ldots, N_{\rm A}-1 \\ \exp[-\omega_{\rm B}(\mathbf{r})/N] \int {\rm d}\mathbf{r}' \Phi(|\mathbf{r}-\mathbf{r}'|) q_s(\mathbf{r}') & \text{for } s = N_{\rm A}, \ldots, N-1 \end{cases} \tag{3.9}$$

with the initial condition $q_1(\mathbf{r}) = \exp[-\omega_{\rm A}(\mathbf{r})/N]$, where $\Phi(r) = [3(N-1)/2\pi]^{3/2} \exp\left[-3(N-1)r^2/2\right]$. Similarly, the propagator $q^*_t(\mathbf{r})$ corresponds to the probability of finding a partial copolymer chain of t segments that starts from the B-end (where $t \equiv N - s + 1 = 1$) anywhere in the system and ends at $\mathbf{r}$, and satisfies the following CKE

$$q^*_{t+1}(\mathbf{r}) = \begin{cases} \exp[-\omega_{\rm B}(\mathbf{r})/N] \int {\rm d}\mathbf{r}' \Phi(|\mathbf{r}-\mathbf{r}'|) q^*_t(\mathbf{r}') & \text{for } t = 1, \ldots, N_{\rm B}-1 \\ \exp[-\omega_{\rm A}(\mathbf{r})/N] \int {\rm d}\mathbf{r}' \Phi(|\mathbf{r}-\mathbf{r}'|) q^*_t(\mathbf{r}') & \text{for } t = N_{\rm B}, \ldots, N-1 \end{cases} \tag{3.10}$$

with the initial condition $q^*_1(\mathbf{r}) = \exp[-\omega_{\rm B}(\mathbf{r})/N]$. Once the SCF equations are solved, the mean-field free energy per chain can be calculated as

$$\begin{aligned} \beta f_c = -\frac{1}{V} \int \frac{{\rm d}\mathbf{k}}{(2\pi)^3} \Big\{ \frac{N}{2\kappa} \left[\hat{\phi}_{\rm A}(\mathbf{k}) + \hat{\phi}_{\rm B}(\mathbf{k})\right] \beta\hat{u}_0(k) \left[\hat{\phi}_{\rm A}(-\mathbf{k}) + \hat{\phi}_{\rm B}(-\mathbf{k})\right] \\ + \chi N \hat{\phi}_{\rm A}(\mathbf{k}) \beta\hat{u}_0(k) \hat{\phi}_{\rm B}(-\mathbf{k}) \Big\} - \ln \frac{\hat{q}_N(\mathbf{k}=\mathbf{0})}{V}. \end{aligned} \tag{3.11}$$

We solve the SCF equations in real space with the periodic boundary conditions applied in all directions. For given $\{\omega_{\rm A}(\mathbf{r}), \omega_{\rm B}(\mathbf{r})\}$ at all $\mathbf{r}$, the convolutions in Eqs. (3.9) and (3.10) are evaluated via the fast Fourier transforms;[30] $\{\phi_{\rm A}(\mathbf{r}), \phi_{\rm B}(\mathbf{r})\}$ at all $\mathbf{r}$ are then calculated

via Eqs. (3.7) and (3.8); finally, Eqs. (3.5) and (3.6) are solved via either the Broyden method combined with a globally convergent strategy[31] in 1D or the Anderson mixing[32] in 2D and 3D, with their maximum residual error at all $\mathbf{r}$ less than 10^{-12}. Once the SCF equations are solved, the integral in Eq. (3.11) is evaluated via the Romberg integration.[33] Our spatial discretization gives an accuracy of at least 10^{-5} in the calculated βf_c. We have only considered four ordered morphologies in this work: lamellae (L) in 1D, hexagonally packed cylinders (C) in 2D, and spheres arranged on a body-centered cubic lattice (S) and the double-gyroid (G) in 3D. Unless specified otherwise, for each of these morphologies we minimize βf_c with respect to the calculation cell size to obtain its bulk period L_0 at given χN. These minimized βf_c, along with that of the disordered phase (D), are then used to determine the phase boundaries at given f.

Finally, in the limit of $N \to \infty$ at finite $R_{e,0}$, DGC becomes the continuous Gaussian chain (CGC) model commonly used in polymer field theories. In addition, with $\sigma = 0$ and $\kappa = 0$, our model recovers the "standard" one (i.e., incompressible DBC melts of CGC interacting with the Dirac δ-function potential) used in polymer field theories, for which the SCF equations can be found in, for example, Ref. [34]. In view of this correspondence between our model and the "standard" one, their χN can be directly compared.

3.3 Results and Discussion

For the DPD model system, unless specified otherwise, we use the same parameter values as in the DPD simulations,[15,17] i.e., $N = 10$, $\sigma/R_{e,0} = 2/3\sqrt{3}$, $N/\kappa = 50\pi$, $\chi N = 30\pi$ (at $\rho_0\sigma^3 = 3$) and 20π (at $\rho_0\sigma^3 = 5$).

3.3.1 Symmetric DBC

3.3.1.1 Order-disorder transition (ODT)

Table 3.1 shows the mean-field ODT $\chi^*_{\rm MF}N$ and the corresponding bulk lamellar period $L^*_{0,\rm MF}$ determined from RPA, which are not affected by the system compressibility N/κ[34] and the invariant degree of polymerization $\bar{\mathcal{N}}$. We see that $\chi^*_{\rm MF}N$ increases with both

increasing interaction range σ and increasing chain discretization N, and $L^*_{0,\mathrm{MF}}$ increases with increasing σ but decreasing N. These are consistent with and well understood based on Refs. [5,34] (note that $L^*_{0,\mathrm{MF}}$ in Fig. 6(b) of Ref. [5] is in units of $\sqrt{N/6}a$ instead of $R_{e,0}$). On the other hand, Table 3.2 shows the ODT χ^*N and the corresponding bulk lamellar period L^*_0 determined from our FOMC simulations of the DPD model system. We see that both χ^*N and L^*_0 are significantly larger than the corresponding mean-field value due to the large system fluctuations/correlations, which are expected for the small $\bar{\mathcal{N}}$-values used in the simulations. Another well-known effect of fluctuations on ODT of symmetric DBC is to change it from a second-order phase transition predicted by the mean-field theory to a first-order transition.[14,23]

Table 3.1: Mean-field ODT $\chi^*_{\mathrm{MF}}N$ and the corresponding bulk lamellar period $L^*_{0,\mathrm{MF}}$ (shown in parentheses) of symmetric DBC for four combinations of chain model with non-bonded interaction potential, obtained from RPA. The upper-left corresponds to the "standard" model and the lower-right to the DPD model system.

$\chi^*_{\mathrm{MF}}N(L^*_{0,\mathrm{MF}}/R_{e,0})$	δ-function potential	DPD-potential
CGC	10.495 (1.318)	12.134 (1.462)
DGC with $N = 10$	9.944 (1.345)	11.427 (1.495)

To compare their DPD simulations with the SCF results for the "standard" model, Groot and Madden mapped the interaction parameters $a_{\mathrm{AA}} = a_{\mathrm{BB}}$ and a_{AB} in the simulations to the Flory-Huggins χ parameter in the "standard" model (denoted by χ_e hereafter) using the following relation:

$$\chi_e = \begin{cases} (0.306 \pm 0.003)(a_{\mathrm{AB}} - a_{\mathrm{AA}}) & \text{for } \rho_0\sigma^3 = 3 \text{ and } 2 < N < 10 \\ (0.689 \pm 0.002)(a_{\mathrm{AB}} - a_{\mathrm{AA}}) & \text{for } \rho_0\sigma^3 = 5 \text{ and } N = 1 \end{cases} . \tag{3.12}$$

This relation is for $\chi_e > 3$ and obtained by Groot and Warren via fitting the domain segregation from canonical-ensemble DPD simulations of phase-separated symmetric mixtures of A and B monomers (at $\rho_0\sigma^3 = 5$) and homopolymers (at $\rho_0\sigma^3 = 3$, where a value of 2 instead

Table 3.2: ODT χ^*N and the corresponding bulk lamellar period L_0^* of symmetric DBC for the DPD model at given segmental number density $\rho_0\sigma^3$, obtained from FOMC simulations. The corresponding values of the invariant degree of polymerization $\bar{\mathcal{N}}$, the Flory-Huggins parameter χ_e, and that corrected for the fluctuation effects based on FH theory $\chi_{e,f}$ are also listed. See main text for more details. [a] According to Sec. 3.2.1 and Eq. (3.12), we have $\chi_e^*N = (15/\pi\rho_0\sigma^3)\lambda\chi^*N$ and calculate its error $\epsilon_{\chi_e^*N} = \chi_e^*N\sqrt{(\epsilon_{\chi^*N}/\chi^*N)^2 + (\epsilon_\lambda/\lambda)^2}$.

$\rho_0\sigma^3$	$\bar{\mathcal{N}}$	χ^*N	$\chi_e^*N^a$	$\chi_{e,f}^*N$	$L_0^*/R_{e,0}$
3	≈ 28	55.08 ± 0.47	26.82 ± 0.82	11.70 ± 0.36	2.203 ± 0.001
5	≈ 77	34.31 ± 0.82	22.57 ± 0.57	11.76 ± 0.30	2.053 ± 0.003

of 4 was used in the spring force given in Eq. (3.1)) to the corresponding prediction of the Flory-Huggins theory,[35] and its use by Groot and Madden clearly has no rigorous basis.

To account for the fluctuation effects neglected by the SCF calculations, Groot and Madden further used an "effective" χ-parameter $\chi_{e,f} = \chi_e/(1 + 3.91\bar{\mathcal{N}}^{-1/3})$ based on FH theory,[14] which gives $\chi^*/\chi^*_{\rm MF} - 1 = 3.91\bar{\mathcal{N}}^{-1/3}$. The values of χ_e^*N and $\chi_{e,f}^*N$ corresponding to χ^*N determined from our FOMC simulations are also listed in Table 3.2; at both densities, $\chi_{e,f}^*N$ is clearly different from the mean-field ODT for the "standard" model (i.e., 10.495). As explained in Chapter 2, the small $\bar{\mathcal{N}}$-values in the DPD simulations do not justify the use of FH theory; indeed, our FOMC data in Table 3.2 give $\chi^*/\chi^*_{\rm MF} - 1 = 31.16\bar{\mathcal{N}}^{-0.63}$ if the power-law is assumed. Finally, we note that another way of calculating $\chi_{e,f}$ used in Ref. [15] (see Eq. (13) there), which gives "a near quantitative match with the mean-field theory" as claimed by Groot and Madden,[15] results in $\chi_{e,f}^*N \approx 16$ at both densities. Therefore, even with Eq. (3.12) and FH theory, we do not find the "quantitative match" for the ODT of symmetric DBC.

3.3.1.2 Lamellar period

Fig. 3.1 compares the mean-field bulk lamellar period $L_{0,\rm MF}$ for several models. Comparing the "standard" model with that of "CGC, $\sigma = 0$" reveals that decreasing N/κ from infinity

to 50π decreases $L_{0,\mathrm{MF}}$. Comparing the three cases of $N = 10$ (i.e., "DPD", "$\sigma/R_{e,0} = 0.1$", and "$\sigma = 0$") reveals that decreasing σ also decreases $L_{0,\mathrm{MF}}$. These are consistent with and well understood based on Ref. [34].

The same trends are observed for the exponent b defined via $L_{0,\mathrm{MF}} \propto (\chi N)^b$, which is a decreasing function of χN. In particular, we find that b quickly approaches 0 (i.e., $L_{0,\mathrm{MF}}$ quickly approaches a constant) with increasing χN for the case of discrete chains with Dirac δ-function interaction (i.e., "$N = 10$, $\sigma = 0$"); this unphysical behavior was also found and explained by Matsen in his recent SCF calculations of incompressible DBC melts modeled as freely jointed chains with a Gaussian non-bonded repulsive potential between A and B segments.[36] Combined with the aforementioned effects of N on $\chi^*_{\mathrm{MF}} N$ and $L^*_{0,\mathrm{MF}}$, this leads to the crossing of the two curves at $\sigma = 0$ (i.e., the "CGC" and "$N = 10$" cases).

Fig. 3.1 also shows the bulk lamellar period L_0 obtained from our FOMC simulations of the DPD model, where the results at each $\bar{\mathcal{N}}$ start from the corresponding $\chi^* N$ given in Table 3.2. To the best of our knowledge, this is the first unambiguous results showing

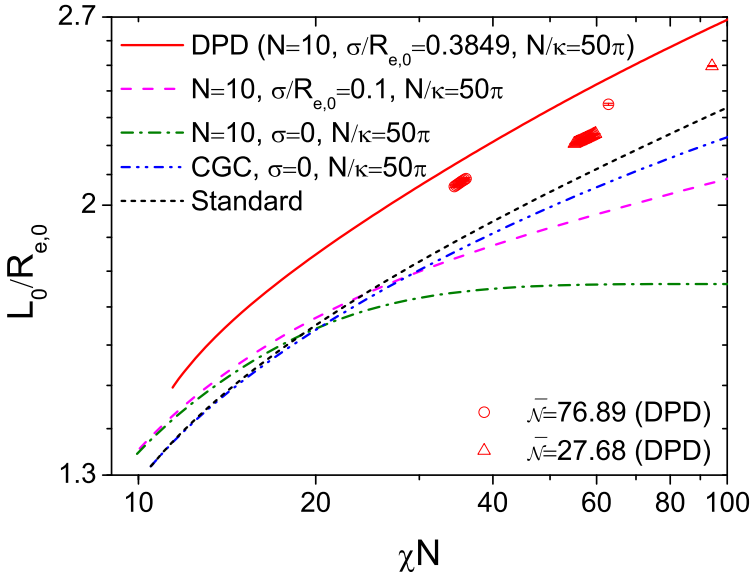

Figure 3.1: Logarithmic plot of the bulk lamellar period L_0 of symmetric diblock copolymers as a function of χN. The SCF results are shown in curves, where "Standard" denotes the "standard" model, and the FOMC results for the DPD model are shown in symbols.

that the system fluctuations/correlations decrease L_0. If one were to compare the FOMC results with $L_{0,\mathrm{MF}}$ for the "standard" model, the wrong conclusion that the system fluctuations/correlations increase L_0 would be drawn, and the effects of $\bar{\mathcal{N}}$ might be difficult to explain. Table 3.3 further compares $L_{0,\mathrm{MF}}$, that from variable-box FOMC simulations L_0, and the lamellar period from fixed-box DPD simulations L. We see that the deviation of L from L_0 is less than 3% due to the large box size used in the DPD simulations.

Table 3.3: Comparisons of the bulk period from SCF calculations $L_{0,\mathrm{MF}}$, that from variable-box FOMC simulations L_0, and the period from fixed-box simulations L for lamellae (at $f = 0.5$ and 0.4) and hexagonally packed cylinders (at $f = 0.3$) obtained with various parameters. [a] From Fig. 7 of Ref. [15]. [b] From the upper-left panel in Fig. 5 of Ref. [15]. [c] From Fig. 8 of Ref. [15]. [d] From our FOMC simulations. [e] From Fig. 9 of Ref. [15], see also Sec. 3.3.2.3. [f] From the lower-right panel in Fig. 6 of Ref. [15], see also Sec. 3.3.2.3.

f	χN	$\rho_0\sigma^3$	$\bar{\mathcal{N}}$	$L_{0,\mathrm{MF}}/R_{e,0}$	$L_0/R_{e,0}$	$L/R_{e,0}$
0.5	30π	3	≈ 28	2.658	2.497 ± 0.002	2.434[a]
0.5	20π	5	≈ 77	2.449	2.349 ± 0.004	2.321[b]
0.4	30π	3	≈ 28	2.653	2.497 ± 0.003	2.434[c]
0.4	20π	5	≈ 77	2.442	2.2001 ± 0.0002	2.222[d]
0.3	30π	3	≈ 28	2.796	2.600 ± 0.012	2.606 or 2.722[e]
0.3	20π	5	≈ 77	2.570	2.476 ± 0.004	2.407 or 2.500[f]

3.3.1.3 Segmental density profiles

Fig. 3.2(a) compares the ensemble-averaged profiles of the relative fraction of A segments in the direction (denoted by x) perpendicular to the lamellar interfaces, $\tilde{\phi}_{\mathrm{A}}(x) \equiv \langle \phi_{\mathrm{A}}(x)/[\phi_{\mathrm{A}}(x) + \phi_{\mathrm{B}}(x)] \rangle$, obtained from our SCF calculations and FOMC simulations at $\chi N = 30\pi$ ($\bar{\mathcal{N}} \approx 28$ in the simulations), where well-ordered lamellae form. As explained in Sec. 2.1.3 of Ref. [37], $\tilde{\phi}_{\mathrm{A}}(x)$ from FOMC simulations is obtained by aligning the collected profiles of $\phi_{\mathrm{A}}(x)/[\phi_{\mathrm{A}}(x) + \phi_{\mathrm{B}}(x)]$. Consistent with Ref. [37], we see that the A-B interfacial width (defined, for example, as $\left[\mathrm{d}\tilde{\phi}_{\mathrm{A}}(x)/\mathrm{d}x|_{x=0}\right]^{-1}$) in the FOMC simulations is larger

than that in the SCF calculations, due to the neglect of capillary-wave fluctuations at the interfaces by the latter.

On the other hand, Fig. 3.2(b) compares the ensemble-averaged profiles of the total segmental density in the x-direction, $\phi(x) \equiv \langle \phi_{\rm A}(x) + \phi_{\rm B}(x) \rangle$, obtained from our SCF calculations and FOMC simulations under the above condition. Note that $\phi(x)$ from FOMC simulations is also obtained by aligning the collected profiles of $\phi_{\rm A}(x) + \phi_{\rm B}(x)$ in the same

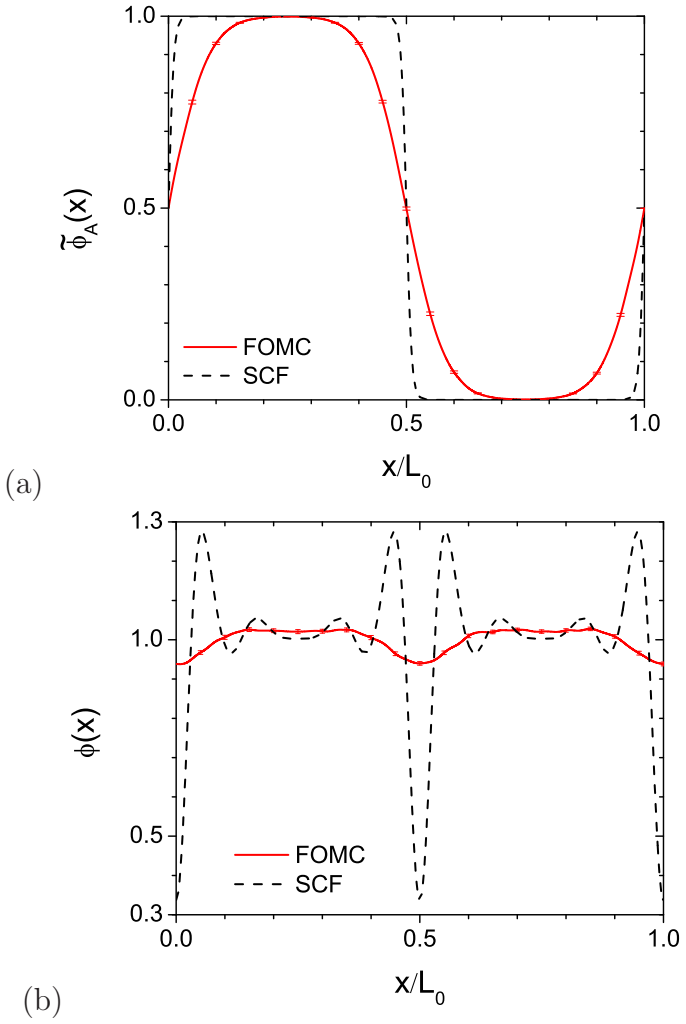

Figure 3.2: Comparisons of the ensemble-averaged profiles of (a) the relative fraction of A segments in the direction (denoted by x) perpendicular to the lamellar interfaces, $\tilde{\phi}_{\rm A}(x) \equiv \langle \phi_{\rm A}(x)/[\phi_{\rm A}(x) + \phi_{\rm B}(x)] \rangle$, and (b) the total segmental density in the x-direction, $\phi(x) \equiv \langle \phi_{\rm A}(x) + \phi_{\rm B}(x) \rangle$, obtained from our SCF calculations and FOMC simulations of the DPD model at $\chi N = 30\pi$ ($\bar{\mathcal{N}} \approx 28$ in the simulations), where the bulk lamellar period $L_0/R_{e,0} = 2.658$ in the SCF calculations and 2.497 ± 0.002 in the FOMC simulations.

way as above.[37] Different from the "standard" model, since the DPD model is compressible, the strong A-B repulsion results in the large depletion of $\phi(x)$ at the A-B interfaces as well as the oscillations of $\phi(x)$ in each lamellar domain enriched by A or B segments in SCF calculations, which are greatly suppressed by the system fluctuations in FOMC simulations. These are consistent with Figs. 6 and 7 of Ref. [37]; in fact, the DPD model is equivalent to DBC in an implicit, good and neutral solvent characterized by the second virial coefficient (or an excluded-volume parameter). Finally, we note that similar results are found at $\chi N = 20\pi$ ($\bar{\mathcal{N}} \approx 77$ in the simulations) and thus not shown.

3.3.2 Asymmetric DBC

3.3.2.1 SCF results

Fig. 3.3(a) compares the free energy per chain βf_c of various phases obtained from our SCF calculations of the DPD model at the A-block volume fraction in the copolymer $f = 0.4$. We see that, with increasing χN, the stable phase having the lowest βf_c changes in the sequence of D→S→C→G→L; the stable regions of the order phases are listed in Table 3.4. This sequence is the same as found for the "standard" model, but all the phase boundaries are shifted to higher χN compared to the latter, as also shown in Table 3.4. We attribute this to the finite interaction range $\sigma > 0$ in the DPD model, which is consistent with our RPA results on the mean-field ODT of symmetric DBC shown in Table 3.1. That $\sigma > 0$ shifts the phase boundaries to higher χN is also found by Matsen in his recent work.[36]

Fig. 3.3(b) compares βf_c of various phases obtained from our SCF calculations of the DPD model at $f = 0.3$, where L is unstable. In his recent work,[36] Matsen argued that L should be stable at large χN for discrete chains. While this trend could be seen in the inset of Fig. 3.3(b), for the DPD model we find that L remains unstable for χN up to at least 500. In addition, we have not been able to find G at all, suggesting that it also be unstable. With increasing χN, the stable phase now changes in the sequence of D→S→C. As in the above $f = 0.4$ case, this sequence is the same as found for the "standard" model with all the phase boundaries shifted to higher χN as shown in Table 3.4. The same is found at $f = 0.2$.

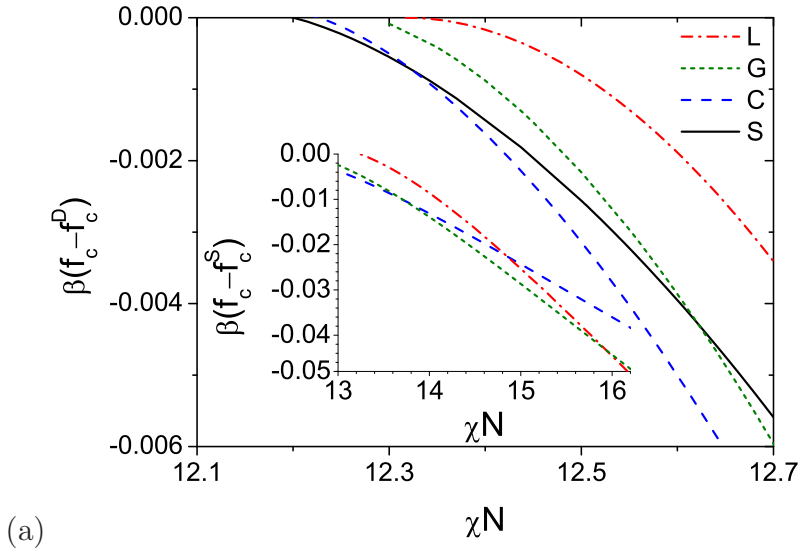

(a)

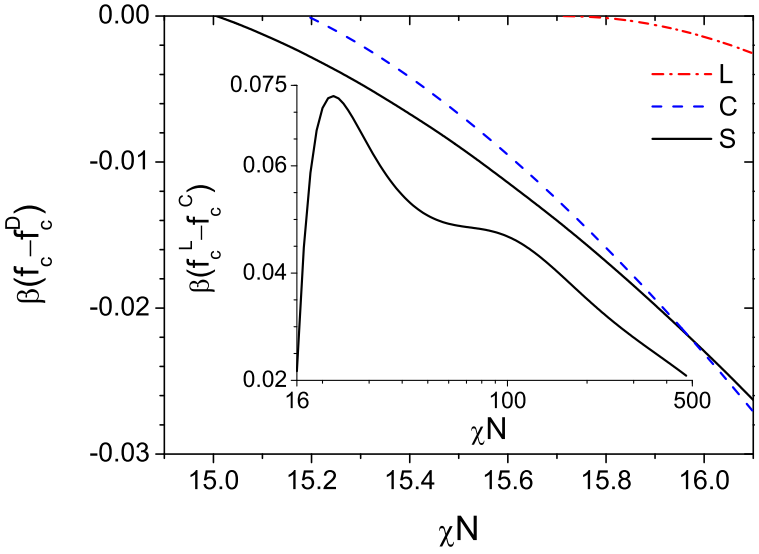

(b)

Figure 3.3: Differences in the free energy per chain βf_c of various ordered phases from that of the disordered phase βf_c^{D} obtained from our SCF calculations of the DPD model at (a) $f = 0.4$ and (b) $f = 0.3$. The inset of part (a) uses the free energy per chain of S, βf_c^{S}, as the reference, and the inset of part (b) shows the difference in the free energy per chain between L and C.

Table 3.4: Stable regions in χN of various ordered phases obtained from the SCF calculations of the DPD and the "standard" models; results for the latter model are provided by Mark Matsen. For each A-block volume fraction in the copolymer f, the stable phase (having the lowest Helmholtz free energy per chain) is replaced by that in a lower row at higher χN. The last column lists the χN-values at which the DPD simulations[15,17] were performed; the morphology obtained from the DPD simulations is given in parentheses if it is different from the SCF prediction. See main text for more details. [a] Also found at $f = 0.2$.

f	Phase	SCF Results		Morphology in DPD Simulations
		DPD model	"standard" model	
0.5	L	>11.427	>10.495	20π, 30π
0.4	S	>12.215	>11.231	
	C	>12.324	>11.373	
	G	>13.730	>12.786	
	L	>15.933	>15.352	20.5 ± 0.2 (D)[a], 41.1 ± 0.4 ("liquid rods"), 61.6 ± 0.6 ("random network"), 82.1 ± 0.8 ("like gyroid"), 30π, 102.7±1.0, 123.2±1.2
0.3	S	>15.007	>13.917	
	C	>15.970	>14.989	20π, 30π
0.2	S	>22.373	>21.136	
	C	>28.589	>27.740	41.1 ± 0.4 (D), 61.6 ± 0.6 ("micellar"), 20π ("micellar"), 82.1 ± 0.8 ("micellar"), 30π ("micellar"), 102.7 ± 1.0 ("long micellar"), 123.2 ± 1.2
0.1	S	>47.181	>47.956	30π (D)

Finally, at $f = 0.1$, our SCF results shown in Table 3.4 indicate that S is the only stable ordered phase, again consistent with the "standard" model. Different from the above cases, however, χN at the D/S transition is lower than that for the "standard" model. We attribute this to the finite chain discretization $N = 10$ in the DPD model (i.e., only one segment in the A-block), which is consistent with our RPA results on the mean-field ODT of symmetric DBC shown in Table 3.1.

3.3.2.2 FOMC results

At $f = 0.4$, Groot and Madden performed DPD simulations with $\rho_0\sigma^3 = 3$ (at $\chi N = 30\pi$) and 5 (at $\chi N = 20\pi$) using a cubic box of $(20\sigma)^3$. While the equilibrium morphology in the former case was found to be lamellae, they did not obtain the equilibrium morphology in the latter case due to the high density thus slow dynamics of the system (see the upper-right structure in Fig. 5 of Ref. [15]; their morphology for this case reported in Table II of Ref. [15] is incorrect). We therefore perform FOMC simulations using exactly the same parameters (including the box size) for this latter case, which give well-ordered lamellae as the equilibrium morphology.

For both cases, Table 3.3 compares the bulk lamellar period from our SCF calculations $L_{0,\mathrm{MF}}$, that from variable-box FOMC simulations L_0, and the lamellar period from fixed-box simulations L. We see that, as in the above $f = 0.5$ case, fluctuations decrease L_0. Finally, we again find that the capillary-wave fluctuations at the A-B interfaces increase the interfacial width, and that the system fluctuations greatly suppress the large depletion of the total segmental density at the A-B interfaces as well as its oscillations in lamellar domains predicted by our SCF calculations (data not shown).

At $f = 0.3$, Groot and Madden obtained hexagonally packed cylinders as the equilibrium morphology at both densities using a cubic box of $(20\sigma)^3$. Table 3.3 also compares the bulk period (intercylinder distance) from our SCF calculations $L_{0,\mathrm{MF}}$, that from variable-box FOMC simulations L_0, and the periods from the DPD simulations L. We again see that fluctuations decrease L_0. In their fixed-box simulations, the cylinders obtained by Groot and Madden are not arranged in a regular hexagonal pattern; we explain in Sec. 3.3.2.3 how to calculate their intercylinder distances, which were not reported in Ref. [15]. Finally, we also find that the capillary-wave fluctuations at the A-B interfaces increase the interfacial width, and that the system fluctuations greatly suppress the large depletion of the total segmental density at the A-B interfaces as well as its oscillations in A and B domains predicted by our SCF calculations (data not shown).

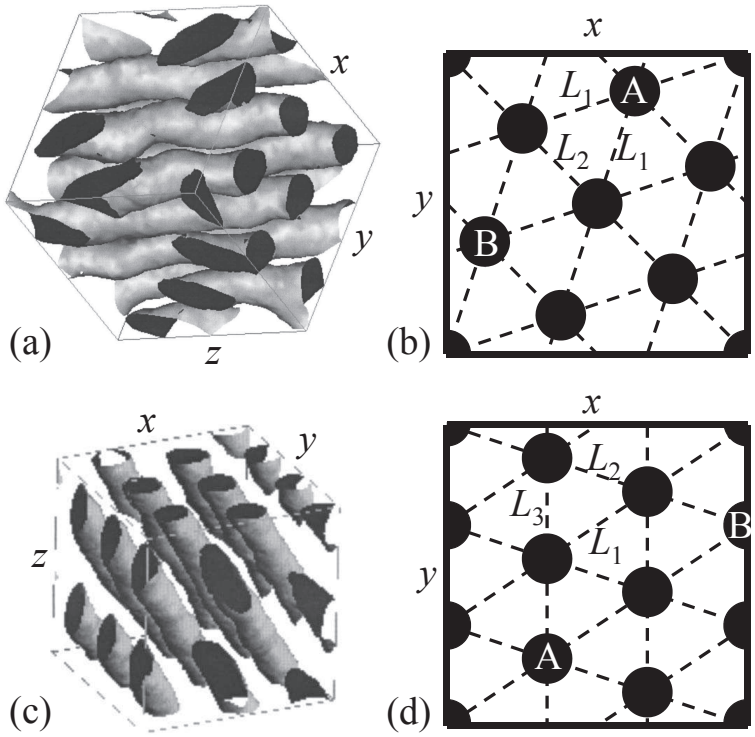

Figure 3.4: (a) Reproduced Fig. 9 in Ref. [15]. (b) Hexagonal packing of cylinders in any x-y cross section of the cubic simulation box shown in part (a). (c) Reproduced lower-right panel of Fig. 6 in Ref. [15]. (d) Hexagonal packing of cylinders in any x-y cross section of the cubic simulation box shown in part (c). See text for more details.

3.3.2.3 Intercylinder distances of hexagonally packed cylinders in a cubic simulation box

Here we show how to calculate the intercylinder distances when the cylinder axis is not parallel to any of the box surfaces. Taking Fig. 9 in Ref. [15] as an example, which is reproduced in Fig. 3.4(a), we schematically show in Fig. 3.4(b) the hexagonal packing of cylinders in any x-y cross section of the cubic simulation box (note the periodic boundary conditions). From this we find $L_1 = (\sqrt{5}/2)L_2 = (\sqrt{10}/8)L_b$, where L_1 and L_2 are marked in the figure, and $L_b = (40/3\sqrt{3})R_{e,0}$ is the box length. In addition, the cylinder axis is tilted at an angle of $\arcsin\sqrt{2/3}$ with respect to the x-y plane so that a cylinder passes through both circles (ellipses to be more precise) "A" at the right surface and "B" at the left surface of the simulation box. We therefore find the intercylinder distance $L/R_{e,0} = 2.606$ or 2.722 for this configuration.

Similarly, Fig. 3.4(d) is for the hexagonal packing of cylinders shown in the lower-right panel of Fig. 6 in Ref. [15], which is reproduced in Fig. 3.4(c). Here we find $L_1 = \sqrt{1.3}L_2 = (\sqrt{13}/3)L_3 = (\sqrt{13}/9)L_b$. In addition, the cylinder axis is tilted at an angle of $\arcsin(9/\sqrt{133})$ with respect to the x-y plane so that a cylinder passes through both "A" at the top surface and "B" at the bottom surface of the simulation box. We therefore find $L/R_{e,0} = 2.407$ or 2.500 for this configuration.

3.3.3 Comparing morphologies in SCF calculations and DPD simulations

Using a cubic box of $(20\sigma)^3$, Groot and Madden performed DPD simulations at $\chi N = 30\pi$ (with $\rho_0\sigma^3 = 3$) and 20π (with $\rho_0\sigma^3 = 5$),[15] and Chen et al. performed DPD simulations at more χN-values (with $\rho_0\sigma^3 = 3$).[17] Table 3.4 also lists the morphologies obtained in these DPD simulations; as the values of $\chi_e N$ instead of a_{ij} were reported in Ref. [17], their χN-values have a small error bar due to the use of Eq. (3.12). In eleven of the totally 20 cases (f-χN combinations) studied in these DPD simulations, a morphology different from that predicted by the SCF calculations was obtained, mostly at $f = 0.4$ and 0.2. We focus on these discrepancies in the following.

As shown in Table 3.2, our FOMC simulations give $\chi^* N = 55.08 \pm 0.47$ for symmetric DBC with $\rho_0\sigma^3 = 3$; for asymmetric DBC, we expect the ODT to be at higher χN, which means that the disordered phase found in the DPD simulations at $f = 0.4$ ($\chi N = 20.5 \pm 0.2$) and 0.2 ($\chi N = 41.1 \pm 0.4$)[17] is due to the large system fluctuations neglected in the SCF calculations. In the case of $f = 0.1$ ($\chi N = 30\pi$), where the ODT is unknown, mismatch between the cubic simulation box and the bulk period of S could also lead to the disordered phase found in the DPD simulations.[15] On the other hand, the "liquid rods" morphology found in the DPD simulations at $f = 0.4$ ($\chi N = 41.1 \pm 0.4$)[17] is questionable, as their χN-value is even below our ODT for symmetric DBC.

The "random network" and "like gyroid" morphologies found in the DPD simulations at $f = 0.4$ ($\chi N = 61.6 \pm 0.6$ and 82.1 ± 0.8, respectively)[17] are interesting and may correspond

to G in the SCF calculations. Mismatch between the cubic simulation box and the bulk period of G, however, needs to be considered, which strongly affects the observation of G in fixed-box simulations.[25]

Finally, the "micellar" and "long micellar" morphologies found in most DPD simulations at $f = 0.2$[15,17] may be due to the mismatch between the cubic simulation box and the bulk period of C or S. As DPD is a dynamic simulation technique, these poorly ordered morphologies could also be kinetically trapped. Since canonical-ensemble simulations cannot be used to find L_0 without accurate free-energy calculations,[25] we defer our FOMC simulations of S and G to a future study.

3.4 Summary

Using soft potentials such as that for the conservative force in the dissipative particle dynamics (DPD) simulations[1,2] is the basic idea of the so-called fast off-lattice Monte Carlo (FOMC) simulations,[5] which in principle give the same thermodynamic properties as DPD simulations.[2] In this work, we revisit the comparisons made by Groot and Madden[15,16] and Chen et al.[17] between their DPD simulations of the DPD model (i.e., a compressible system of discrete Gaussian chains each of $N = 10$ segments interacting with a finite-range (DPD) potential) and the self-consistent field (SCF) calculations of the "standard" model[13] (i.e., an incompressible system of continuous Gaussian chains interacting with the Dirac δ-function potential) for diblock copolymer (DBC) A-B melts, where the model differences were mixed with the following differences between the two methods: (1) DPD simulations sample the full spectrum of fluctuations/correlations of the system, which are neglected in SCF calculations; (2) morphologies found in DPD simulations could be kinetically trapped, while SCF calculation is an equilibrium approach; (3) the DPD simulations[15–17] are performed in a fixed-size box, which limits the allowed periods of the ordered structures,[20] while the SCF calculations[13] find the bulk period of all ordered phases; and (4) binary blends of DBC with different compositions (volume fractions of the A-block in the copolymer) f are used in most

of the DPD simulations by Groot and Madden,[15,16] while the SCF calculations[13] are for pure DBC systems.

We perform both SCF calculations and FOMC simulations in a canonical ensemble based on the DPD model; note that our FOMC simulations performed in variable-size boxes can find the bulk period of lamellar and cylindrical structures. Comparing our SCF results with those for the "standard" model therefore unambiguously reveals the effects of model differences (i.e., the system compressibility, chain discretization N, and interaction range σ), and comparing our SCF and FOMC results reveals, without any parameter-fitting, the effects of system fluctuations/correlations neglected in the SCF theory. Furthermore, comparing our FOMC results with the DPD results obtained in the same fixed-size box unambiguously identifies the kinetically trapped structures in the latter, and comparing our SCF (or FOMC) results in fixed- and variable-size boxes can unambiguously reveal the effects of fixed vs. bulk periods. For simplicity, we only consider systems of pure DBC and four ordered morphologies in this work: lamellae, hexagonally packed cylinders, spheres arranged on a body-centered cubic lattice, and the double-gyroid.

For symmetric DBC, the mean-field ODT $\chi^*_{\rm MF}N$ and the corresponding bulk lamellar period $L^*_{0,\rm MF}$ (as listed in Table 3.1) are not affected by the system compressibility N/κ[34] and the invariant degree of polymerization $\bar{\mathcal{N}}$, where χ and κ are the generalized Flory-Huggins interaction parameter and the generalized Helfand compressibility,[21,22] respectively, defined in the DPD model (see Eq. (3.3)). Consistent with Ref. [5, 34], we find that $\chi^*_{\rm MF}N$ increases with both increasing σ and increasing N, and $L^*_{0,\rm MF}$ increases with increasing σ but decreasing N. On the other hand, the ODT χ^*N and the corresponding bulk lamellar period L^*_0 determined from our FOMC simulations of the DPD model (as listed in Table 3.2) are significantly larger than the corresponding mean-field value due to the large system fluctuations/correlations expected for the small $\bar{\mathcal{N}}$-values used in the simulations. Such small $\bar{\mathcal{N}}$-values do not justify the use of the fluctuation theory of Fredrickson and Helfand[14] by Groot and Madden, and the parameter-fitting (i.e., the use of Eq. (3.12)) in their comparisons

with the SCF results of the "standard" model also has no rigorous basis. Even with these, we do not find the "quantitative match" for the ODT of symmetric DBC claimed by Groot and Madden.[15]

In addition, the mean-field bulk lamellar period $L_{0,\mathrm{MF}}$ decreases with decreasing N/κ and decreasing σ, consistent with Ref. [34]. The same trends are observed for the exponent b defined via $L_{0,\mathrm{MF}} \propto (\chi N)^b$. The system fluctuations/correlations, however, decrease the bulk period L_0. Finally, consistent with Refs. [37], for well-ordered lamellae we find that the capillary-wave fluctuations at the A-B interfaces increase the interfacial width, and that the system fluctuations greatly suppress the large depletion of the total segmental density at the A-B interfaces as well as its oscillations in lamellar domains predicted by our SCF calculations. Similar results are also found for well-ordered lamellae at $f = 0.4$ (and 0.6) and hexagonally packed cylinders at $f = 0.3$ (and 0.7).

As summarized in Table 3.4, at all values of f (which are integer multiples of 0.1) our SCF calculations of the DPD model give the same sequence of phase transitions with varying χN as the "standard" model. All phase boundaries, however, are shifted to higher χN due to $\sigma > 0$, except at $f = 0.1$ (and 0.9), where χN at the transition between the disordered phase and the spheres arranged on a body-centered cubic lattice is lower due to $N = 10$ in the DPD model. Finally, Table 3.4 also compares, without any parameter-fitting, the morphologies obtained in the DPD simulations[15,17] with the SCF predictions. In eleven of the totally 20 cases (f-χN combinations) studied in these DPD simulations, a morphology different from the SCF prediction was obtained due to the aforementioned differences (1)$\sim$(3) between the two methods.

We emphasize that the goal of this work is not to invalidate the DPD model/method, but to highlight the importance of quantitative and parameter-fitting-free comparisons among different models/methods. In fact, with the numerical SCF calculations well-developed and widely applied to various polymeric systems,[38] it is of great interest to achieve quantitative understanding of the fluctuation/correlation effects neglected by the SCF calculations.

For this purpose, it is invaluable to develop particle-based models/methods such as DPD[1,2] or FOMC[5] simulations and field-based models/methods such as the field-theoretic simulations.[39] Direct comparisons between these simulations and SCF calculations based on the same model system, thus without any parameter-fitting, can unambiguously quantify the fluctuation/correlation effects in the system.[9–11]

REFERENCES

[1] P. J. Hoogerbrugge and J. M. V. A. Koelman, Europhys. Lett. **19**, 155 (1992).

[2] P. Espanol and P. B. Warren, Europhys. Lett. **30**, 191 (1995).

[3] S. M. Willemsen, T. J. H. Vlugt, H. C. J. Hoefsloot, and B. Smit, J. Comput. Phys. **147**, 507 (1998).

[4] C. M. Wijmans, B. Smit, and R. D. Groot, J. Chem. Phys. **114**, 7644 (2001).

[5] Q. Wang and Y. Yin, J. Chem. Phys. **130**, 104903 (2009).

[6] Q. Wang, Soft Matter **5**, 4564 (2009); **6**, 6206 (2010).

[7] F. A. Detcheverry, D. Q. Pike, P. F. Nealey, M. Muller, and J. J. de Pablo, Phys. Rev. Lett. **102**, 197801 (2009).

[8] D. Q. Pike, F. A. Detcheverry, M. Muller, and J. J. de Pablo, J. Chem. Phys. **131**, 084903 (2009).

[9] P. Zhang, X. Zhang, B. Li, and Q. Wang, Soft Matter **7**, 4461 (2011).

[10] P. Zhang, B. Li, and Q. Wang, Macromolecules **44**, 7837 (2011).

[11] P. Zhang, B. Li, and Q. Wang, Macromolecules **45**, 2537 (2012).

[12] J. Zong, X. Zhang, and Q. Wang, J. Chem. Phys. **137**, 134904 (2012).

[13] M. W. Matsen and F. S. Bates, Macromolecules **29**, 1091 (1996).

[14] G. H. Fredrickson and E. Helfand, J. Chem. Phys. **87**, 697 (1987).

[15] R. D. Groot and T. J. Madden, J. Chem. Phys. **108**, 8713 (1998).

[16] R. D. Groot and T. J. Madden, *Structure and Dynamics of Materials in the Mesoscopic Domain*, 288, (ed.) M. Lal, R. A. Mashelkar, B. D. Kulkarni, and V. M. Naik, 4th Meeting of the Royal-Society-Unilever-Indo-UK Forum in Materials Science and Engineering, Natl. Chem. Lab, Pune, India, 1999.

[17] L. J. Chen, Z. Y. Lu, H. J. Qian, Z. S. Li, and C. C. Sun, J. Chem. Phys. **122**, 104907 (2005).

[18] S. A. Brazovskii, Sov. Phys. JETP **41**, 85 (1975).

[19] T. Ohta and K. Kawasaki, Macromolecules **19**, 2621 (1986).

[20] Q. Wang, Q. L. Yan, P. F. Nealey, and J. J. de Pablo, J. Chem. Phys. **112**, 450 (2000).

[21] E. Helfand and Y. Tagami, J. Polym. Sci. Part B: Polym. Lett. **9**, 741 (1971).

[22] E. Helfand and Y. Tagami, J. Chem. Phys. **56**, 3592 (1972).

[23] J. Zong and Q. Wang, J. Chem. Phys. **139**, 124907 (2013).

[24] Q. Wang, P. F. Nealey, and J. J. de Pablo, Macromolecules **34**, 3458 (2001).

[25] F. J. Martinez-Veracoechea and F. A. Escobedo, J. Chem. Phys. **125**, 104907 (2006).

[26] R. H. Swendsen and J. S. Wang, Phys. Rev. Lett **57**, 2607 (1986).

[27] A. M. Ferrenberg and R. H. Swendsen, Phys. Rev. Lett. **63**, 1195 (1989).

[28] M. Muller and N. B. Wilding, Phys. Rev. E **51**, 2079 (1995).

[29] P.-G. de Gennes, *Scaling Concepts in Polymer Physics*, Cornell University Press, Ithaca and London, 1979.

[30] http://www.fftw.org.

[31] W. H. Press, S. A. Teukolsky, W. T. Vetterling, and B. P. Flannery, Chap. 9.7 in *Numerical Recipes in C: the Art of Scientific Computing*, 2nd ed., Cambridge University Press, Cambridge, 2002.

[32] R. B. Thompson, K. O. Rasmussen, and T. Lookman, J. Chem. Phys. **120**, 31 (2004); M. W. Matsen, Eur. Phys. J. E **30**, 361 (2009).

[33] W. H. Press, S. A. Teukolsky, W. T. Vetterling, and B. P. Flannery, Chap. 4.3 in *Numerical Recipes in C: the Art of Scientific Computing*, 2nd ed., Cambridge University Press, Cambridge, 2002.

[34] Q. Wang, J. Chem. Phys. **129**, 054904 (2008).

[35] R. D. Groot and P. B. Warren, J. Chem. Phys. **107**, 4423 (1997).

[36] M. W. Matsen, Macromolecules **45**, 8502 (2012).

[37] Q. Wang, P. F. Nealey, and J. J. de Pablo, Macromolecules **35**, 9563 (2002).

[38] G. H. Fredrickson, *The Equilibrium Theory of Inhomogeneous Polymers*, Oxford University Press, Oxford, 2006.

[39] G. H. Fredrickson, V. Ganesan, and F. Drolet, Macromolecules **35**, 16 (2002).

CHAPTER 4

ON THE ORDER-DISORDER TRANSITION OF COMPRESSIBLE DIBLOCK COPOLYMER MELTS

4.1 Introduction

The shift of order-disorder transition (ODT) of block copolymer melts from the corresponding mean-field prediction due to fluctuations is a classic problem in polymer physics.[1,2] In a seminal work, Leibler predicted that the mean-field ODT of symmetric diblock copolymer (DBC) A-B melts is a second-order phase transition given by $\chi^*_{\rm MF}N \approx 10.495$, where χ is the Flory-Huggins interaction parameter characterizing the repulsion between A and B segments and N the total number of segments on each copolymer chain.[1] In another seminal work, Fredrickson and Helfand (FH) predicted that the ODT of symmetric DBC melts becomes a first-order phase transition due to fluctuations and its shift is given by $\chi^*/\chi^*_{\rm MF} - 1 = 3.91\bar{\mathcal{N}}^{-1/3}$, where the invariant degree of polymerization $\bar{\mathcal{N}} \equiv (nR^3_{e,0}/V)^2$ is for n copolymer chains in volume V with $R_{e,0}$ denoting the root-mean-square end-to-end distance of an ideal chain.[2] While many groups have since then performed molecular simulations to study the ODT shift,[3–13] this problem is complicated in most studies by the different model systems used in the simulations and the mean-field theory (thus the definition of χ). For example, Leibler's mean-field prediction is only for continuous Gaussian chains (where $N \to \infty$) with the Dirac δ-function interactions,[14,15] neither of which can be used in particle-based simulations. To the best of our knowledge, only three groups used exactly the same model system in both their recent simulations and the corresponding mean-field theory.[4,5,8–11]

In this work, we focus on another common difference between particle-based simulations and the standard field theories of DBC melts,[1,2,16,17] i.e., the incompressibility constraint

requiring that the polymer volume fraction be 1 everywhere in the system; while enforced in the standard field theories, it cannot be used in particle-based simulations in continuum.[18] For incompressible DBC melts, the determination of ODT when it is a first-order phase transition (e.g., given by mean-field theories for asymmetric DBC) is simplified, where the ordered and disordered phases have the same density and Helmholtz free energy per chain, and the ODT is given by a single χ-value. In contrast, for compressible DBC melts, ODT as a first-order phase transition corresponds to a range of χ-values, over which the two phases co-exist with the same pressure and chain chemical potential but different densities (thus different Helmholtz free energies per chain). Since real DBC melts are compressible, density change of two co-existing phases has been found at ODT in experiments.[19] To the best of our knowledge, however, such a co-existing range has not been determined in either simulations or mean-field theories.

We therefore use both the self-consistent field calculations and fast off-lattice Monte Carlo simulations to determine the ODT of a model system of compressible DBC melts when it is a first-order phase transition, and compare with our previous results obtained by equating the Helmholtz free energy per chain of the two phases[9,10] in Chapters 2 and 3. We find that the co-existing range is quite small and decreases as the system becomes less compressible, which justifies the previous results in Chapters 2 and 3 where it was assumed that the co-existing phases have the same density. We also find that, for the most compressible model system where there is no interaction between the same type of segments, the self-consistent field theory predicts the ODT to be a second-order phase transition even for asymmetric DBC melts.

4.2 Model and Methods

4.2.1 Model system

We consider compressible DBC melts of n chains, each having N_{A} segments of type A followed by N_{B} segments of B, in volume V at thermodynamic temperature T. The volume fraction

of A block in the copolymer is denoted by $f \equiv N_{\rm A}/N$ with $N \equiv N_{\rm A} + N_{\rm B}$. The Hamiltonian of our model system is given by $\mathcal{H} = \mathcal{H}^C + \mathcal{H}^E$, where

$$\mathcal{H}^C = \sum_{k=1}^{n} \sum_{s=1}^{N-1} u_{k,s}^b$$

is due to the chain connectivity modeled by discrete Gaussian chains (DGC), with the bonding potential $u_{k,s}^b = (3/2a^2\beta)\left(\mathbf{R}_{k,s+1} - \mathbf{R}_{k,s}\right)^2$, $\beta \equiv 1/k_BT$, k_B being the Boltzmann constant, a the effective bond length, and $\mathbf{R}_{k,s}$ the spatial position of the $s^{\rm th}$ segment on the $k^{\rm th}$ chain; and

$$\begin{aligned}\mathcal{H}^E = \frac{1}{2}\int {\rm d}\mathbf{r}{\rm d}\mathbf{r}' \left[\hat{\rho}_{\rm A}(\mathbf{r})\epsilon u_0(|\mathbf{r}-\mathbf{r}'|)\hat{\rho}_{\rm A}(\mathbf{r}') + 2\hat{\rho}_{\rm A}(\mathbf{r})\epsilon_{\rm AB}u_0(|\mathbf{r}-\mathbf{r}'|)\hat{\rho}_{\rm B}(\mathbf{r}')\right. \\ \left. +\hat{\rho}_{\rm B}(\mathbf{r})\epsilon u_0(|\mathbf{r}-\mathbf{r}'|)\hat{\rho}_{\rm B}(\mathbf{r}')\right] - \frac{nN}{2}\epsilon u_0(0) \end{aligned} \tag{4.1}$$

is due to the non-bonded interactions, with ϵ and $\epsilon_{\rm AB}$ being the repulsion strength between two segments of the same and different types, respectively, $\hat{\rho}_{\rm A}(\mathbf{r}) \equiv \sum_{k=1}^{n}\sum_{s=1}^{N_{\rm A}} \delta(\mathbf{r} - \mathbf{R}_{k,s})$ and $\hat{\rho}_{\rm B}(\mathbf{r}) \equiv \sum_{k=1}^{n}\sum_{s=N_{\rm A}+1}^{N} \delta(\mathbf{r} - \mathbf{R}_{k,s})$ being the microscopic number density of A and B segments at spatial position $\mathbf{r}$, respectively, and the last term deducting the self-interaction. Finally, the non-bonded pair potential

$$u_0(r) = \begin{cases} (15/2\pi\sigma^3\beta)(1 - r/\sigma)^2 & \text{if } r < \sigma \\ 0 & \text{otherwise} \end{cases}$$

is normalized (i.e., $\int {\rm d}\mathbf{r}\beta u_0(r) = 1$ in 3D) and isotropic (i.e., depends only on the distance r between two segments) with σ denoting the finite interaction range. This is essentially the same as the non-bonded pair potential for the conservative force used in the dissipative particle dynamics (DPD) simulations.[20]

Note that our model system is the same as that used Chapters 2 and 3 with

$$N/\kappa \equiv \rho_c N^2 \epsilon \tag{4.2}$$

and

$$\chi N \equiv \rho_c N^2 \left(\epsilon_{\rm AB} - \epsilon\right), \tag{4.3}$$

where the chain number density $\rho_c \equiv n/V$, and κ and χ denote the generalized Helfand compressibility[21] and the generalized Flory-Huggins parameter, respectively. As explicitly shown in Chapter 3, this model is equivalent to that used by Groot and Madden in their DPD simulations of DBC microphase separation.[22] It is also equivalent to the soft models S1, S2, and S3 recently used by Morse and co-workers to study the ODT of symmetric DBC;[12,13] in particular, we find

$$\frac{N}{\kappa} = \frac{5\pi}{3} \frac{N^2 \sqrt{\bar{\mathcal{N}}}}{[3(N-1)/k]^{3/2}} \tag{4.4}$$

in their soft models, where the invariant degree of polymerization $\bar{\mathcal{N}} = (\rho_c R_{e,0}^3)^2$ with the root-mean-square end-to-end distance of an ideal chain $R_{e,0} = \sqrt{N-1}a$, and k is the "κ" in Eq. (12) of Ref. [13].

Hereafter we take $R_{e,0}$ as the length scale. We finally note that ϵ and ϵ_{AB} (just like N, f, a and σ) must be the same for the two phases at equilibrium, because they control the interactions between polymer segments; in other words, κ and χ are different if the two phases have different ρ_c, but satisfy

$$\frac{\chi^{\mathrm{O}}}{\chi^{\mathrm{D}}} = \frac{\kappa^{\mathrm{D}}}{\kappa^{\mathrm{O}}} = \frac{\rho_c^{\mathrm{O}}}{\rho_c^{\mathrm{D}}}, \tag{4.5}$$

where the superscripts "O" and "D" denote the ordered and disordered phases, respectively, at equilibrium.

4.2.2 Fast off-lattice Monte Carlo (FOMC) simulations

We perform FOMC simulations of our model system to compare the ODT of symmetric DBC melts determined using two different methods. In the first method, our simulations are performed in a canonical (nVT) ensemble using a variable-length, rectangular parallelepipedal simulation box with the periodic boundary conditions applied in all directions, where the two equilibrium (D and L) phases have the same chain number density ρ_c (or equivalently the invariant degree of polymerization $\bar{\mathcal{N}}$) and the Helmholtz free energy per chain βf_c. This is actually done in Chapter 2. In particular, for $N = 10$, $\sigma/a = 0.3$, and $\bar{\mathcal{N}} = 10^4$, we found that $\chi^* N = 25.67 \pm 0.23$ and 81.66 ± 0.54 at $N/\kappa^* = 0$ and 50, respectively;[10] these two

cases correspond to $\epsilon = 0$ and $\epsilon_{\rm AB} = 0.002567$ (Case I) and $\epsilon = 0.005$ and $\epsilon_{\rm AB} = 0.013166$ (Case II), and will be examined here.

In the second method, we perform simulations in an isothermal-isobaric (nPT) ensemble in a similar way to our previous nVT simulations,[10] but replace the trial move of box-length change previously used at constant V by that of volume change, where we generate the new box length along the j ($= x, y, z$) direction as $L_{j,\rm new} = L_{j,\rm old} \exp(\xi)$; here $L_{j,\rm old}$ is the box length before the trial move, ξ is a random number uniformly distributed within $(-\xi_{\rm max}, \xi_{\rm max})$ and used for all directions, and the maximum displacement $\xi_{\rm max}$ is adjusted at the beginning of equilibration to achieve about 50% acceptance rate of the volume-change trial moves. As in our previous nVT simulations in Chapter 2, we further use the replica-exchange (RE) of configurations, but now at different (adjacent) pressures[23] instead of χ-values previously used, to greatly reduce the sample correlation length. The acceptance criterion for swapping two configurations i and j at pressure P_i and P_j, respectively, is $P_{\rm acc} = \min\{1, \exp[\beta(P_i - P_j)(V_i - V_j)]\}$, where V_i and V_j denote the corresponding volume.

To compare with our previous nVT simulations of the above two cases, we use the same parameters (i.e., N, σ/a, ϵ, and $\epsilon_{\rm AB}$) and perform $R = 16$ parallel nPT simulations with RE at different pressures around those of the D and L phases at the ODT determined in our nVT simulations, which are found to be $\beta P^{\rm D} = 280.9 \pm 1.1$ and $\beta P^{\rm L} = 278.6 \pm 1.1$ for Case I, and $\beta P^{\rm D} = 1944.0 \pm 1.9$ and $\beta P^{\rm L} = 1938.1 \pm 2.0$ for Case II. In addition, we use the lamellar structure obtained from our previous nVT simulations[10] as the initial configuration. For more details, we refer the readers to Chapter 2.

Finally, we use the multiple histogram reweighting technique,[24] which is nicely combined with RE, to accurately locate the ODT. For totally R simulation runs performed at the same N, σ/a, ϵ and $\epsilon_{\rm AB}$ but at different P_i ($i = 1, \ldots, R$), we collect the histogram $H_i(E, V, \Psi)$ at each pressure P_i, where E denotes the system energy and Ψ the scalar order parameter used in our previous work[10] to characterize the degree of positional order in lamellae. The unnormalized probability for the system having E, V and Ψ at given P within the pressure

range of our simulations is then given by

$$\tilde{p}_b(E,V,\Psi|P) = \frac{\sum_{i=1}^{R} g_i^{-1} H_i(E,V,\Psi)\exp[\beta(E+PV)]}{\sum_{j=1}^{R} g_j^{-1} M_j H_j(E,V,\Psi)\exp[\beta(E+P_jV)-C_j]},$$

where g_j is the statistical inefficiency of the collected V in the j^{th} run, M_j is the total number of collected samples after equilibration in the j^{th} run, and $\exp(C_j) = \sum_E \sum_V \sum_\Psi \tilde{p}_b(E,V,\Psi|P_j)$; note that $\exp(C_j)$ is proportional to the nPT-ensemble partition function at P_j.[25] We then calculate the normalized two-dimensional histogram $p_b(\rho_c,\Psi|P) = \sum_E \tilde{p}_b(E,V,\Psi|P)/\left[\sum_E \sum_V \sum_\Psi \tilde{p}_b(E,V,\Psi|P)\Delta\Psi n\Delta V/\left(V-\Delta V/2\right)\left(V+\Delta V/2\right)\right]$ with ΔV and $\Delta\Psi$ being bin sizes used for V and Ψ, respectively, and determine the pressure P^* at the ODT from the equal-weight criterion[26]

$$\sum_{\Psi<\Psi^*}\sum_{\rho_c} p_b(\rho_c,\Psi|P^*) = \sum_{\Psi>\Psi^*}\sum_{\rho_c} p_b(\rho_c,\Psi|P^*), \tag{4.6}$$

where $\Psi^* \equiv \langle\Psi\rangle(P^*)$. Note that the equal-weight criterion is equivalent to setting the Gibbs free energies per chain of the two co-existing phases at P^* to be the same.[27]

Once P^* (thus Ψ^*) is determined, all samples (at all pressures) with $\Psi < \Psi^*$ are considered as the disordered (D) phase, and the rest are considered as the ordered (O) phase; averaging over these two phases, respectively, then gives the ensemble-averaged chain number densities of the two phases at the ODT, ρ_c^{D} and ρ_c^{O}, from which N/κ^{D}, $\chi^{\text{D}}N$, N/κ^{O} and $\chi^{\text{O}}N$ can be obtained according to Eqs. (4.2) and (4.3). Finally, we note that, to estimate the statistical errors of P^*, ρ_c^{D} and ρ_c^{O}, we calculate these quantities using the first- and second-half of our samples collected after equilibration, respectively, then take three times their largest deviation from the corresponding value determined using all the samples as the error bar.

4.2.3 Self-consistent field (SCF) calculations

The SCF equations for the model system are derived in Chapter 3 and given by

$$\hat{\omega}_{\text{A}}(\mathbf{k}) = \frac{N}{\kappa}\beta\hat{u}_0(k)\left[\hat{\phi}_{\text{A}}(\mathbf{k})+\hat{\phi}_{\text{B}}(\mathbf{k})\right] + \chi N\beta\hat{u}_0(k)\hat{\phi}_{\text{B}}(\mathbf{k}) \tag{4.7}$$

$$\hat{\omega}_{\rm B}(\mathbf{k}) = \frac{N}{\kappa}\beta\hat{u}_0(k)\left[\hat{\phi}_{\rm A}(\mathbf{k}) + \hat{\phi}_{\rm B}(\mathbf{k})\right] + \chi N\beta\hat{u}_0(k)\hat{\phi}_{\rm A}(\mathbf{k}) \tag{4.8}$$

$$\phi_{\rm A}(\mathbf{r}) = \frac{\exp[\omega_{\rm A}(\mathbf{r})/N]}{NQ}\sum_{s=1}^{N_{\rm A}} q_s(\mathbf{r})q^*_{N-s+1}(\mathbf{r}) \tag{4.9}$$

$$\phi_{\rm B}(\mathbf{r}) = \frac{\exp[\omega_{\rm B}(\mathbf{r})/N]}{NQ}\sum_{s=N_{\rm A}+1}^{N} q_s(\mathbf{r})q^*_{N-s+1}(\mathbf{r}), \tag{4.10}$$

where $\phi_{\rm P}(\mathbf{r})$ and $\omega_{\rm P}(\mathbf{r})$ (P = A, B) are the normalized segment number density (volume fraction) field constrained to $\hat{\rho}_{\rm P}(\mathbf{r})/N\rho_c$ and the conjugate field imposing the constraint, respectively; the Fourier transform of $\omega_{\rm P}(\mathbf{r})$, for example, is denoted by $\hat{\omega}_{\rm P}(\mathbf{k}) \equiv \int {\rm d}\mathbf{r}\exp(-i\mathbf{k}\cdot\mathbf{r})\omega_{\rm P}(\mathbf{r})$ with $\mathbf{k}$ being the wave-vector and $k \equiv |\mathbf{k}|$; $Q = \hat{q}_N(\mathbf{k} = \mathbf{0})/V$ is the single-chain partition function; and $q_s(\mathbf{r})$ and $q^*_t(\mathbf{r})$ are the propagators satisfying the Chapman-Kolmogorov equation (CKE)[28]

$$q_{s+1}(\mathbf{r}) = \begin{cases} \exp[-\omega_{\rm A}(\mathbf{r})/N]\int {\rm d}\mathbf{r}'\Phi(|\mathbf{r}-\mathbf{r}'|)q_s(\mathbf{r}') & \text{for } s = 1,\ldots,N_{\rm A}-1 \\ \exp[-\omega_{\rm B}(\mathbf{r})/N]\int {\rm d}\mathbf{r}'\Phi(|\mathbf{r}-\mathbf{r}'|)q_s(\mathbf{r}') & \text{for } s = N_{\rm A},\ldots,N-1 \end{cases} \tag{4.11}$$

and

$$q^*_{t+1}(\mathbf{r}) = \begin{cases} \exp[-\omega_{\rm B}(\mathbf{r})/N]\int {\rm d}\mathbf{r}'\Phi(|\mathbf{r}-\mathbf{r}'|)q^*_t(\mathbf{r}') & \text{for } t = 1,\ldots,N_{\rm B}-1 \\ \exp[-\omega_{\rm A}(\mathbf{r})/N]\int {\rm d}\mathbf{r}'\Phi(|\mathbf{r}-\mathbf{r}'|)q^*_t(\mathbf{r}') & \text{for } t = N_{\rm B},\ldots,N-1 \end{cases}, \tag{4.12}$$

respectively, with the initial conditions $q_1(\mathbf{r}) = \exp[-\omega_{\rm A}(\mathbf{r})/N]$ and $q^*_1(\mathbf{r}) = \exp[-\omega_{\rm B}(\mathbf{r})/N]$, and $\Phi(r) = [3(N-1)/2\pi]^{3/2}\exp\left[-3(N-1)r^2/2\right]$. Once the SCF equations are solved, the mean-field Helmholtz free energy per chain can be calculated as

$$\beta f_c = -\rho_c\tau - \ln Q + \ln\rho_c - 1 \tag{4.13}$$

with $\tau \equiv \int {\rm d}\mathbf{r}\left[\omega_{\rm A}(\mathbf{r})\phi_{\rm A}(\mathbf{r}) + \omega_{\rm B}(\mathbf{r})\phi_{\rm B}(\mathbf{r})\right]/2n$; this is equivalent to Eq. 3.11 in Chapter 3 (where the last two terms in the above Eq. 4.13 is omitted). Note that, as a mean-field theory, SCF theory becomes exact in the limit of $\rho_c \to \infty$ (i.e., $\epsilon \to 0$ and $\epsilon_{\rm AB} \to 0$, while κ and χ remain finite), where the system has no fluctuations/correlations. On the other hand, the value of ρ_c cannot (and needs not to) be calculated in SCF theory (that of $\rho_c\tau$, however, can be calculated).

In our SCF calculations, we consider two ordered phases of asymmetric DBC: lamellae (L) in 1D and hexagonally packed cylinders (C) in 2D, where a calculation cell of size L_b and $L_b \times \sqrt{3}L_b$ are used, respectively, with the periodic boundary conditions applied in all directions. For each ordered phase at given N, f, σ/a, N/κ and χN, we solve the SCF equations and obtain their bulk period L_0 (which minimizes βf_c) using the same methods as in Chapter 3, but with finer spatial discretization and more stringent convergence criteria to ensure an accuracy of at least 10^{-12} in our calculated βf_c.

We then use two different methods to determine the ODT. In the first method (which was used in Chapter 3), the two phases are assumed to have the same ρ_c and the ODT (denoted by χ^*) is determined from $\beta f_c^{\mathrm{O}} = \beta f_c^{\mathrm{D}}$. Since $\beta f_c^{\mathrm{D}} = N/2\kappa + f\,(1-f)\,\chi N + \ln \rho_c - 1$, we solve for χ^* at given κ^* from

$$-\rho_c \tau^{\mathrm{O}}(\kappa^*, \chi^*) - \ln Q^{\mathrm{O}}(\kappa^*, \chi^*) = \frac{N}{2\kappa^*} + f\,(1-f)\,\chi^* N \tag{4.14}$$

using the Newton-Raphson method with a convergence criterion of 10^{-11}; hereafter, we omit the property dependence of the ordered phase on N, f and σ/a. Since the mean-field ODT between L and D phases is always a second-order phase transition regardless of f, it can also be obtained by analyzing the stability of the D phase using the random-phase approximation given in Sec. 4.2.4.

In the second method, the two phases co-exist at the same dimensionless pressure

$$\beta P \equiv -\left(\frac{\partial n \beta f_c}{\partial V}\right)_{n,\beta} = \rho_c^2 \tau + \rho_c \tag{4.15}$$

and chain chemical potential

$$\beta \mu \equiv \left(\frac{\partial n \beta f_c}{\partial n}\right)_{V,\beta} = -\ln Q + \ln \rho_c, \tag{4.16}$$

where their derivation is given in Sec. 4.2.5. Since $\beta P^{\mathrm{D}} = \rho_c[N/2\kappa + f(1-f)\chi N + 1]$ and $\beta \mu^{\mathrm{D}} = N/\kappa + 2f(1-f)\chi N + \ln \rho_c$, we can solve for κ^{D}, χ^{D}, and χ^{O} at given κ^{O} (thus the ODT) from

$$\rho_c^{\mathrm{O}} \left[\rho_c^{\mathrm{O}} \tau^{\mathrm{O}}(\kappa^{\mathrm{O}}, \chi^{\mathrm{O}}) + 1\right] = \rho_c^{\mathrm{D}} \left[N/2\kappa^{\mathrm{D}} + f(1-f)\chi^{\mathrm{D}} N + 1\right], \tag{4.17}$$

$$-\ln Q^{\mathrm{O}}(\kappa^{\mathrm{O}},\chi^{\mathrm{O}})+\ln\rho_c^{\mathrm{O}}=N/\kappa^{\mathrm{D}}+2f(1-f)\chi^{\mathrm{D}}N+\ln\rho_c^{\mathrm{D}}, \tag{4.18}$$

and Eq. (4.5). In particular, since Eq. (4.17), after Eq. (4.5) is used to eliminate $\rho_c^{\mathrm{O}}/\rho_c^{\mathrm{D}}$ and κ^{D}, is a quadratic equation of $\chi^{\mathrm{D}}>0$, these three equations can be de-coupled and solved sequentially; we again use the Newton-Raphson method with a convergence criterion of 10^{-11}. Finally, when ODT is a second-order phase transition, the above two methods become equivalent.

4.2.4 Random-Phase Approximation

Following the Appendix of Ref. [15], we find the second-order term in the expansion of the Helmholtz free energy per chain βf_c around the disordered phase as

$$\beta f_c^{(2)}=\frac{1}{V}\int\frac{\mathrm{d}\mathbf{k}}{(2\pi)^3}\begin{bmatrix}\widehat{\delta\phi}_{\mathrm{A}}(\mathbf{k})\\ \widehat{\delta\phi}_{\mathrm{B}}(\mathbf{k})\end{bmatrix}\cdot\mathbf{S}^{-1}(k)\begin{bmatrix}\widehat{\delta\phi}_{\mathrm{A}}(-\mathbf{k})\\ \widehat{\delta\phi}_{\mathrm{B}}(-\mathbf{k})\end{bmatrix},$$

where $\delta\phi_{\mathrm{A}}(\mathbf{r})=\phi_{\mathrm{A}}(\mathbf{r})-f$, $\delta\phi_{\mathrm{B}}(\mathbf{r})=\phi_{\mathrm{B}}(\mathbf{r})-(1-f)$, and

$$\mathbf{S}^{-1}=\begin{bmatrix}(N/\kappa)\hat{u}_0(k)+4P_{\mathrm{A}}(x)/\Delta P(x) & (\chi N+N/\kappa)\hat{u}_0(k)-2P_{\mathrm{B}}(x)/\Delta P(x)\\ (\chi N+N/\kappa)\hat{u}_0(k)-2P_{\mathrm{B}}(x)/\Delta P(x) & (N/\kappa)\hat{u}_0(k)+4P_{\mathrm{A}}(x)/\Delta P(x)\end{bmatrix}$$

with $x\equiv k^2Na^2/6$, $P_{\mathrm{A}}(x)=P(f,x)$, $P_{\mathrm{B}}(x)=P(1-f,x)$, $P_{\mathrm{AB}}(x)=P(1,x)-P_{\mathrm{A}}(x)-P_{\mathrm{B}}(x)$, $\Delta P(x)=4P_{\mathrm{A}}(x)P_{\mathrm{B}}(x)-P_{\mathrm{AB}}^2(x)$, and

$$P(f,x)=\frac{N\left(1-e^{-x/N}\right)\left(1+e^{-x/N}\right)f+2e^{-x/N}\left(e^{-xf}-1\right)}{N^2\left(1-e^{-x/N}\right)^2}.$$

The two eigenvalues λ_1 and λ_2 of $\mathbf{S}^{-1}$ are given by

$$\lambda_1(k)=\frac{2P_{\mathrm{A}}+2P_{\mathrm{B}}-\zeta}{\Delta P}+\frac{N}{\kappa}\hat{u}_0,$$
$$\lambda_2(k)=\frac{2P_{\mathrm{A}}+2P_{\mathrm{B}}+\zeta}{\Delta P}+\frac{N}{\kappa}\hat{u}_0,$$

with

$$\zeta=\sqrt{4\left(P_{\mathrm{A}}-P_{\mathrm{B}}\right)^2+\left[2P_{\mathrm{AB}}-\left(\chi N+N/\kappa\right)\hat{u}_0\Delta P\right]^2}.$$

Since $\hat{u}_0(k)>0$ and $\Delta P(x)\geq 0$ with the equal sign taken only at $x=0$, the ODT at given N/κ^* is then obtained by setting to 0 the minimum of λ_1 with respect to k, i.e., solving $\chi^*_{\mathrm{RPA}}N$ and k^*_{RPA} from two coupled equations $\lambda_1=0$ and $\mathrm{d}\lambda_1/\mathrm{d}k=0$.

4.2.5 Pressure and Chemical Potential in SCF Theory

With Eqs. (4.2) and (4.3), Eq. (4.7) can be re-written in real space as

$$\omega_{\mathrm{A}}(\mathbf{r}) = \frac{nN^2\epsilon}{V}\int \mathrm{d}\mathbf{r}'\beta u_0\left(|\mathbf{r}-\mathbf{r}'|\right)\phi_{\mathrm{A}}(\mathbf{r}') + \frac{nN^2\epsilon_{\mathrm{AB}}}{V}\int \mathrm{d}\mathbf{r}'\beta u_0\left(|\mathbf{r}-\mathbf{r}'|\right)\phi_{\mathrm{B}}(\mathbf{r}').$$

Because the interaction range of $\beta u_0\left(|\mathbf{r}-\mathbf{r}'|\right)$ is finite, $\int \mathrm{d}\mathbf{r}'\beta u_0\left(|\mathbf{r}-\mathbf{r}'|\right)\phi_{\mathrm{P}}(\mathbf{r}')$ $(\mathrm{P}=\mathrm{A},\mathrm{B})$ is not a function of V. We therefore have $\left[\partial\omega_{\mathrm{A}}(\mathbf{r})/\partial n\right]_V = \omega_{\mathrm{A}}(\mathbf{r})/n$ and $\left[\partial\omega_{\mathrm{A}}(\mathbf{r})/\partial V\right]_n = -\omega_{\mathrm{A}}(\mathbf{r})/V$. Similarly, from Eq. (4.8) we have $\left[\partial\omega_{\mathrm{B}}(\mathbf{r})/\partial n\right]_V = \omega_{\mathrm{B}}(\mathbf{r})/n$ and $\left[\partial\omega_{\mathrm{B}}(\mathbf{r})/\partial V\right]_n = -\omega_{\mathrm{B}}(\mathbf{r})/V$. Note that we have used $\left[\partial\phi_{\mathrm{P}}(\mathbf{r})/\partial V\right]_n = \left[\partial\phi_{\mathrm{P}}(\mathbf{r})/\partial n\right]_V = 0$ $(\mathrm{P}=\mathrm{A},\mathrm{B})$ here.

The single-chain partition function is defined as[17]

$$Q \equiv \frac{1}{G}\prod_{s=1}^{N}\int \mathrm{d}\mathbf{R}_s \cdot P(\{\mathbf{R}_s\})\cdot W(\{\mathbf{R}_s\}), \tag{4.19}$$

where $\mathbf{R}_s$ denotes the spatial position of the s^{th} segment on the chain, $P(\{\mathbf{R}_s\}) \equiv \exp\left[-(3/2a^2)\sum_{s=1}^{N-1}\left(\mathbf{R}_{s+1}-\mathbf{R}_s\right)^2\right]$, $G \equiv \prod_{s=1}^{N}\int \mathrm{d}\mathbf{R}_s \cdot P(\{\mathbf{R}_s\}) = V\left[3(N-1)/2\pi\right]^{3(1-N)/2}$, and $W(\{\mathbf{R}_s\}) \equiv \exp\left[-\sum_{s=1}^{N_{\mathrm{A}}}\omega_{\mathrm{A}}(\mathbf{R}_s)/N - \sum_{s=N_{\mathrm{A}}+1}^{N}\omega_{\mathrm{B}}(\mathbf{R}_s)/N\right]$. Introducing the bond vector $\mathbf{b}_s \equiv \mathbf{R}_{s+1}-\mathbf{R}_s$ and the normalized spatial position $\tilde{\mathbf{R}}_1 \equiv \mathbf{R}_1/V$, we can re-write Q as

$$\begin{aligned} Q = & \frac{V}{G}\int \mathrm{d}\tilde{\mathbf{R}}_1 \prod_{s=1}^{N-1}\int \mathrm{d}\mathbf{b}_s \exp\left(-\frac{3}{2a^2}\mathbf{b}_s^2\right) \\ & \cdot \exp\left[-\frac{1}{N}\sum_{s=1}^{N_{\mathrm{A}}}\omega_{\mathrm{A}}(V\tilde{\mathbf{R}}_1 + \sum_{s'=1}^{s-1}\mathbf{b}_{s'}) - \frac{1}{N}\sum_{s=N_{\mathrm{A}}+1}^{N}\omega_{\mathrm{B}}(V\tilde{\mathbf{R}}_1 + \sum_{s'=1}^{s-1}\mathbf{b}_{s'})\right]. \end{aligned}$$

We therefore have

$$\begin{aligned} \left(\frac{\partial \ln Q}{\partial V}\right)_n = & \frac{V}{GQ}\int \mathrm{d}\tilde{\mathbf{R}}_1 \prod_{s=1}^{N-1}\int \mathrm{d}\mathbf{b}_s \exp\left(-\frac{3}{2a^2}\mathbf{b}_s^2\right) \\ & \cdot \left(\frac{\partial}{\partial V}\exp\left[-\frac{1}{N}\sum_{s=1}^{N_{\mathrm{A}}}\omega_{\mathrm{A}}(V\tilde{\mathbf{R}}_1 + \sum_{s'=1}^{s-1}\mathbf{b}_{s'}) - \frac{1}{N}\sum_{s=N_{\mathrm{A}}+1}^{N}\omega_{\mathrm{B}}(V\tilde{\mathbf{R}}_1 + \sum_{s'=1}^{s-1}\mathbf{b}_{s'})\right]\right)_n \\ = & \frac{1}{GQ}\prod_{s=1}^{N}\int \mathrm{d}\mathbf{R}_s \cdot P(\{\mathbf{R}_s\})\cdot\left[\frac{\partial W(\{\mathbf{R}_s\})}{\partial V}\right]_n \\ = & \frac{1}{GQVN}\prod_{s=1}^{N}\int \mathrm{d}\mathbf{R}_s \cdot P(\{\mathbf{R}_s\})\cdot W(\{\mathbf{R}_s\})\cdot\left[\sum_{s'=1}^{N_{\mathrm{A}}}\omega_{\mathrm{A}}(\mathbf{R}_{s'}) + \sum_{s'=N_{\mathrm{A}}+1}^{N}\omega_{\mathrm{B}}(\mathbf{R}_{s'})\right] \end{aligned}$$

$$
\begin{aligned}
&= \frac{1}{GQVN}\left[\sum_{s'=1}^{N_{\mathrm{A}}}\prod_{s=1}^{N}\int \mathrm{d}\mathbf{R}_s\omega_{\mathrm{A}}(\mathbf{R}_{s'})\cdot P(\{\mathbf{R}_s\})\cdot W(\{\mathbf{R}_s\})\right.\\
&\qquad\left.+\sum_{s'=N_{\mathrm{A}}+1}^{N}\prod_{s=1}^{N}\int \mathrm{d}\mathbf{R}_s\omega_{\mathrm{B}}(\mathbf{R}_{s'})\cdot P(\{\mathbf{R}_s\})\cdot W(\{\mathbf{R}_s\})\right]\\
&= \frac{1}{V^2}\int \mathrm{d}\mathbf{r}\omega_{\mathrm{A}}(\mathbf{r})\frac{1}{NQ}\exp\left[\omega_{\mathrm{A}}(\mathbf{r})/N\right]\sum_{s'=1}^{N_{\mathrm{A}}} q_{s'}(\mathbf{r})q^*_{N-s'+1}(\mathbf{r})\\
&\quad+\frac{1}{V^2}\int \mathrm{d}\mathbf{r}\omega_{\mathrm{B}}(\mathbf{r})\frac{1}{NQ}\exp\left[\omega_{\mathrm{B}}(\mathbf{r})/N\right]\sum_{s'=N_{\mathrm{A}}+1}^{N} q_{s'}(\mathbf{r})q^*_{N-s'+1}(\mathbf{r})\\
&= \frac{1}{V^2}\int \mathrm{d}\mathbf{r}\left[\omega_{\mathrm{A}}(\mathbf{r})\phi_{\mathrm{A}}(\mathbf{r})+\omega_{\mathrm{B}}(\mathbf{r})\phi_{\mathrm{B}}(\mathbf{r})\right]\\
&= \frac{2n\tau}{V^2},
\end{aligned}
$$

and

$$
\begin{aligned}
\left(\frac{\partial \ln Q}{\partial n}\right)_V &= \frac{1}{GQ}\prod_{s=1}^{N}\int \mathrm{d}\mathbf{R}_s\cdot P(\{\mathbf{R}_s\})\cdot\left[\frac{\partial W(\{\mathbf{R}_s\})}{\partial n}\right]_V\\
&= -\frac{1}{nGQN}\prod_{s=1}^{N}\int \mathrm{d}\mathbf{R}_s\cdot P(\{\mathbf{R}_s\})\cdot W(\{\mathbf{R}_s\})\cdot\left[\sum_{s'=1}^{N_{\mathrm{A}}}\omega_{\mathrm{A}}(\mathbf{R}_{s'})+\sum_{s'=N_{\mathrm{A}}+1}^{N}\omega_{\mathrm{B}}(\mathbf{R}_{s'})\right]\\
&= -\frac{1}{nGQN}\left[\sum_{s'=1}^{N_{\mathrm{A}}}\prod_{s=1}^{N}\int \mathrm{d}\mathbf{R}_s\omega_{\mathrm{A}}(\mathbf{R}_{s'})\cdot P(\{\mathbf{R}_s\})\cdot W(\{\mathbf{R}_s\})\right.\\
&\qquad\left.-\sum_{s'=N_{\mathrm{A}}+1}^{N}\prod_{s=1}^{N}\int \mathrm{d}\mathbf{R}_s\omega_{\mathrm{B}}(\mathbf{R}_{s'})\cdot P(\{\mathbf{R}_s\})\cdot W(\{\mathbf{R}_s\})\right]\\
&= -\frac{1}{nV}\int \mathrm{d}\mathbf{r}\omega_{\mathrm{A}}(\mathbf{r})\frac{1}{NQ}\exp\left[\omega_{\mathrm{A}}(\mathbf{r})/N\right]\sum_{s'=1}^{N_{\mathrm{A}}} q_{s'}(\mathbf{r})q^*_{N-s'+1}(\mathbf{r})\\
&\quad-\frac{1}{nV}\int \mathrm{d}\mathbf{r}\omega_{\mathrm{B}}(\mathbf{r})\frac{1}{NQ}\exp\left[\omega_{\mathrm{B}}(\mathbf{r})/N\right]\sum_{s'=N_{\mathrm{A}}+1}^{N} q_{s'}(\mathbf{r})q^*_{N-s'+1}(\mathbf{r})\\
&= -\frac{1}{nV}\int \mathrm{d}\mathbf{r}\left[\omega_{\mathrm{A}}(\mathbf{r})\phi_{\mathrm{A}}(\mathbf{r})+\omega_{\mathrm{B}}(\mathbf{r})\phi_{\mathrm{B}}(\mathbf{r})\right]\\
&= -\frac{2\tau}{V};
\end{aligned}
$$

note that we have used the relation

$$
\prod_{s=1}^{N}\int \mathrm{d}\mathbf{R}_s\omega_{\mathrm{P}}(\mathbf{R}_{s'})\cdot P(\{\mathbf{R}_s\})\cdot W(\{\mathbf{R}_s\}) = \frac{G}{V}\int \mathrm{d}\mathbf{r}\omega_{\mathrm{P}}(\mathbf{r})\exp\left[\frac{\omega_{\mathrm{P}}(\mathbf{r})}{N}\right] q_{s'}(\mathbf{r})q^*_{N-s'+1}(\mathbf{r})
$$

to derive the fifth and third equalities in the above two derivations, respectively.

On the other hand, with the normalized spatial position $\tilde{\mathbf{r}} \equiv \mathbf{r}/V$, we have

$$\begin{aligned}\left(\frac{\partial\tau}{\partial V}\right)_n &= \frac{1}{2n}\left[\frac{\partial}{\partial V}\left(V\int \mathrm{d}\tilde{\mathbf{r}}\,[\omega_{\mathrm{A}}(\mathbf{r})\phi_{\mathrm{A}}(\mathbf{r})+\omega_{\mathrm{B}}(\mathbf{r})\phi_{\mathrm{B}}(\mathbf{r})]\right)\right]_n \\ &= \frac{1}{2n}\int \mathrm{d}\tilde{\mathbf{r}}\left[\omega_{\mathrm{A}}(\mathbf{r})\phi_{\mathrm{A}}(\mathbf{r})+\omega_{\mathrm{B}}(\mathbf{r})\phi_{\mathrm{B}}(\mathbf{r})+V\left(\frac{\partial}{\partial V}\left[\omega_{\mathrm{A}}(\mathbf{r})\phi_{\mathrm{A}}(\mathbf{r})+\omega_{\mathrm{B}}(\mathbf{r})\phi_{\mathrm{B}}(\mathbf{r})\right]\right)_n\right] \\ &= \frac{1}{2n}\int \mathrm{d}\tilde{\mathbf{r}}\,[\omega_{\mathrm{A}}(\mathbf{r})\phi_{\mathrm{A}}(\mathbf{r})+\omega_{\mathrm{B}}(\mathbf{r})\phi_{\mathrm{B}}(\mathbf{r})] - \frac{1}{2n}\int \mathrm{d}\tilde{\mathbf{r}}\,[\omega_{\mathrm{A}}(\mathbf{r})\phi_{\mathrm{A}}(\mathbf{r})+\omega_{\mathrm{B}}(\mathbf{r})\phi_{\mathrm{B}}(\mathbf{r})] \\ &= 0,\end{aligned}$$

and

$$\begin{aligned}\left(\frac{\partial\tau}{\partial n}\right)_V &= -\frac{1}{2n^2}\int \mathrm{d}\mathbf{r}\,[\omega_{\mathrm{A}}(\mathbf{r})\phi_{\mathrm{A}}(\mathbf{r})+\omega_{\mathrm{B}}(\mathbf{r})\phi_{\mathrm{B}}(\mathbf{r})] + \frac{1}{2n}\int \mathrm{d}\mathbf{r}\left[\frac{\omega_{\mathrm{A}}(\mathbf{r})}{n}\phi_{\mathrm{A}}(\mathbf{r})+\frac{\omega_{\mathrm{B}}(\mathbf{r})}{n}\phi_{\mathrm{B}}(\mathbf{r})\right] \\ &= 0.\end{aligned}$$

Therefore, from Eq. (4.13), we have

$$\beta P \equiv -\left(\frac{\partial n\beta f_c}{\partial V}\right)_{n,\beta} = \frac{n^2\tau}{V^2} + \frac{n}{V}, \tag{4.20}$$

and

$$\beta\mu \equiv \left(\frac{\partial n\beta f_c}{\partial n}\right)_{V,\beta} = -\ln Q + \ln\frac{n}{V}. \tag{4.21}$$

4.3 Results and Discussion

4.3.1 FOMC simulations of symmetric DBC

Here we compare the ODT of symmetric DBC melts with $N = 10$ and $\sigma/a = 0.3$ determined in FOMC simulations using two different methods. In the first method, our simulations are performed in a canonical (nVT) ensemble.[10] We assume that the two (D and L) phases at equilibrium have the same chain number density $\rho_c = 10^2$ (thus the Helmholtz free energy per chain βf_c), and found that $\chi^* N = 25.67 \pm 0.23$ and 81.66 ± 0.54 at $N/\kappa^* = 0$ and 50, respectively;[10] these two cases correspond to $\epsilon = 0$ and $\epsilon_{\mathrm{AB}} = 0.002567$ (Case I) and $\epsilon = 0.005$ and $\epsilon_{\mathrm{AB}} = 0.013166$ (Case II), where the dimensionless pressures of the two phases at the ODT are found to be $\beta P^{\mathrm{D}} = 280.9 \pm 1.1$ and $\beta P^{\mathrm{O}} = 278.6 \pm 1.1$ for Case I, and $\beta P^{\mathrm{D}} = 1944.0 \pm 1.9$ and $\beta P^{\mathrm{O}} = 1938.1 \pm 2.0$ for Case II.

In the second method, we perform simulations in an isothermal-isobaric (nPT) ensemble. Fig. 4.1 shows the normalized $p_b(\rho_c, \Psi|P^*)$ for Case I at the ODT pressure $\beta P^* = 278.4 \pm 0.3$ determined as described in Sec. 4.2.2. We find that $\rho_c^{\mathrm{D}} = 93.96 \pm 0.31$ and $\rho_c^{\mathrm{O}} = 100.54 \pm 0.11$, thus $\chi^{\mathrm{D}} N = 24.12 \pm 0.15$ and $\chi^{\mathrm{O}} N = 25.81 \pm 0.03$, for the two co-existing phases at the ODT. We therefore see small differences between the ODT determined using the two methods; in particular, $\chi^* N$ is close to $\chi^{\mathrm{O}} N$ but distinct from $\chi^{\mathrm{D}} N$, and the same is found for the pressures.

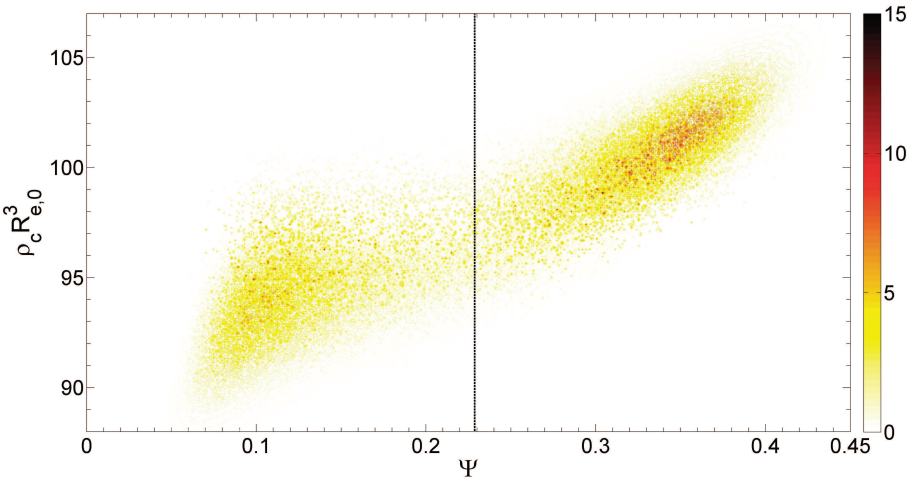

Figure 4.1: Normalized two-dimensional histogram $p_b(\rho_c, \Psi|P^*)$ for $N/\kappa = 0$ with $N = 10$, $f = 0.5$, $\sigma/a = 0.3$, $\epsilon = 0$ and $\epsilon_{\mathrm{AB}} = 0.002567$ in nPT simulation. The transition pressure $\beta P^* R_{e,0}^3 = 278.44$, and the vertical black dashed line marks $\langle \Psi \rangle (P^*)$.

Similarly, Fig. 4.2 shows the normalized $p_b(\rho_c, \Psi|P^*)$ for Case II at the ODT pressure $\beta P^* = 1948.9 \pm 3.8$ determined as described in Sec. 4.2.2. We find that $\rho_c^{\mathrm{D}} = 99.99 \pm 0.73$ and $\rho_c^{\mathrm{O}} = 100.27 \pm 0.72$, thus $N/\kappa^{\mathrm{D}} = 49.99 \pm 0.36$, $N/\kappa^{\mathrm{O}} = 50.13 \pm 0.36$, $\chi^{\mathrm{D}} N = 81.65 \pm 0.59$ and $\chi^{\mathrm{O}} N = 81.88 \pm 0.59$, for the two co-existing phases at the ODT. In this case, we find no difference between the ODT determined using the two methods within their error bars.

Comparing Cases I and II, we conclude that the difference between the ODT determined using the two methods is small and decreases with increasing N/κ^*. This validates our ODT results obtained in nVT simulations in Chapter 2 (where $N/\kappa^* = 0$ and 50) and Chapter 3

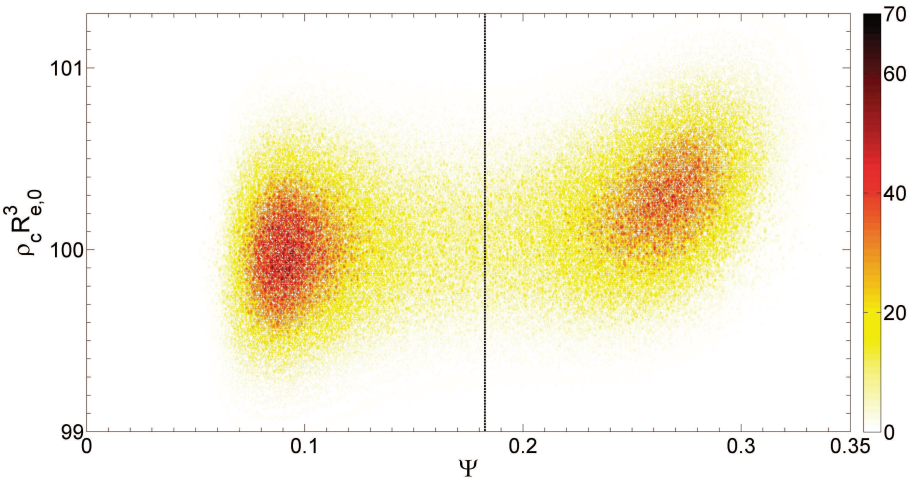

Figure 4.2: Normalized two-dimensional histogram $p_b(\rho_c, \Psi|P^*)$ for $N/\kappa = 50$ with $N = 10$, $f = 0.5$, $\sigma/a = 0.3$, $\epsilon = 0.005$ and $\epsilon_{\rm AB} = 0.013166$ in nPT simulation. The transition pressure $\beta P^* R_{e,0}^3 = 1949.32$, and the vertical black dashed line marks $\langle\Psi\rangle\,(P^*)$.

(where $N/\kappa^* = 50\pi$). On the other hand, according to Eq. (4.4), Morse and co-workers used $N/\kappa^* = 157 \sim 3170$ in Refs. [12, 13]; given their large values of N/κ^* (i.e., nearly incompressible systems), this work justifies their underlying assumption that the D and L phases at equilibrium have the same ρ_c.

4.3.2 SCF calculations of asymmetric DBC

4.3.2.1 ODT between D and C phases

Fig. 4.3(a) compares the mean-field ODT between D and C phases determined using the two different methods in our SCF calculations at $N = 10$, $f = 0.4$ and $\sigma/a = 2/\sqrt{3}$. For asymmetric DBC melts, the mean-field ODT is a first-order phase transition, except at $N/\kappa = 0$ as explained below. In the first method, we assume that the two phases at equilibrium have the same chain number density ρ_c (thus the Helmholtz free energy per chain βf_c) and obtain the ODT curve of $\chi^* N$ vs. N/κ^*. We see that $\chi^* N$ monotonically increases with increasing N/κ^* and approaches $\chi^\infty N \approx 12.242$ in the limit of $N/\kappa^* \to \infty$ (i.e., for incompressible DBC melts). The region above the curve of $\chi^* N$ vs. N/κ^* is the cylindrical phase, and that below the curve is the disordered phase.

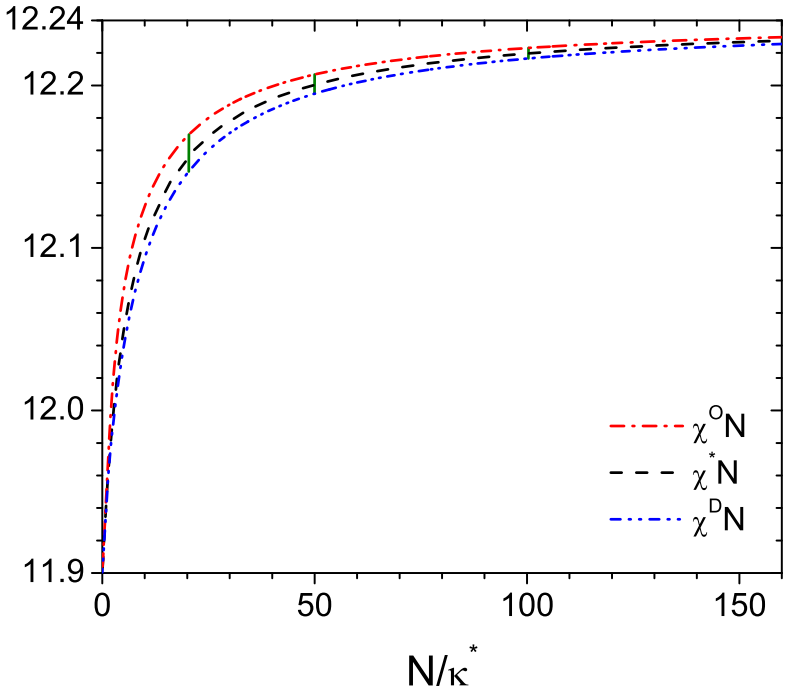

(a)

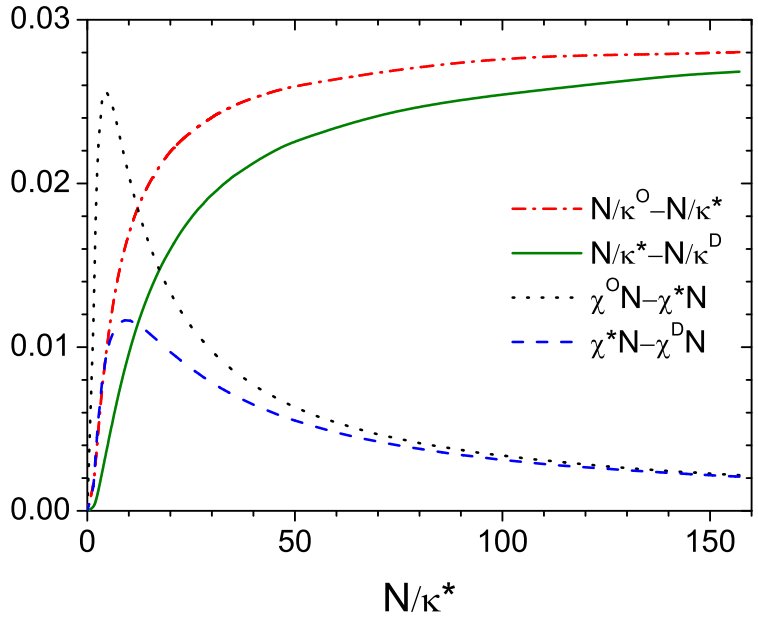

(b)

Figure 4.3: (a) ODT as a function of N/κ for C phase obtained in the first and second method in SCF calculation with $N = 10$, $f = 0.4$ and $\sigma/a = 2/\sqrt{3}$. (b) $N/\kappa^{\mathrm{O}} - N/\kappa^{*}$, $N/\kappa^{*} - N/\kappa^{\mathrm{D}}$, $\chi^{\mathrm{O}}N - \chi^{*}N$, and $\chi^{*}N - \chi^{\mathrm{D}}N$ vs. N/κ^{*} with $N = 10$, $f = 0.4$ and $\sigma/a = 2/\sqrt{3}$.

In the second method, we equate the dimensionless pressure βP and chain chemical potential $\beta\mu$ of the two phases, from which along with Eq. (4.5) we can solve for $\chi^{\rm O}$, $\chi^{\rm D}$ and $\kappa^{\rm D}$ at given $\kappa^{\rm O}$. We see that both $\chi^{\rm O}N$ and $\chi^{\rm D}N$ monotonically increase with increasing N/κ^* (or $N/\kappa^{\rm O}$ and $N/\kappa^{\rm D}$, respectively), and approach $\chi^{\infty}N$ for incompressible DBC melts, where the two methods become identical. The region above the curve of $\chi^{\rm O}N$ vs. N/κ^* is the cylindrical phase, that below the curve of $\chi^{\rm D}N$ vs. N/κ^* is the disordered phase, and that between these two curves is where the two phases co-exist. In addition, the straight line connecting the two points $(N/\kappa^{\rm D}, \chi^{\rm D}N)$ and $(N/\kappa^{\rm O}, \chi^{\rm O}N)$ is the tie line, and our calculations always give $\chi^{\rm O}N > \chi^{\rm D}N$ (thus $N/\kappa^{\rm O} > N/\kappa^{\rm D}$ according to Eq. (4.5)) at finite $N/\kappa^{\rm D} > 0$ (that is, the tie lines are not vertical but tilt towards right in Fig. 4.3(a)). Finally, we note that the curve of χ^*N vs. N/κ^* lies in-between those of $\chi^{\rm O}N$ vs. $N/\kappa^{\rm O}$ and $\chi^{\rm D}N$ vs. $N/\kappa^{\rm D}$, and that the point where a tie line intersects with the curve of χ^*N vs. N/κ^* has the same ϵ and $\epsilon_{\rm AB}$, thus corresponding to the same system, as other points on the tie line. The differences between the two methods for determining ODT are therefore clearly revealed by those between the intersection and the two end points of the tie line.

To quantify these differences, Fig. 4.3(b) shows $N/\kappa^{\rm O} - N/\kappa^*$, $N/\kappa^* - N/\kappa^{\rm D}$, $\chi^{\rm O}N - \chi^*N$, and $\chi^*N - \chi^{\rm D}N$ vs. N/κ^*. We see that both $N/\kappa^{\rm O} - N/\kappa^*$ and $N/\kappa^* - N/\kappa^{\rm D}$ monotonically increase with increasing N/κ^* and seem to level off at large N/κ^*. In contrast, $\chi^{\rm O}N - \chi^*N$ and $\chi^*N - \chi^{\rm D}N$ exhibit a maximum around $N/\kappa^* = 4.44$ and $N/\kappa^* = 9.01$, and scale with $(N/\kappa^*)^{-0.959}$ and $(N/\kappa^*)^{-0.913}$ at large N/κ^*, respectively (data not shown). While the results at large N/κ^* are consistent with the fact that the two methods become identical for incompressible DBC melts (where the transition between C and D phases is a first-order phase transition), those at small N/κ^* are due to the fact that SCF theory gives a second-order phase transition at $N/\kappa^* = 0$, where $N/\kappa^{\rm O} = N/\kappa^{\rm D} = N/\kappa^*$ and $\chi^{\rm D}N = \chi^{\rm O}N = \chi^*N = 11.900$.

4.3.2.2 *Second-order phase transition at $N/\kappa = 0$*

It is well known that SCF theory gives a second-order phase transition between D and L phases regardless of f. The χN-value at this transition, denoted by $\chi^*_{\rm RPA}N$, can be accurately obtained by analyzing the stability of the D phase using the random-phase approximation (which is the same as the ODT between D and L phases obtained from SCF calculations). The inset of Fig. 4.4(a) shows $\chi^*_{\rm RPA}N$ vs. N/κ^* for $N = 10$, $f = 0.4$ and $\sigma/a = 2/\sqrt{3}$; note that, while for symmetric DBC $\chi^*_{\rm RPA}N$ does not depend on N/κ^*,[14] for asymmetric DBC it does. On the other hand, Fig. 4.4(a) shows $(\chi^*_{\rm RPA} - \chi^*)N$ vs. N/κ^*, where χ^*N is the ODT between D and C phases obtained via SCF calculations using the first method explained above. We see that, while SCF theory gives a first-order transition between D and C phases as indicated by $\chi^*_{\rm RPA} > \chi^*$ for $N/\kappa > 0$, $(\chi^*_{\rm RPA} - \chi^*)N$ quickly decreases towards 0 as N/κ approaches 0, thus suggesting a second-order phase transition between D and C phases in the case of $N/\kappa = 0$.

Fig. 4.4(b) shows the difference in the Helmholtz free energy per chain βf_c between D and an ordered phase (L or C) as a function of $(\chi - \chi^*_{\rm RPA})N$ at $N/\kappa = 0$. We find that $\beta(f_c^{\rm D} - f_c^{\rm L}) \propto (\chi - \chi^*_{\rm RPA})^{2.00}$ and $\beta(f_c^{\rm D} - f_c^{\rm C}) \propto (\chi - \chi^*_{\rm RPA})^{2.95}$ at small $(\chi - \chi^*_{\rm RPA})N$, suggesting that both the transition between D and L phases and that between D and C phases are of the second-order at $N/\kappa = 0$. We also note that it is difficult to obtain χ^*N accurately in SCF calculations at small $N/\kappa \lesssim 1$ due to the very small difference in βf_c between D and C phases.

4.4 Conclusions

Using both the self-consistent field (SCF) calculations and fast off-lattice Monte Carlo (FOMC) simulations, we investigate the effect of compressibility on the order-disorder transition (ODT) of diblock copolymer (DBC) melts. We apply two different methods to determine the ODT: in the first method, the co-existing ordered and disordered phases have the same

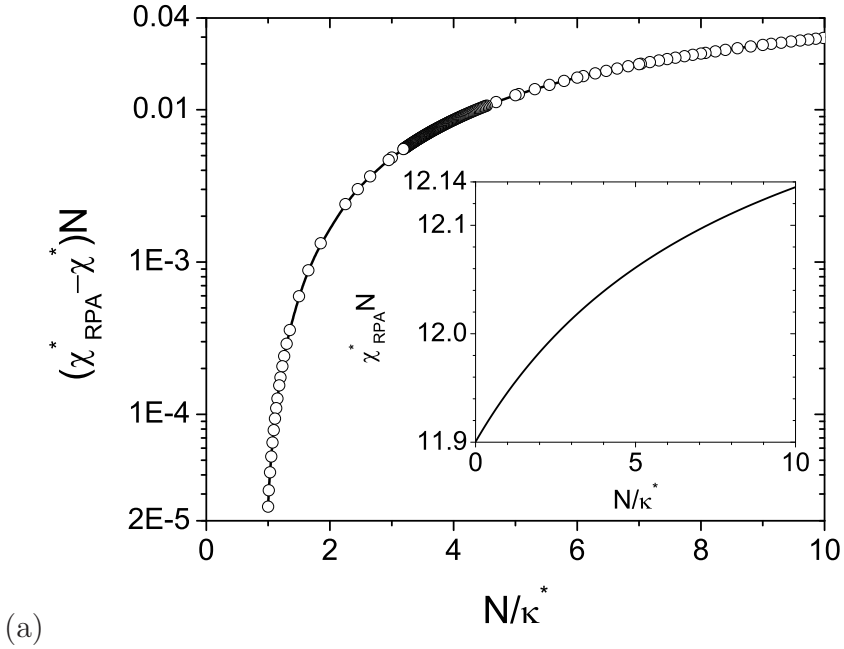

(a)

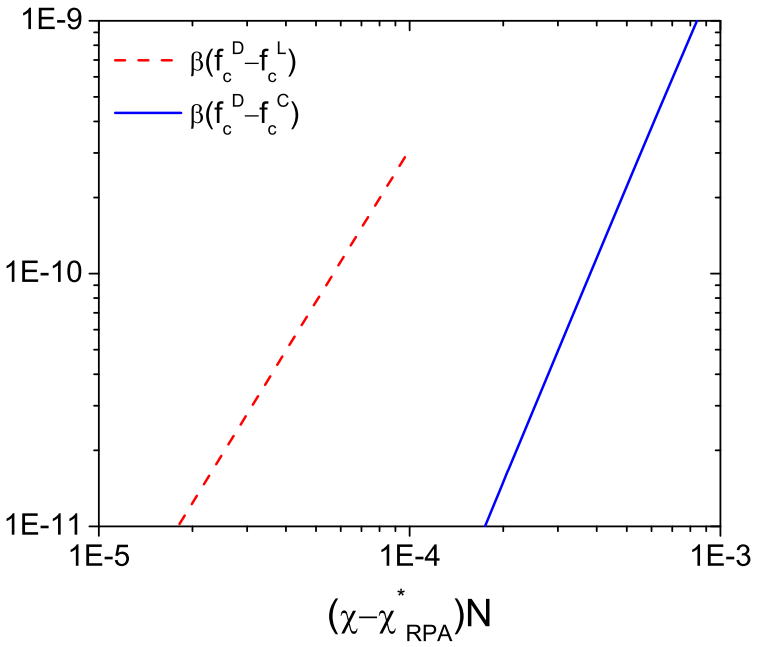

(b)

Figure 4.4: (a) $\chi^*_{\rm RPA}N$ vs. N/κ^* for $N = 10$, $f = 0.4$ and $\sigma/a = 2/\sqrt{3}$. (b) Difference of βf_c between D and an ordered phase (L or C) as a function of $(\chi - \chi^*_{\rm RPA})N$ at $N/\kappa = 0$.

density (thus have the same Helmholtz free energy per chain); in the second method, two co-existing phases have the same pressure and chemical potential (thus have the same Gibbs free energies per chain).

We use FOMC to study the phase transition between disordered and lamellar phases for two case, where in Case I $N/\kappa^* = 0$, and in Case II $N/\kappa^* = 50$. The ODT results obtained in the first method (in nVT ensemble) are given in Chapter 2, and we give the results obtained in second method (in nPT ensemble) in this chapter. Comparing the results of Cases I and II, we conclude that the difference between the ODT determined using these two methods is small and decreases with increasing N/κ^*. This justifies the underlying assumption that the disordered and lamellar phases at equilibrium have the same ρ_c used in Chapters 2 and 3.

We use SCF to study the phase transition between disordered and cylindrical phases. In the first method, we obtain the ODT curve of $\chi^* N$ vs. N/κ^*; the region above this curve is the cylindrical phase, and below this curve is the disordered phase. In the second method, we obtain two curves $\chi^{\mathrm{O}} N$ vs. N/κ^{O} and $\chi^{\mathrm{D}} N$ vs. N/κ^{D}; the region above the curve of $\chi^{\mathrm{O}} N$ vs. N/κ^{O} is the cylindrical phase, below the curve of $\chi^{\mathrm{D}} N$ vs. N/κ^{D} is the disordered phase, and between these two curves is where two phases co-exist. We find that the curve of $\chi^* N$ vs. N/κ^* lies in-between those two curves obtained in the second method. Finally, we find, in SCF, that the phase transition between disordered and cylindrical phases changes from first-order to second-order when $N/\kappa = 0$.

REFERENCES

[1] L. Leibler, Macromolecules **13**, 1602 (1980).

[2] G. H. Fredrickson and E. Helfand, J. Chem. Phys. **87**, 697 (1987).

[3] H. Fried and K. Binder, J. Chem. Phys. **94**, 8349 (1991); A. Weyersberg and T. A. Vilgis, Phys. Rev. E **48**, 377 (1993); R. G. Larson, Mol. Simul. **13**, 321 (1994); *ibid.*, Macromolecules **27**, 4198 (1994); Y. Yang, J. Lu, D. Yan, and J. Ding, Macromol. Theory Simul. **3**, 731 (1994); T. Dotera and A. Hatano, J. Chem. Phys. **105**, 8413 (1996); G. S. Grest, M. Lacasse, K. Kremer, and A. M. Gupta, J. Chem. Phys. **105**, 10583 (1996); A. Hoffmann, J. Sommer, and A. Blumen, J. Chem. Phys. **106**, 6709 (1997); *ibid.* **107**, 7559 (1997); T. Pakula, K. Karatasos, S. H. Anastasiadis, and G. Fytas, Macromolecules **30**, 8463 (1997); M. Murat, G. S. Grest, and K. Kremer, Macromolecules **32**, 595 (1999); A. J. Schultz, C. K. Hall, and J. Genzer, J. Chem. Phys. **117**, 10329 (2002); J. Yang, M. A. Winnik, and T. Pakula, Macromol. Theory Simul. **14**, 9 (2005); M. W. Matsen, G. H. Griffiths, R. A. Wickham, and O. N. Vassiliev, J. Chem. Phys. **124**, 024904 (2006).

[4] O. N. Vassiliev and M. W. Matsen, J. Chem. Phys. **118**, 7700 (2003).

[5] E. M. Lennon, K. Katsov, and G. H. Fredrickson, Phys. Rev. Lett. **101**, 138302 (2008).

[6] M. Muller and K. C. Daoulas, J. Chem. Phys. **128**, 024903 (2008).

[7] F. A. Detcheverry, D. Q. Pike, P. F. Nealey, M. Muller, and J. J. de Pablo, Phys. Rev. Lett. **102**, 197801 (2009); D. Q. Pike, F. A. Detcheverry, M. Muller, and J. J. de Pablo, J. Chem. Phys. **131**, 084903 (2009).

[8] T. M. Beardsley and M. W. Matsen, Eur. Phys. J. E **32**, 255 (2010).

[9] P. Sandhu, J. Zong, D. Yang, and Q. Wang, J. Chem. Phys. **138**, 194904 (2013).

[10] J. Zong and Q. Wang, J. Chem. Phys. **139**, 124907 (2013).

[11] P. Stasiak and M. W. Matsen, Macromolecules **46**, 8037 (2013).

[12] J. Glaser, P. Medapuram, T. M. Beardsley, M. W. Matsen, and D. C. Morse, Phys. Rev. Lett. **113**, 068302 (2014).

[13] P. Medapuram, J. Glaser, and D. C. Morse, Macromolecules **48**, 819 (2015).

[14] Q. Wang, J. Chem. Phys. **129**, 054904 (2008).

[15] Q. Wang and Y. Yin, J. Chem. Phys. **130**, 104903 (2009).

[16] M. W. Matsen and M. Schick, Phys. Rev. Lett. **72**, 2660 (1994); C. A. Tyler and D. C. Morse, *ibid.* **94**, 208302 (2005).

[17] G. H. Fredrickson, The Equilibrium Theory of Inhomogeneous Polymers, Oxford University Press, 2006.

[18] P. Zhang, D. Yang, and Q. Wang, J. Phys. Chem. B **118**, 12059 (2014).

[19] H. Kasten and B. Stuhn, Macromolecules **28**, 4777 (1995); D. H. Hajduk, S. M. Gruner, S. Erramilli, R. A. Register, and L. J. Fetters, Macromolecules **29**, 1473 (1996); B. Steinhoff, M. Rullmann, M. Wenzel, M. Junker, I. Alig, R. Oser, B. Stuhn, G. Meier, O. Diat, P. Bosecke, and H. B. Stanley, Macromolecules **31**, 36 (1998).

[20] P. J. Hoogerbrugge and J. M. V. A. Koelman, Europhys. Lett. **19**, 155 (1992).

[21] E. Helfand and Y. Tagami, J. Polym. Sci., Part B: Polym. Lett. **9**, 741 (1971).

[22] R. D. Groot and T. J. Madden, J. Chem. Phys. **108**, 8713 (1998).

[23] N. C. Ekdawi-Sever, P. B. Conrad, and J. J. de Pablo, J. Phys. Chem. A **105**, 734 (2001); T. Okabe, M. Kawata, Y. Okamoto, and M. Mikami, Chem. Phys. Lett. **335**, 435 (2001); T. Kristof and J. Liszi, Mol. Phys. **99**, 167 (2001).

[24] A. M. Ferrenberg and R. H. Swendsen, Phys. Rev. Lett. **63**, 1195 (1989).

[25] J. D. Chodera,W. C. Swope, J.W. Pitera, C. Seok, and K. A. Dill, J. Chem. Theory Comput. **3**, 26 (2007).

[26] M. Muller and N. B. Wilding, Phys. Rev. E **51**, 2079 (1995).

[27] J. Zong, X. Zhang, and Q. Wang, J. Chem. Phys. **137**, 134904 (2012).

[28] E. Helfand and Y. Tagami, J. Chem. Phys. **56**, 3592 (1972).

CHAPTER 5

ISOTROPIC-NEMATIC TRANSITION OF SOFT-CORE SPHEROCYLINDERS

5.1 Introduction

Fast Monte Carlo simulations have recently attracted great interest in the study of polymeric systems.[1,2] In this chapter, we explore the use of anisotropic soft-core potentials that can lead to liquid-crystalline phases in fast off-lattice Monte Carlo simulations, with future applications to the study of rod-coil block copolymers.[3]

The use of soft-core potentials for liquid crystal only began several years ago. Vink and Schilling studied in a grand-canonical ensemble a soft-core spherocylinder model given by $\beta u(d_{\min}) = \epsilon \geq 0$ if the minimum distance $d_{\min}$ between two line segments representing spherocylinders[4] is less than the spherocylinder diameter D and 0 otherwise; they determined the isotropic-nematic transition (INT) of this model as a function of the spherocylinder aspect ratio L/D for $\epsilon = 2$.[5] They also demonstrated the great advantage of using soft-core potentials in estimating the isotropic-nematic interfacial tension.[5,6] Wilson and co-workers studied in an isothermal-isobaric ensemble three soft-core variants of the soft repulsive spherocylinder potential,[7] all of which depend on $d_{\min}$ similar to the above model.[8] While these four soft-core potentials all recover the standard model of hard spherocylinders[9] for liquid crystals as the repulsion strength $\epsilon \to \infty$, they do not take into account the degree of overlap between two spherocylinders. The same problem exists for another soft-core spherocylinder potential recently proposed by Lintuvuori and Wilson, although partially elevated by an orientation-dependent attraction between two spherocylinders;[10] INT of this model was studied by these authors using statistical temperature molecular dynamics.[11]

Going beyond spherocylinders, Prestipino and Saija proposed the Gaussian-core nematic model and explored its phase diagram at both zero and finite temperatures;[12] the zeor-temperature phase diagram was recently studied by Nikoubashman and Likos.[13] Zannoni and co-workers proposed a soft-core Gay-Berne potential by modifying the repulsive part of the standard Gay-Berne potential,[14] and explored the phase diagrams of uniaxial and biaxial ellipsoidal particles interacting with this potential.[15]

Finally, we would like to mention that, while dissipative particle dynamics simulations[16] using isotropic soft-core potentials have been applied to the study of liquid-crystalline phases as first reported by AlSunaidi et al.,[17] a mesogenic unit in such simulations is usually represented by a rigid (linear)[17] or semiflexible[18] chain of several spherical particles. This is not very computationally efficient because the simulation time is proportional to at least the square of particle number. To the best of our knowledge, the only exception was reported by Purton and Smith, who performed pilot dissipative particle dynamics study using a Gaussian density model for non-spherical particles suitable for both uniaxial and biaxial liquid crystals.[19]

In this work, we propose a novel anisotropic soft-core potential for spherocylinders, demonstrate its advantage and application to the study of INT, and compare fast off-lattice Monte Carlo simulation results with virial expansion predictions.

5.2 Model and Methods

5.2.1 Two models of soft-core spherocylinders

We study two models in this work. In Model A, we use a pair potential given by

$$\beta u_{\mathrm{A}}(d_{\min}) = \begin{cases} \epsilon \geq 0 & \text{if } d_{\min} < D \\ 0 & \text{otherwise} \end{cases}, \tag{5.1}$$

where $\beta = 1/k_B T$ with k_B being the Boltzmann constant and T the thermodynamic temperature, D is the diameter of spherocylinders, $d_{\min}$ is the minimum distance between two line segments representing spherocylinders,[4] and ϵ is the repulsion strength.

While Model A uses a simple anisotropic soft-core pair potential, it does not take into account the degree of overlap between two spherocylinders. To overcome this drawback, we propose Model B, which includes all point-point interactions between two line segments (spherocylinders) 1 and 2 and is given by

$$\beta u_{\mathrm{B}}(\mathbf{r}_1 - \mathbf{r}_2, \mathbf{u}_1, \mathbf{u}_2, L) = \epsilon \int_{-1/2}^{1/2} \mathrm{d}t_1 \int_{-1/2}^{1/2} \mathrm{d}t_2 v(|\mathbf{r}_1 + t_1 L\mathbf{u}_1 - \mathbf{r}_2 - t_2 L\mathbf{u}_2|), \tag{5.2}$$

where L is length of the line segments, $\mathbf{r}_i$ ($i = 1$ and 2) is the spatial position of the mid-point of line segment i, $\mathbf{u}_i$ is a unit vector denoting the orientation of line segment i, and the integrations over t_1 and t_2 include the repulsion between all pairs of points (one on each line segment) via a step-function-like isotropic pair potential v depending on the distance d between the two points

$$v(d) = \begin{cases} 1 & \text{if } d < D \\ 0 & \text{otherwise} \end{cases} .$$

Note that βu_{B} can be evaluated analytically and thus efficiently. We also note that, in the limit of $\epsilon \to \infty$, both Model A and B recover the standard model of hard spherocylinders[9] for liquid crystals.

5.2.2 Fast off-lattice Monte Carlo simulations

Our simulations are performed in an isothermal-isobaric (nPT) ensemble using a cubic simulation box with periodic boundary conditions in all directions. Trial moves include random displacement and rotation of spherocylinders, and volume change of the simulation box; for the latter, the new volume is generated as $V_{\mathrm{new}} = V_{\mathrm{old}} \exp(\xi)$, where V_{old} is the current volume and ξ a random number uniformly distributed within $(-\xi_{\max}, \xi_{\max})$. These three types of trial moves occur with a probability of 0.5, 0.496 and 0.004, respectively, and their acceptance rates are about 50% achieved by adjusting the maximum displacement at the beginning of equilibration. To meet the minimum image convention for spherocylinders,[20] we require the length of our simulation box $L_b > 2L + 4D$. Similar to the work of Vink and Schilling,[5] we use a cell structure to save simulation time.

To improve sampling efficiency, we use the replica exchange (RE) at different pressures,[21] which greatly reduces the sample correlation length. The acceptance criterion for swapping two configurations i and j at pressure P_i and P_j, respectively, is $P_{\rm acc} = \min\{1, \exp[\beta(P_i - P_j)(V_i - V_j)]\}$, where V_i and V_j denote the corresponding volume.

We also use the multiple histogram reweighting (HR) technique[22] to analyze simulation results. For totally R simulation runs performed at the same ϵ but different pressures P_i $(i = 1, \ldots, R)$, we collect the histogram $H_i(E, V, S)$ at each pressure P_i, where E denotes the system energy, and S is the orientational order parameter defined as the largest eigenvalue of the orientational tensor $\mathbf{Q} = \sum_{i=1}^{n}(3\mathbf{u}_i\mathbf{u}_i - \mathbf{I})/2n$ with n being the number of spherocylinders in the box and $\mathbf{I}$ the identity matrix. The probability for the system having E, V and S at pressure P is then given by

$$p_b(E, V, S|P) = \frac{\sum_{i=1}^{R} g_i^{-1} H_i(E, V, S) \exp[\beta(E + PV)]}{\sum_{j=1}^{R} g_j^{-1} M_j H_j(E, V, S) \exp[\beta(E + P_j V) - C_j]},$$

where g_j is the statistical inefficiency of the collected V in the $j^{\rm th}$ run, M_j is the total number of collected samples after equilibration in the $j^{\rm th}$ run, and $C_j = \sum_E \sum_V \sum_S p_b(E, V, S|P_j)$; note that $\exp(C_j)$ is proportional to the nPT-ensemble partition function at P_j.[23]

In this work, we simulate $n = 700$ soft-core spherocylinders with the aspect ratio $L/D = 7$ at several ϵ-values. The initial configuration of each run is randomly generated. Before RE is performed, we run several nPT simulations to determine the pressure range of INT. Once the range is roughly determined for a given ϵ, we use $R = 10 \sim 15$ with RE attempted every 10 Monte Carlo steps (MCS), where one MCS is defined as on average one trial move for every particle in the system; this gives an acceptance rate of about $60 \sim 85\%$. We use $2 \sim 4 \times 10^6$ MCS for equilibration and collect samples every 10 MCS for the subsequent $8 \sim 10 \times 10^6$ MCS.

5.2.3 Virial expansion

Here we denote the director of the nematic phase as the z axis. The orientation of a spherocylinder can then be expressed as $\mathbf{u} = (\theta, \varphi)$, where θ is the angle between $\mathbf{u}$ and the z

axis, and φ is the longitudinal angle; note that $\int \mathrm{d}\mathbf{u} = -\int_0^{2\pi} \mathrm{d}\varphi \int_{\theta=0}^{\theta=\pi} \mathrm{d}\cos\theta$. We further introduce the orientation distribution function $\phi(\mathbf{u})$ that satisfies

$$\int \phi(\mathbf{u})\mathrm{d}\mathbf{u} = 1; \tag{5.3}$$

$(n/V)\phi(\mathbf{u})\mathrm{d}\mathbf{u}$ gives the number of spherocylinders in the system having an orientation between $\mathbf{u}$ and $\mathbf{u} + \mathrm{d}\mathbf{u}$.

For both the isotropic (I) and nematic (N) phases, we can write $\phi(\mathbf{u}) = \phi(\theta)$. After the virial expansion analogous to Onsager's work,[9] the Helmholtz free energy of the system becomes

$$\begin{aligned}\beta\mathcal{F} = \frac{\pi n^2}{V}\int_{\theta=0}^{\theta=\pi} \mathrm{d}\cos\theta \int_{\theta'=0}^{\theta'=\pi} \mathrm{d}\cos\theta' \phi(\theta) V_2(\theta,\theta')\phi(\theta') \\ -2\pi n \int_{\theta=0}^{\theta=\pi} \mathrm{d}\cos\theta \phi(\theta)\ln\phi(\theta) + n\ln\frac{n}{V} - n,\end{aligned} \tag{5.4}$$

where

$$V_2(\theta,\theta') \equiv \int_0^{2\pi} \mathrm{d}(\varphi-\varphi') \int \mathrm{d}(\mathbf{r}-\mathbf{r}') \left\{1 - \exp\left[-\beta u_{\mathrm{A(B)}}(\mathbf{r}-\mathbf{r}', \mathbf{u}, \mathbf{u}', L)\right]\right\}.$$

Note that for Model A we have

$$V_2(\theta,\theta') = [1-\exp(-\epsilon)] \int_0^{2\pi} \mathrm{d}(\varphi-\varphi') \left(\frac{4\pi}{3}D^3 + 2\pi L D^2 + 2L^2 D|\mathbf{u}\times\mathbf{u}'|\right), \tag{5.5}$$

where $|\mathbf{u}\times\mathbf{u}'| = \sin\gamma$ with γ being the angle between $\mathbf{u}$ and $\mathbf{u}'$ and $\cos\gamma = \sin\theta\sin\theta'\cos(\varphi-\varphi') + \cos\theta\cos\theta'$. In Appendix A, we derive an approximate correspondence between the virial expansion of Model A and the commonly used Maier-Saupe interaction.[24] In the limit of $L\to\infty$, we also note that for Model B we have

$$\frac{V_2(\theta,\theta')}{L^2} = 2D\int_0^{2\pi} \mathrm{d}(\varphi-\varphi')\sin\gamma \left\{1 - \int_0^D \mathrm{d}d_{\min} \exp\left[-\frac{\pi\epsilon\,(D^2 - d_{\min}^2)}{\sin\gamma}\right]\right\}.$$

Clearly, for the isotropic phase $\phi_{\mathrm{I}}(\theta) = 1/4\pi$, and for the nematic phase $\phi_{\mathrm{N}}(\theta)$ is obtained by minimizing $\mathcal{F}$, i.e., setting $\delta\beta\mathcal{F}/\delta\phi(\theta) = 0$. Also, the phase equilibrium equations for INT are obtained by equating the pressures and chemical potentials of the two phases,

$P \equiv -(\partial \mathcal{F}/\partial V)_{n,T}$ and $\mu \equiv (\partial \mathcal{F}/\partial n)_{V,T}$. These, along with Eq. (5.3), give

$$\begin{aligned}
\frac{a}{16\pi}\rho_{\mathrm{I}}^2 + \rho_{\mathrm{I}} &= \pi b \rho_{\mathrm{N}}^2 + \rho_{\mathrm{N}}, \\
\frac{a}{8\pi}\rho_{\mathrm{I}} + \ln\frac{\rho_{\mathrm{I}}}{4\pi} &= 2\pi b \rho_{\mathrm{N}} - 2\pi \int_{\theta=0}^{\theta=\pi} \mathrm{d}\cos\theta \phi_{\mathrm{N}}(\theta) \ln \phi_{\mathrm{N}}(\theta) + \ln \rho_{\mathrm{N}}, \\
\phi_{\mathrm{N}}(\theta) &= -\frac{\exp\left[-\rho_{\mathrm{N}} c(\theta)\right]}{2\pi \int_{\theta=0}^{\theta=\pi} \mathrm{d}\cos\theta \exp\left[-\rho_{\mathrm{N}} c(\theta)\right]},
\end{aligned}$$

where $\rho_{\mathrm{I(N)}} \equiv D^3 n / V_{\mathrm{I(N)}}$ is the dimensionless number density of spherocylinders in the co-existing isotropic (nematic) phase, and

$$\begin{aligned}
a &\equiv \int_{\theta=0}^{\theta=\pi} \mathrm{d}\cos\theta \int_{\theta'=0}^{\theta'=\pi} \mathrm{d}\cos\theta' \frac{V_2(\theta,\theta')}{D^3}, \\
b &\equiv -\int_{\theta=0}^{\theta=\pi} \mathrm{d}\cos\theta \phi_{\mathrm{N}}(\theta) c(\theta), \\
c(\theta) &\equiv -\int_{\theta'=0}^{\theta'=\pi} \mathrm{d}\cos\theta' \phi_{\mathrm{N}}(\theta') \frac{V_2(\theta,\theta')}{D^3}.
\end{aligned}$$

Solving these equations gives ρ_{I}, ρ_{N}, and $\phi_{\mathrm{N}}(\theta)$ of the co-existing phases. From the latter we can further obtain the corresponding orientational order parameter $S_{\mathrm{N}} = -\pi \int_{\theta=0}^{\theta=\pi} \mathrm{d}\cos\theta (3\cos^2\theta - 1)\phi_{\mathrm{N}}(\theta)$. Finally, we note that for Model A $[1 - \exp(-\epsilon)]\rho_{\mathrm{I(N)}}$ and $\phi_{\mathrm{N}}(\theta)$ (thus S_{N}) depend only on L/D.

5.3 Results and Discussion

5.3.1 Advantage of Model B

To demonstrate the advantage of Model B over soft-core spherocylinder models depending only on $d_{\min}$ (e.g., Model A), we use a few particular examples here to compare the pair potentials of Model A and B with the actual overlapping volume V_0 between two spherocylinders; note that in general V_0 is unknown.

In the first example, we consider two spherocylinders having the same center (thus $d_{\min} = 0$) and an angle γ between their axes, as shown in the inset of Fig. 5.1(a); when $\gamma = 0$, the two spherocylinders completely overlap. Fig. 5.1(a) shows how u_{A}, u_{B} and V_0, each normalized by its value at $\gamma = \pi/2$, vary with γ. The vertical line in Fig. 5.1(a) marks the angle

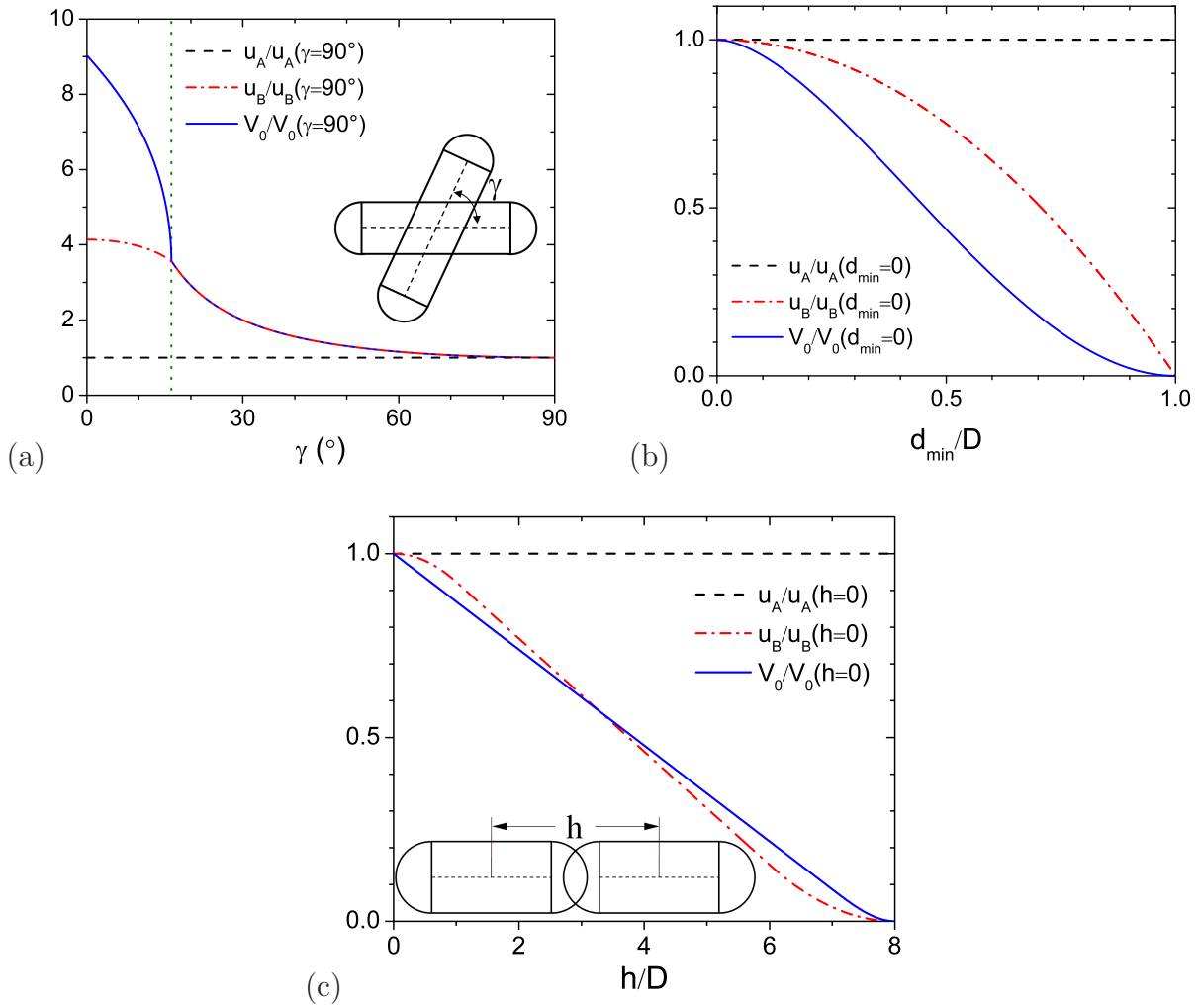

Figure 5.1: Comparison among the pair potential of Model A and B, $u_{\rm A}$ and $u_{\rm B}$, respectively, and the actual overlapping volume V_0 between two spherocylinders in three cases, where $L/D = 7$ is used. See main text for more details.

$\gamma_0 = 2\arcsin(1/\sqrt{1+(L/D)^2})$; for $\gamma > \gamma_0$, the hemispherical caps of the two spherocylinders do not overlap. We see that, while $u_{\rm A}$ is constant, $u_{\rm B}$ decreases with increasing γ in the same trend as V_0; for $\gamma \in [\gamma_0, \pi/2]$, we even find $u_{\rm B} \propto V_0$. In fact, the latter is the same as the case of two infinitely long cylinders, for which we have $\beta u_{\rm B} = \epsilon\pi D^2/\sin\gamma$ and $V_0 = 2D^3/3\sin\gamma$.

In the second example, we consider two spherocylinders having their centers separated by $d_{\rm min} \in (0, D)$ and an angle $\gamma \in [\gamma_0, \pi/2]$ between their axes, which are both perpendicular to the line connecting their centers; the $d_{\rm min} = 0$ case was just discussed above. Here we have $\beta u_{\rm B} = \epsilon\pi(D^2 - d_{\rm min}^2)/\sin\gamma$ and $V_0 =$

$4\int_{d_{\min}-D/2}^{D/2} \mathrm{d}t \sqrt{[(D/2)^2 - t^2]\,[(D/2)^2 - (d_{\min} - t)^2]} \Big/ \sin\gamma$; at given $d_{\min}$, we again find $u_{\mathrm{B}} \propto V_0$ regardless of γ. Fig. 5.1(b) shows how u_{A}, u_{B} and V_0, each normalized by its value at $d_{\min} = 0$, vary with $d_{\min}$. We see that u_{B} decreases with increasing $d_{\min} \in (0, D)$ in the same trend as V_0, while u_{A} is constant.

In the third example, we consider two spherocylinders with their axes on the same line and their centers of mass separated at distance h, as shown in the inset of Fig. 5.1(c). Fig. 5.1(c) shows how u_{A}, u_{B} and V_0, each normalized by its value at $h = 0$, vary with h. We see that, while u_{A} is constant for $h \in [0, L + D)$ (i.e., where the two spherocylinders overlap), u_{B} decreases with increasing $h \in [0, L + D)$ in the same trend as V_0. In particular, for $L/D > 2$, we have

$$V_0 = \begin{cases} \pi D^3/6 + \pi D^2(L - h)/4 & \text{for } 0 \le h \le L \\ \pi(h + 2D - L)(L + D - h)^2/12 & \text{for } L < h < L + D \end{cases}$$

and

$$\frac{\beta u_{\mathrm{B}}}{\epsilon} = \begin{cases} 2DL - D^2 - h^2 & \text{for } 0 \le h \le D \\ 2D(L - h) & \text{for } D < h \le L - D \\ (L + D - h)^2/2 & \text{for } L - D < h < L + D \end{cases} ;$$

note that $u_{\mathrm{B}} \propto V_0 - \pi D^3/6$ for $h \in [D, L-D)$, where the term $\pi D^3/6$ is due to the overlapping between the cylindrical body and the hemispherical cap of the two spherocylinders; clearly, the contribution of this term to V_0 becomes smaller with increasing L/D.

These examples demonstrate that our Model B is superior to soft-core spherocylinder models depending only on $d_{\min}$ (e.g., Model A) in that it takes into account the degree of overlap between two spherocylinders.

5.3.2 Sampling improvement of RE

Here we compare the sampling near INT of simulations with RE to that of nPT simulations without RE. Fig. 5.2 shows the statistical inefficiency[23] of the orientational order parameter, g_S, as a function of the dimensionless pressure, $\beta D^3 P$, for Model B with $\epsilon = 2$. In this

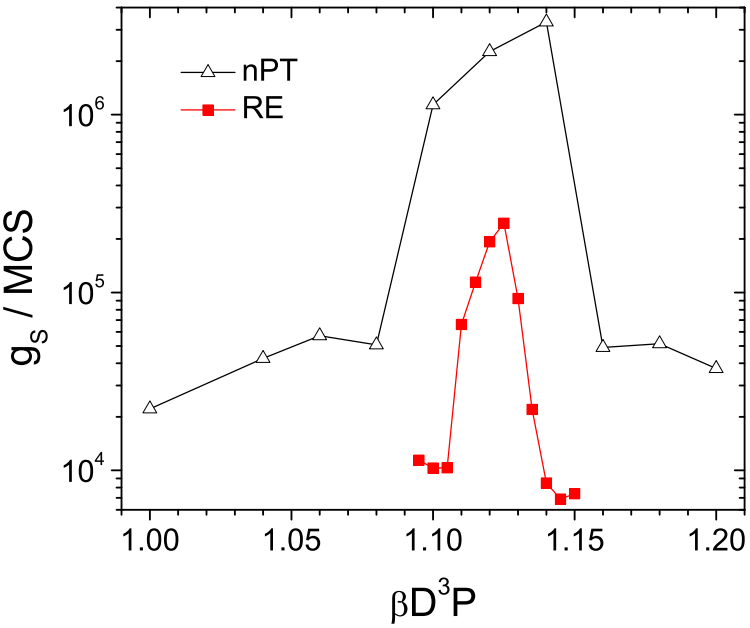

Figure 5.2: Statistical inefficiency of the orientational order parameter g_S in RE and nPT simulations (without RE) as a function of the dimensionless pressure $\beta D^3 P$ for Model B with $L/D = 7$ and $\epsilon = 2$.

semi-logarithmic plot, we see that g_S greatly increases in the transition region and that RE reduces g_S by at least an order of magnitude. Similar results are also found for Model A and thus not shown. Another benefit of using RE is that it can be combined with HR to accurately locate the phase transition point, as both techniques require the overlap of histograms obtained in different runs.

5.3.3 Equation of states and fluctuations

Fig. 5.3(a) shows how the ensemble average of the system dimensionless density $\rho \equiv D^3 n/V$, $\langle \rho \rangle$, varies with the pressure $\beta D^3 P$ for Model B with $\epsilon = 2$. For the simulation results, the sharp increase of $\langle \rho \rangle$ over a small range of pressure indicates INT, which is more clearly seen from the results of the orientational order parameter $\langle S \rangle$ shown in Fig. 5.3(b). In the thermodynamic limit (i.e., an infinitely large system), both $\langle \rho \rangle$ and $\langle S \rangle$ exhibit a discontinuity at the transition similar to the VE results. On the other hand, while we see qualitative

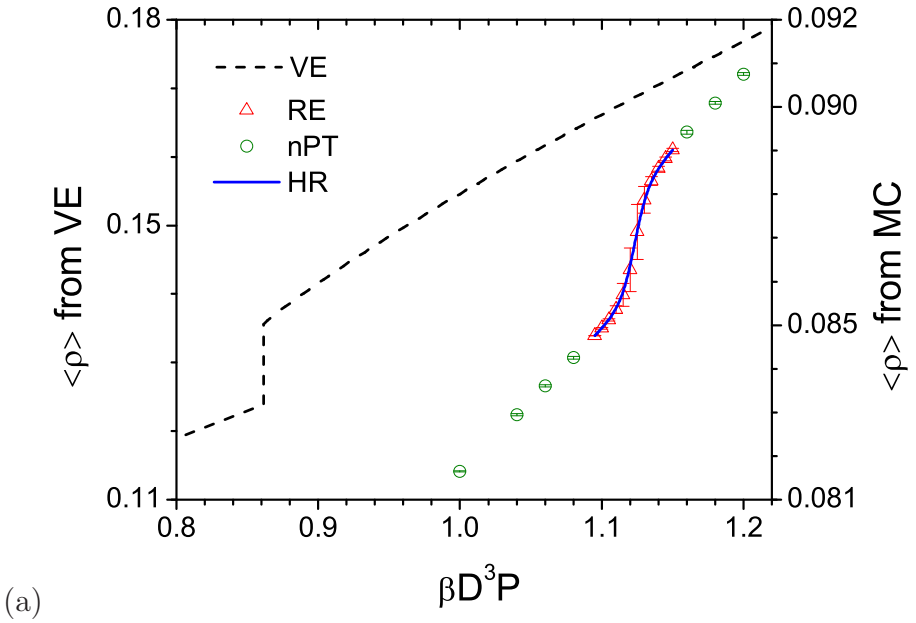

(a)

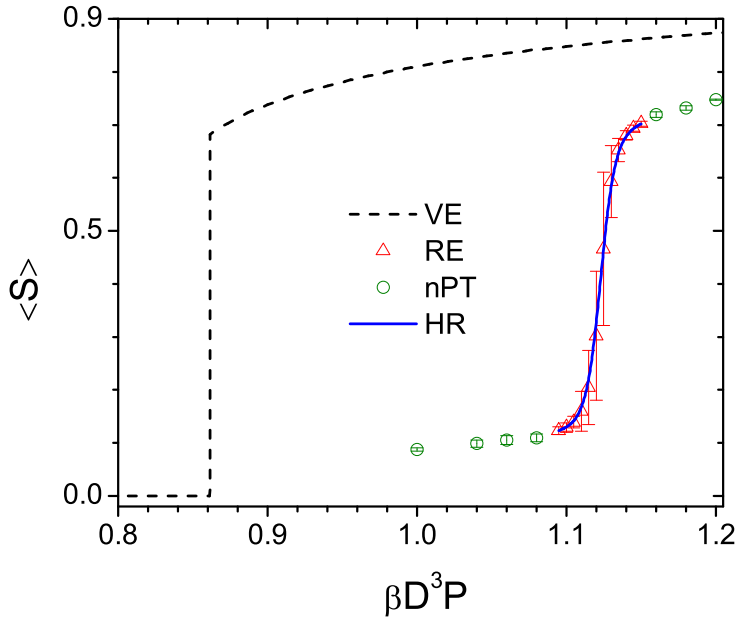

(b)

Figure 5.3: (a) Ensemble average of the dimensionless density $\langle\rho\rangle$ and (b) that of the orientational order parameter $\langle S\rangle$ as functions of pressure for Model B with $L/D = 7$ and $\epsilon = 2$.

agreement between VE and simulation results, VE underestimates the phase transition pressure and overestimates $\langle\rho\rangle$ and $\langle S\rangle$ (for the nematic phase) at all pressures. This is mainly because only the first-order terms are included in VE with all higher-order terms neglected. Similar results are found for Model A and thus not shown.

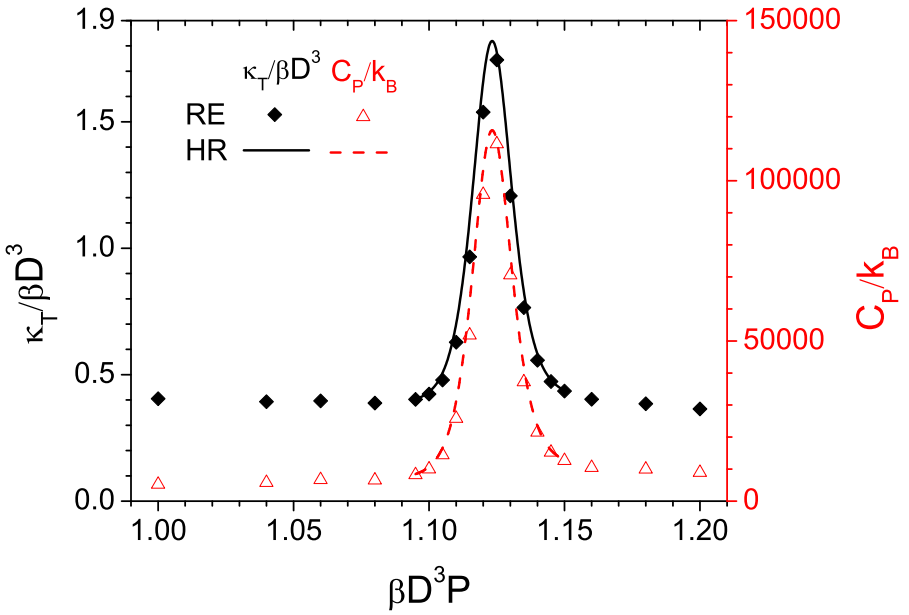

Figure 5.4: Isothermal compressibility κ_T and constant-pressure heat capacity C_P as functions of pressure for Model B with $L/D = 7$ and $\epsilon = 2$.

We also calculate the isothermal compressibility κ_T and constant-pressure heat capacity C_P in our simulations, given by

$$\frac{\kappa_T}{\beta D^3} = \frac{\langle V^2 \rangle - \langle V \rangle^2}{\langle V \rangle \, D^3}$$

and

$$\frac{C_P}{k_B} = \left\langle (\beta E + \beta P V)^2 \right\rangle - \left\langle \beta E + \beta P V \right\rangle^2 .$$

Fig. 5.4 shows how these dimensionless quantities vary with $\beta D^3 P$ for Model B with $\epsilon = 2$. Both quantities exhibit a sharp peak around INT, indicating its first-order nature. We find that both maxima occur at $\beta D^3 P = 1.123$, consistent with the transition point $\beta D^3 P^* = 1.123 \pm 0.005$ determined at this ϵ-value by the equal-weight criterion[25] explained in detail below. In the thermodynamic limit, both κ_T and C_P diverge at the transition.

5.3.4 Phase diagrams

Using HR, we can interpolate with minimal error the simulation data at any pressure within the pressure range of our simulations at given ϵ. Since we are interested in both ρ and S,

we calculate the normalized two-dimensional histogram $p_b(\rho, S|P)$ at given P as shown in Fig. 5.5(a). We then determine the transition pressure P^* from the equal-weight criterion[25]

$$\int_0^{\langle S\rangle(P^*)} \mathrm{d}S \sum_\rho p_b(\rho, S|P^*) = \int_{\langle S\rangle(P^*)}^1 \mathrm{d}S \sum_\rho p_b(\rho, S|P^*).$$

At P^*, all samples with $S < \langle S\rangle\,(P^*)$ are considered as the isotropic phase, and the rest are considered as the nematic phase; averaging over the nematic phase then gives S_N, and the ensemble averaged co-existing densities of the two phases, ρ_I and ρ_N, are similarly determined. To estimate the statistical errors of P^*, S_N, ρ_I and ρ_N, we calculate these quantities using the first- and second-half of our samples collected after equilibration, respectively, then take three times their largest deviation from the corresponding value determined using all the samples as the error bar. Fig. 5.5(b) shows the re-weighted histogram of the system density $p_b(\rho|P^*) = \int_0^1 p_b(\rho, S|P^*)\mathrm{d}S$, and those for the isotropic and nematic phase, $p_{b,\mathrm{I}}(\rho|P^*) = \int_0^{\langle S\rangle(P^*)} p_b(\rho, S|P^*)\mathrm{d}S$ and $p_{b,\mathrm{N}}(\rho|P^*) = \int_{\langle S\rangle(P^*)}^1 p_b(\rho, S|P^*)\mathrm{d}S$, respectively; we see that the double peak in $p_b(\rho|P^*)$ are well separated.

Collecting all the data for INT at various ϵ-values, we construct phase diagrams for the two models as shown in Figs. 5.6(a) and 5.6(b), respectively. In each figure, the area above ρ_N is the nematic phase, the area under ρ_I is the isotropic phase, and the area between them is the two-phase region. We also compare VE and simulation results in Fig. 5.6. First, as $\epsilon \to \infty$ (i.e., $\epsilon/(\epsilon+2) = 1$), VE results of both models recover those for hard spherocylinders, and the co-exiting densities obtained from our simulations are also in good agreement with those of Bolhuis and Frenkel.[20] Second, VE and simulation results exhibit qualitatively the same behavior. We see ρ_I and ρ_N increase with decreasing ϵ for both models, which means INT still occurs at high enough densities even for small ϵ. In fact, at fixed L/D, VE gives constant $[1 - \exp(-\epsilon)]\rho_{\mathrm{I(N)}}$ for Model A and $\rho_{\mathrm{I(N)}} \propto \epsilon^{-2}$ at small ϵ for Model B. On the other hand, at large ϵ, ρ_I and ρ_N for Model A are almost independent of ϵ, while those for Model B still decrease with increasing ϵ. This means Model B is "softer" than Model A. For quantitative comparison, however, VE largely overestimates ρ_I, ρ_N and $\rho_\mathrm{N} - \rho_\mathrm{I}$ for both models.

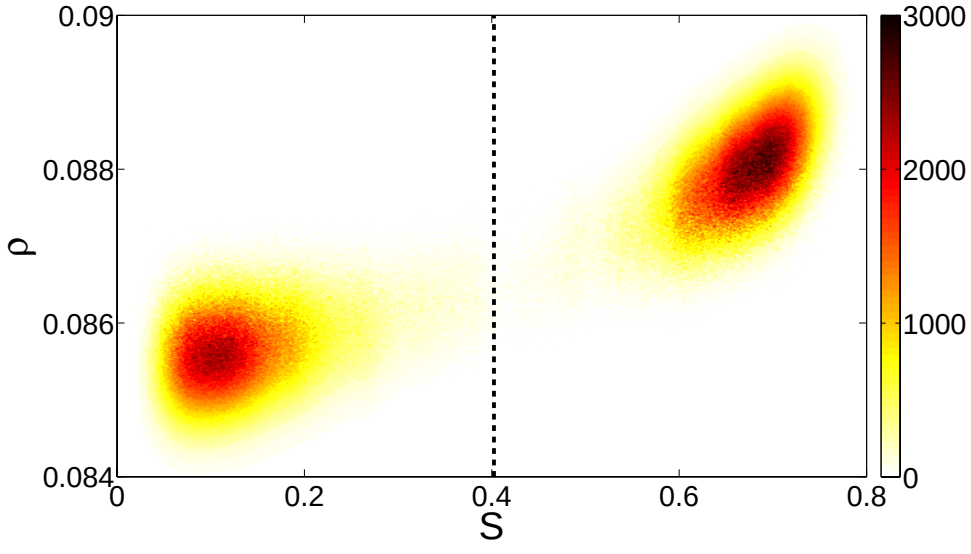

(a)

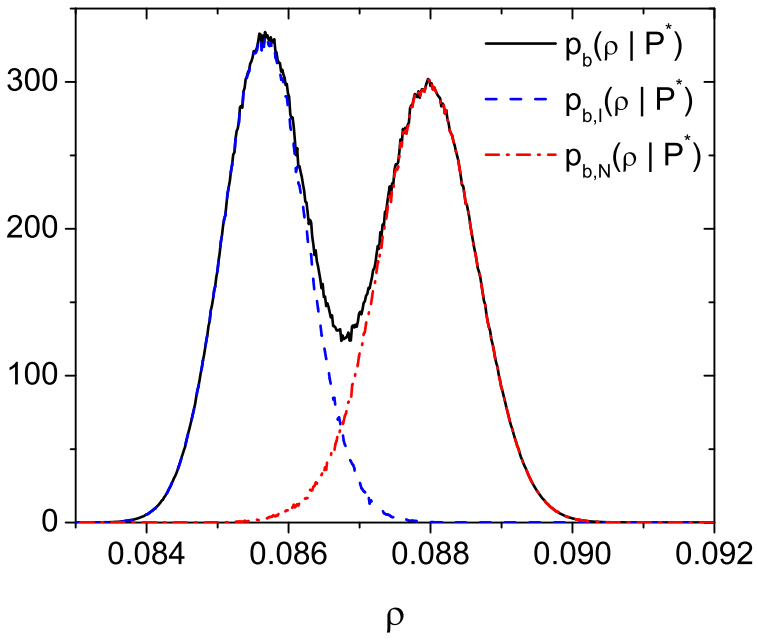

(b)

Figure 5.5: Re-weighted (a) two-dimensional histogram $p_b(\rho, S|P^*)$ and (b) one-dimensional histograms $p_b(\rho|P^*)$, $p_{b,\mathrm{I}}(\rho|P^*)$ and $p_{b,\mathrm{N}}(\rho|P^*)$ at the transition pressure $\beta D^3 P^* = 1.123$ for Model B with $L/D = 7$ and $\epsilon = 2$. The vertical line in (a) marks $\langle S \rangle$ (P^*).

Fig. 5.6 also shows the orientational order parameter S_{N} of the co-existing nematic phase. VE predicts that S_{N} is independent of ϵ for Model A and varies slightly with $\epsilon \geq 2$ for Model B; while these are in qualitative agreement with our simulation results, VE somewhat overestimates S_{N} for both models (within the range of our ϵ-values). Fig. 5.7 shows how the

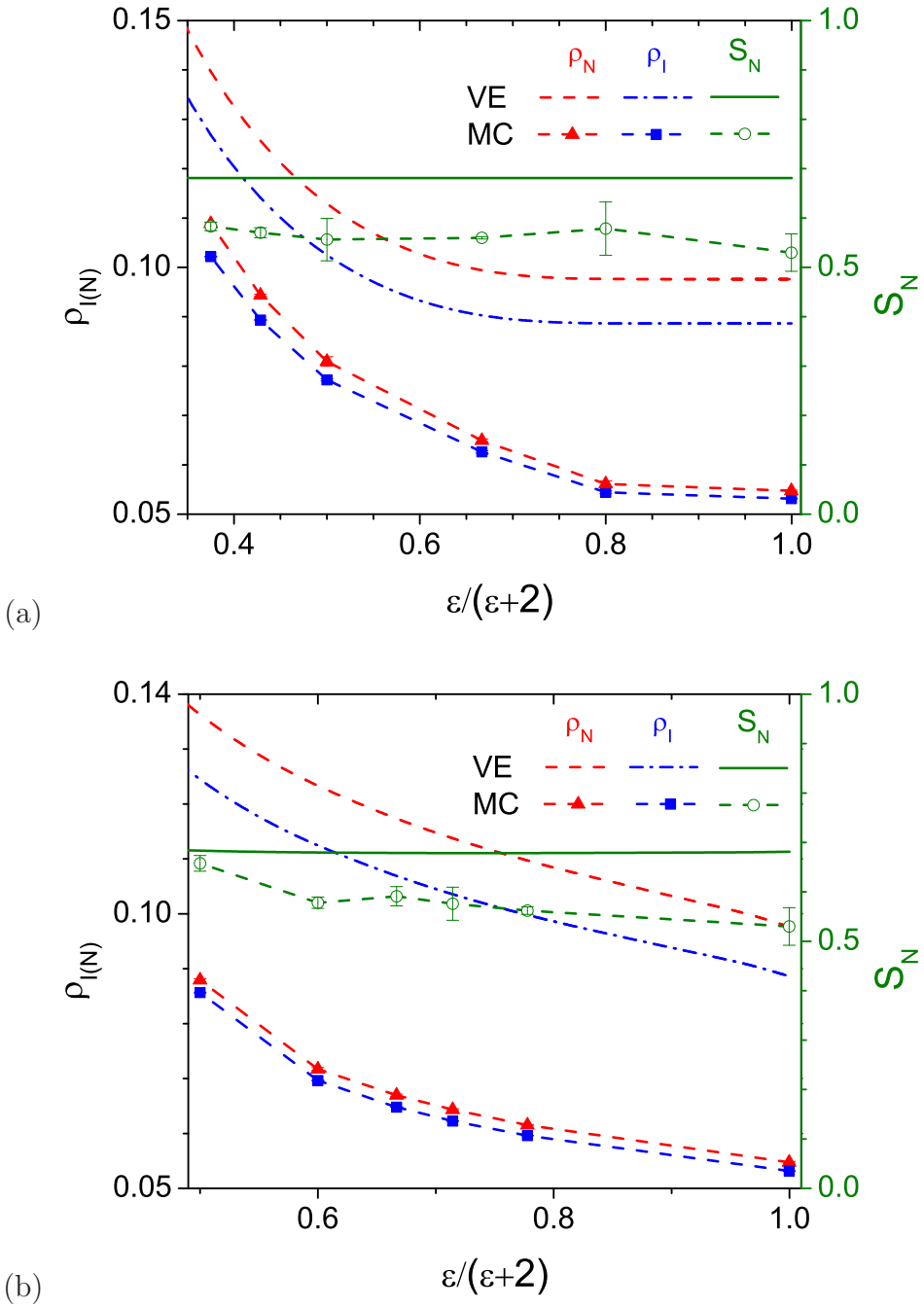

Figure 5.6: Phase diagram and S_{N} for (a) Model A and (b) Model B with $L/D = 7$.

transition pressure P^* varies with ϵ for the two models. Consistent with the above result that Model B is "softer" (thus has higher P^*) than Model A, we see that, at large ϵ, P^* is almost independent of ϵ for Model A but still decreases with increasing ϵ for Model B. While we again see qualitative agreement between VE and simulation results, VE overestimates P^*

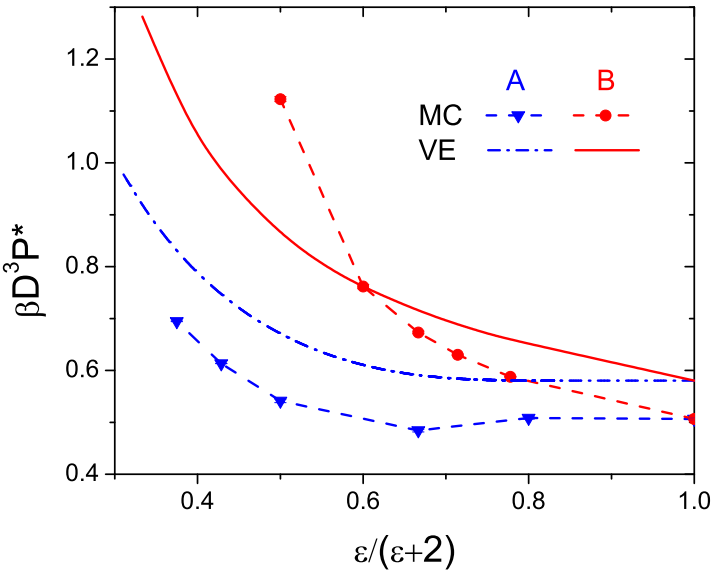

Figure 5.7: Transition pressure $\beta D^3 P^*$ for Model A and B with $L/D = 7$.

both for Model A and at $\epsilon > 3$ for Model B; that VE underestimates P^* at $\epsilon = 2$ for Model B is also shown in Fig. 5.3(a) above.

While we use $L/D = 7$ here, Vink and Schilling performed simulations for Model A with $\epsilon = 2$ and various L/D;[5] we therefore compare in Fig. 5.8 the phase diagrams from VE and simulations for that case, where the simulation results are taken from Ref. [5]. Since for $\epsilon > 0$ both $\rho_{\rm I}$ and $\rho_{\rm N}$ vanish in the limit of $L/D \to \infty$ (VE predicts $\rho_{\rm I(N)} \propto (L/D)^{-2}$ at large L/D), we plot $(L/D)^2 \rho_{\rm I(N)}$ vs. D/L here. Consistent with our results shown in Fig. 5.6, we see that VE overestimates $\rho_{\rm I}$, $\rho_{\rm N}$ and $\rho_{\rm N} - \rho_{\rm I}$ for $L/D \leq 25$; note that the statistical errors of their simulations were not estimated for $L/D \geq 30$.[5] We also see that, while both VE and simulations give decreasing $(L/D)^2 \rho_{\rm N}$ with increasing D/L, opposite trends are found for $(L/D)^2 \rho_{\rm I}$. Note that both VE and simulations give increasing $\rho_{\rm N} - \rho_{\rm I}$ with increasing D/L in the same trend as $\rho_{\rm I}$ and $\rho_{\rm N}$ (data not shown). We further see that the VE predictions become more accurate with decreasing D/L, consistent with Frenkel's statement[26] that the effects of higher-order virial coefficients decrease with increasing L/D and vanish in the limit of $L/D \to \infty$ (while his statement was made for hard spherocylinders, it also holds for Model A).

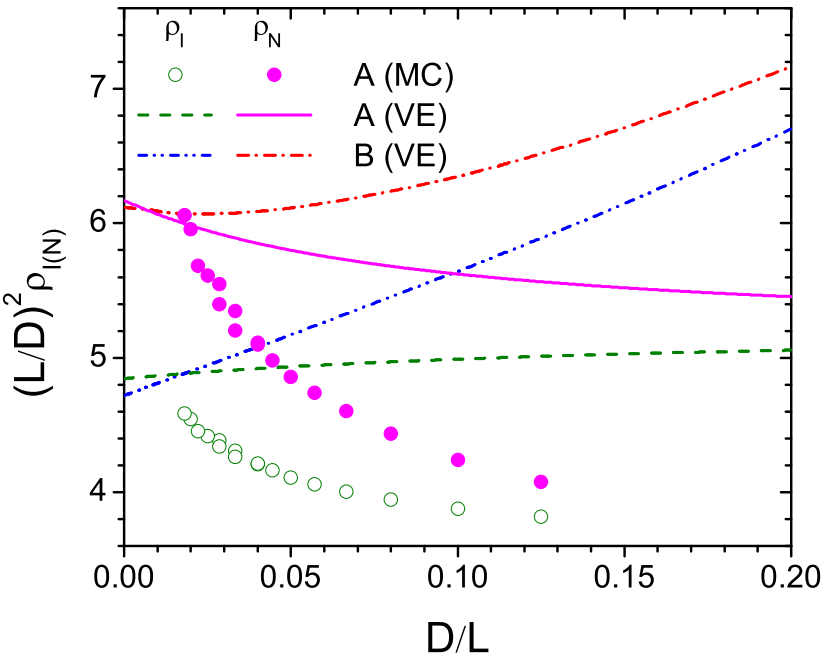

Figure 5.8: Phase diagrams for Model A and B with $\epsilon = 2$.

In Fig. 5.8 we also compare the phase diagrams predicted by VE for Model A and B with $\epsilon = 2$. We see that $(L/D)^2\rho_{\rm I}$ increases with increasing D/L for both models. On the other hand, while $(L/D)^2\rho_{\rm N}$ decreases with increasing D/L for Model A, it exhibits a minimum around $D/L = 0.25$ for Model B. Finally, we note that, in the limit of $L/D \to \infty$, while Model A and B coincide and recover the results of Onsager's model of hard needles[27] in the limit of $\epsilon \to \infty$, at finite ϵ these two models are different from each other.

5.4 Conclusions

To summarize, we have proposed a novel anisotropic soft-core potential for spherocylinders (Model B given by Eq. (5.2)), which is superior to other soft-core spherocylinder models depending only on the minimum distance between two line segments representing spherocylinders (e.g., Model A given by Eq. (5.1)) in that it takes into account the degree of overlap between two spherocylinders. This is demonstrated using a few examples where the actual overlapping volume between two spherocylinders is known.

Using fast off-lattice Monte Carlo simulations[1] in an isothermal-isobaric ensemble with the replica exchange (RE) at different pressures[21] and the multiple histogram reweighting (HR) technique,[22,23] we have studied the isotropic-nematic transition (INT) of both Model A and B, which recovers the standard model of hard spherocylinders[9] for liquid crystals as the repulsion strength $\epsilon \to \infty$. RE improves our sampling efficiency near INT by at least an order of magnitude, and HR allows us to accurately locate the transition pressure P^* based on the equal-weight criterion,[25] which is consistent with the peak position of the isothermal compressibility and constant-pressure heat capacity of the system.

We have constructed phase diagrams for both Model A and B with the spherocylinder aspect ratio $L/D = 7$, and compared simulation results with predictions of virial expansion (VE) analogous to Onsager's work.[9] We find that the following VE predictions are in qualitative agreement with our simulation results: For Model A both $[1-\exp(-\epsilon)]\rho_{\mathrm{I(N)}}$ (where $\rho_{\mathrm{I(N)}}$ denotes the number density of spherocylinders in the co-existing isotropic (nematic) phase) and the orientational order parameter S_{N} of the co-existing nematic phase are independent of ϵ, and for Model B $\rho_{\mathrm{I(N)}} \propto \epsilon^{-2}$ at small ϵ and S_{N} slightly varies with $\epsilon \geq 2$. This means INT still occurs at high enough densities even for small ϵ. At large ϵ, ρ_{I}, ρ_{N} and P^* for Model A are almost independent of ϵ, while those for Model B still decrease with increasing ϵ. This means Model B is "softer" (thus has higher P^*) than Model A. Consistent with the simulation results of Vink and Schilling for Model A with $\epsilon = 2$,[5] VE predicts that $\rho_{\mathrm{N}} - \rho_{\mathrm{I}}$ increases with decreasing L/D in the same trend as ρ_{I} and ρ_{N}.

Because only the first-order terms are included in VE with all higher-order terms neglected, we find that VE overestimates ρ_{I}, ρ_{N}, $\rho_{\mathrm{N}} - \rho_{\mathrm{I}}$, and S_{N} for both Model A and B, and that it overestimates P^* for Model A. VE predictions become more accurate with increasing L/D and should be exact in the limit of $L/D \to \infty$, where both ρ_{I} and ρ_{N} vanish (at $\epsilon > 0$) but $(L/D)^2\rho_{\mathrm{I(N)}}$ remains finite. Finally, an approximate correspondence between VE of Model A and the commonly used Maier-Saupe interaction[24] is given in Appendix A.

REFERENCES

[1] Q. Wang and Y. Yin, J. Chem. Phys. **130**, 104903 (2009) and references therein; F. A. Detcheverry, D. Q. Pike, P. F. Nealey, M. Muller, and J. J. de Pablo, Phys. Rev. Lett. **102**, 197801 (2009).

[2] Q. Wang, Soft Matter **5**, 4564 (2009); **6**, 6206 (2010); P. Zhang, X. Zhang, B. Li, and Q. Wang, Soft Matter **7**, 4461 (2011); P. Zhang, B. Li, and Q. Wang, Macromolecules **44**, 7837 (2011); **45**, 2537 (2012).

[3] Q. Wang, Soft Matter **7**, 3711 (2011).

[4] C. Vega and S. Lago, Comput. Chem. **18**, 55 (1994).

[5] R. L. C. Vink and T. Schilling, Phys. Rev. E **71**, 051716 (2005).

[6] R. L. C. Vink and T. Schilling, J. Chem. Phys. **123**, 074901 (2005).

[7] K. M. Aoki and T. Akiyama, Mol. Cryst. Liq. Cryst. **262**, 543 (1995).

[8] Z. E. Hughes, L. M. Stimson, H. Slim, J. S. Lintuvuori, J. M. Ilnytskyi, and M. R. Wilson, Comput. Phys. Commun. **178**, 724 (2008).

[9] L. Onsager, Ann. N.Y. Acad. Sci. **51**, 627 (1949).

[10] J. S. Lintuvuori and M. R. Wilson, J. Chem. Phys. **128**, 044906 (2008).

[11] J. S. Lintuvuori and M. R. Wilson, J. Chem. Phys. **132**, 224902 (2010).

[12] S. Prestipino and F. Saija, J. Chem. Phys. **126**, 194902 (2007).

[13] A. Nikoubashaman and C. N. Likos, J. Phys: Condens. Matter **22**, 104107 (2010).

[14] R. Berardi, C. Zannoni, J. S. Lintuvuori, and M. R. Wilson, J. Chem. Phys. **131**, 174107 (2009).

[15] R. Berardi, J. S. Lintuvuori, M. R. Wilson, and C. Zannoni, J. Chem. Phys. **135**, 134119 (2011).

[16] P. J. Hoogerbrugge and J. M. V. A. Koelman, Europhys. Lett. **19**, 155 (1992); R. D. Groot and P. B. Warren, J. Chem. Phys. **107**, 4423 (1997).

[17] A. AlSunaidi, W. K. den Otter, and J. H. R. Clarke, Phil. Trans. R. Soc. Lond. A **362**, 1773 (2004).

[18] Y. K. Levine, A. E. Gomes, A. F. Martins, and A. Polimeno, J. Chem. Phys. **122**, 144902 (2005).

[19] J. A. Purton and W. Smith, Mol. Simul. **36**, 796 (2010).

[20] P. Bolhuis and D. Frenkel, J. Chem. Phys. **106**, 666 (1997).

[21] N. C. Ekdawi-Sever, P. B. Conrad, and J. J. de Pablo, J. Phys. Chem. A **105**, 734 (2001); T. Okabe, M. Kawata, Y. Okamoto, and M. Mikami, Chem. Phys. Lett. **335**, 435 (2001); T. Kristof and J. Liszi, Mol. Phys. **99**, 167 (2001).

[22] A. M. Ferrenberg and R. H. Swendsen, Phys. Rev. Lett. **63**, 1195 (1989).

[23] J. D. Chodera, W. C. Swope, J. W. Pitera, C. Seok, and K. A. Dill, J. Chem. Theory Comput. **3**, 26 (2007).

[24] R. Holyst and P. Oswald, Macromol. Theory Simul. **10**, 1 (2001).

[25] M. Muller and N. B. Wilding, Phys. Rev. E **51**, 2079 (1995).

[26] D. Frenkel, J. Phys. Chem. **91**, 4912 (1987).

[27] H. N. W. Lekkerkerker, P. Coulon, and R. Van Der Haegen, J. Phys. Chem. **80**, 3427 (1984).

CHAPTER 6

CONCLUDING REMARKS AND FUTURE WORK

In this chapter, I will briefly summarize all the studies in this dissertation, and then point out some extensions that can be possibly made based on the current work.

6.1 Concluding Remarks

We have performed fast off-lattice Monte Carlo (FOMC) simulations and mean-field calculation to study the order-disorder transition (ODT) of symmetric diblock copolymers (DBC). Exactly the same model system (Hamiltonian) is used in both simulations and mean-field theory to unambiguously quantify the shift of ODT $\chi^* N$ from the mean-field prediction $\chi^*_{\rm MF} N$; the ODT shift is therefore due to the fluctuations/correlations neglected by the latter. We have varied all the parameters in our model system (the invariant degree of polymerization $\bar{\mathcal{N}}$, the number of segments N on each chain, the finite interaction range σ, and the compressibility N/κ of DBC melts) to examine their effects on the ODT shift. While $\chi^*/\chi^*_{\rm MF} - 1 \propto \bar{\mathcal{N}}^{-k}$ is found in all the cases, k decreases around $\bar{\mathcal{N}}_{\rm cp}$ (the $\bar{\mathcal{N}}$-value corresponding to the FCC close packing of polymer segments as hard spheres), indicating the short-range correlation effects.

To highlight the importance of quantitative and parameter-fitting-free comparisons among different models/methods, we perform both self-consistent field (SCF) calculations and FOMC simulations for the DPD model (i.e., DBC model used in dissipative particle dynamics (DPD) simulations[1]). Comparing SCF results for DPD model with those for the "standard" model[2] therefore unambiguously reveals the effects of model differences, and for the DPD model, comparing our SCF results with FOMC results reveals the effects of system fluctuations/correlations neglected in the SCF theory. Furthermore, comparing our FOMC

results with the DPD results[1] obtained in the fixed-size box unambiguously identifies the kinetically trapped structures in the latter, and comparing our SCF (or FOMC) results in fixed- and variable-size boxes can unambiguously reveal the effects of fixed vs. bulk periods.

We investigate the effect of system compressibility N/κ on the ODT of DBC melts. We use both the SCF calculations and FOMC simulations to determine the ODT of compressible DBC melts by equating the Gibbs free energy per chain of the two co-existing phases, and compare with our previous results obtained by equating the Helmholtz free energy per chain in Chapters 2 and 3. We find that the co-existing range is quite small and decreases as the system becomes less compressible, which justifies the previous results in Chapters 2 and 3 where it was assumed that the co-existing phases have the same density. We also find that, when $N/\kappa = 0$, the SCF theory predicts the ODT to be a second-order phase transition even for asymmetric DBC melts.

In addition, we use FOMC to determine the isotropic-nematic transition (INT) of liquid crystals (modeled as spherocylinders). We propose a novel anisotropic soft-core potential for spherocylinders (Model B) that takes into account the degree of overlap between two spherocylinders, thus superior to other soft-core spherocylinder models depending only on the minimum distance between two line segments representing spherocylinders, for example, that used by Vink and Schilling[3] (referred to as Model A). Using FOMC simulations in an isothermal-isobaric ensemble, we study the INT of both Model A and B, which recover the standard model of hard spherocylinders for liquid crystals as the repulsion strength $\epsilon \to \infty$, and compare simulation results with predictions of virial expansion (VE). We find that VE results shows INT still occurs at high enough densities even for small ϵ. While VE predictions are in qualitative agreement with FOMC simulation results, we see that VE overestimates the co-existing number densities of isotropic and nematic phases for both Model A and B, because only the first-order terms are included in VE with all higher-order terms neglected. VE predictions become more accurate with increasing aspect ratio of spherocylinders and should be exact in the limit of infinitely large aspect ratio.

6.2 Future Work

Rod-coil (RC) block copolymer (BCP) melts have received great research interest in the areas of material science, nanochemistry, and biomimetic chemistry due to their useful intrinsic functionalized rod structures and the ability to self-assemble to variety of nanostructures.[4,5] Particularly, conjugated polymers, which contain both electron donating rod block and electron accepting coil block, are by far the most promising functional polymers in view of their applications in flexible and less expensive electronic devices.[5] While controlling their morphology and size is critically important for optimizing the device efficiency, a recent review[6] shows that the self-assembly of RC BCPs is far less understood compared with coil-coil (CC) block polymers, and only a few theoretical studies and simulations have been reported due to the complexity of introducing a rigid rod into BCP.

While Maier-Saupe mean-field interaction is usually used for the anisotropic potential between rods in the conventional theoretical calculations[7–9] of RC BCPs, no corresponding physical model can be used in molecular simulations. Based on the novel soft-core potentials (Model B) proposed in Chapter 5, we can build a model of RC BCP which can be readily studied by both FOMC simulations and theoretical calculations, and thus we can unambiguously quantify approximations introduced in theoretical assumptions. This is a natural and promising extension of FOMC method currently applied for diblock copolymers and liquid crystals in this work.

REFERENCES

[1] R. D. Groot and T. J. Madden, J. Chem. Phys. **108**, 8713 (1998).

[2] M. W. Matsen and F. S. Bates, Macromolecules **29**, 1091 (1996).

[3] R. L. C. Vink and T. Schilling, Phys. Rev. E **71**, 051716 (2005).

[4] M. Lee, B. Cho, and W. Zin , Chem. Rev. **101**, 3869 (2001).

[5] B. Olsen and R. Segalman, Mater. Sci. Eng. R **62**, 37 (2008).

[6] Q. Wang, Soft Matter **7**, 3711 (2011).

[7] V. Pryamitsyn and V. Ganesan, J. Chem. Phys. **120**, 5824 (2004).

[8] Y. Kriksin and P. Khalatur, Macromol. Theory Simul. **21**, 382 (2012).

[9] S. Li, Y. Jiang, and J. Chen, Soft Matter **10**, 8932 (2014).

APPENDIX A

RELATION BETWEEN MODEL A AND MAIER-SAUPE INTERACTION

Here we derive an approximate correspondence between the virial expansion of Model A used in Chapter 5 and the commonly used Maier-Saupe interaction.[1] At large L/D, ignoring the first two terms in the integrand of Eq. (5.5), we can approximate the system excess free energy (i.e., the first line of Eq. (5.4)) as

$$\begin{aligned}\beta\mathcal{F}^{ex} &\approx [1-\exp(-\epsilon)]\,\frac{L^2Dn^2}{V}\int \mathrm{d}\mathbf{u}\mathrm{d}\mathbf{u}'\phi(\mathbf{u})|\mathbf{u}\times\mathbf{u}'|\phi(\mathbf{u}')\\ &= [1-\exp(-\epsilon)]\,L^2D\int \mathrm{d}\mathbf{r}\mathrm{d}\mathbf{u}\mathrm{d}\mathbf{u}'\hat{\rho}(\mathbf{r},\mathbf{u})|\mathbf{u}\times\mathbf{u}'|\hat{\rho}(\mathbf{r},\mathbf{u}')\\ &= [1-\exp(-\epsilon)]\,L^2D\int \mathrm{d}\mathbf{r}\sum_{i=1}^{n}\delta(\mathbf{r}-\mathbf{r}_i)\sum_{j=1}^{n}\delta(\mathbf{r}-\mathbf{r}_j)|\mathbf{u}_i\times\mathbf{u}_j|, \qquad \text{(A.1)}\end{aligned}$$

where $\hat{\rho}(\mathbf{r},\mathbf{u}) \equiv \sum_{i=1}^{n}\delta(\mathbf{r}-\mathbf{r}_i)\delta(\mathbf{u}-\mathbf{u}_i)$ is the microscopic density of spherocylinders at spatial position $\mathbf{r}$ with orientation $\mathbf{u}$.

Next, expanding $|\mathbf{u}_i\times\mathbf{u}_j|$ in terms of spherical harmonics gives[2]

$$|\mathbf{u}_i\times\mathbf{u}_j| = \sum_{l=0}^{\infty}\sum_{m=-l}^{l}\frac{4\pi}{2l+1}d_l Y_{lm}(\mathbf{u}_i)Y_{lm}^*(\mathbf{u}_j),$$

where $d_l = 0$ for odd l, $d_0 = \pi/4$,

$$d_{2k} = -\frac{\pi(4k+1)(2k)!(2k-2)!}{2^{4k+1}(k-1)!k!k!(k+1)!},$$

$Y_{00}(\mathbf{u}) = 1/2\sqrt{\pi}$, and the spherical harmonics addition theorem gives

$$\sum_{m=-l}^{l}Y_{lm}(\mathbf{u}_i)Y_{lm}^*(\mathbf{u}_j) = \frac{2l+1}{4\pi}P_l(\cos\gamma)$$

with P_l being the l^{th} order Legendre polynomial.

Truncating at $l = 2$, we have

$$|\mathbf{u}_i \times \mathbf{u}_j| \approx \pi^2 Y_{00}(\mathbf{u}_i) Y_{00}^*(\mathbf{u}_j) - \frac{\pi^2}{8} \sum_{m=-2}^{2} Y_{2m}(\mathbf{u}_i) Y_{2m}^*(\mathbf{u}_j) = \frac{\pi}{4} - \frac{5\pi}{32} P_2(\cos\gamma) \tag{A.2}$$

with $P_2(x) \equiv (x^2 - 1/3)/2$. Using the relation

$$\left(\mathbf{u}_i\mathbf{u}_i - \frac{\mathbf{I}}{3}\right) : \left(\mathbf{u}_j\mathbf{u}_j - \frac{\mathbf{I}}{3}\right) = \cos^2\gamma - \frac{1}{3},$$

we re-write Eq. (A.2) as

$$|\mathbf{u}_i \times \mathbf{u}_j| \approx \frac{\pi}{4} - \frac{15\pi}{64} \left(\mathbf{u}_i\mathbf{u}_i - \frac{\mathbf{I}}{3}\right) : \left(\mathbf{u}_j\mathbf{u}_j - \frac{\mathbf{I}}{3}\right).$$

Substituting the above into Eq. (A.1) and defining

$$\hat{\rho}_{cm}(\mathbf{r}) \equiv \sum_{i=1}^{n} \delta(\mathbf{r} - \mathbf{r}_i)$$

and

$$\hat{\mathbf{S}}(\mathbf{r}) \equiv \sum_{i=1}^{n} \delta(\mathbf{r} - \mathbf{r}_i) \left(\mathbf{u}_i\mathbf{u}_i - \frac{\mathbf{I}}{3}\right),$$

we finally obtain $\beta\mathcal{F}^{ex}$ in form of the Maier-Saupe interaction

$$\beta\mathcal{F}^{ex} \approx \frac{\pi}{4} \left[1 - \exp(-\epsilon)\right] L^2 D \int \mathrm{d}\mathbf{r} \hat{\rho}_{cm}^2(\mathbf{r}) - \frac{15\pi}{64} \left[1 - \exp(-\epsilon)\right] L^2 D \int \mathrm{d}\mathbf{r} \hat{\mathbf{S}}(\mathbf{r}) : \hat{\mathbf{S}}(\mathbf{r}),$$

where the first term is due to the isotropic interaction and the second term corresponds to the quadratic approximation of the anisotropic interaction of Model A.

REFERENCES

[1] R. Holyst and P. Oswald, Macromol. Theory Simul. **10**, 1 (2001).

[2] S. M. Cui, O. Akcakir and Z. Y. Chen, Phys. Rev. E **51**, 4548 (1995).